

2015-01-01

Characterization of the Nodamura virus RNA dependent RNA polymerase and Formation of RNA Replication Complexes in Mammalian Cells

Vincent Ulysses Gant

University of Texas at El Paso, vug84dc@gmail.com

Follow this and additional works at: https://digitalcommons.utep.edu/open_etd

 Part of the [Biochemistry Commons](#), [Molecular Biology Commons](#), and the [Virology Commons](#)

Recommended Citation

Gant, Vincent Ulysses, "Characterization of the Nodamura virus RNA dependent RNA polymerase and Formation of RNA Replication Complexes in Mammalian Cells" (2015). *Open Access Theses & Dissertations*. 1047.
https://digitalcommons.utep.edu/open_etd/1047

This is brought to you for free and open access by DigitalCommons@UTEP. It has been accepted for inclusion in Open Access Theses & Dissertations by an authorized administrator of DigitalCommons@UTEP. For more information, please contact lweber@utep.edu.

CHARACTERIZATION OF THE NODAMURA VIRUS RNA DEPENDENT RNA
POLYMERASE AND FORMATION OF RNA REPLICATION
COMPLEXES IN MAMMALIAN CELLS

VINCENT ULYSSES GANT JR.

Department of Biological Sciences

APPROVED:

Kyle L. Johnson, Ph.D., Chair

Ricardo A. Bernal, Ph.D.

Kristine M. Garza, Ph.D.

Kristin Gosselink, Ph.D.

German Rosas-Acosta, Ph. D.

Jianjun Sun, Ph.D.

Charles Ambler, Ph.D.

Dean of the Graduate School

Copyright ©

By

Vincent Ulysses Gant Jr.

2015

Dedication

I want to dedicate my dissertation to my beautiful mother, Maria Del Carmen Gant. My mother lived her life to make sure all of her children were taken care of and stayed on track. She always pushed me to stay on top of my education and taught me to grapple with life. My mother was incredibly strong and her strength has helped me weather many storms so that I may enjoy the warm sun. I also dedicate this work to my grandfather, James Powell Broome. Much of what I loved about my mother came from him and together they shaped me. He was my first mentor in life and his wisdom could fill the world's oceans many times over. He taught me everything from tying a perfect Windsor knot to treating people with respect and kindness. The essence of my mother and her father is engrained into these pages and their memories will live on in them.

CHARACTERIZATION OF THE NODAMURA VIRUS RNA-DEPENDENT RNA
POLYMERASE AND FORMATION OF RNA REPLICATION
COMPLEXES IN MAMMALIAN CELLS

By

VINCENT ULYSSES GANT, JR., B.S.

DISSERTATION

Presented to the Faculty of the Graduate School of

The University of Texas at El Paso

in Partial Fulfillment

of the Requirements

for the Degree of

DOCTOR OF PHILOSOPHY

Department of Biological Sciences

THE UNIVERSITY OF TEXAS AT EL PASO

May 2015

Acknowledgements

I want to thank Dr. Kyle L. Johnson for giving me all the tools and opportunity I needed to succeed. She is a very generous and understanding mentor and her guidance was invaluable. Her mentorship has pushed me to strive for the best and to keep charging forward until I've succeeded – and then keep going. I give many thanks to my dissertation committee for providing amazing ideas, critical feedback and a true challenge. All of our meetings were very much looked forward to and were such pleasures. I would like to thank everyone who has come through the KLJ lab at UTEP. Your company and friendship has certainly made all of this an extraordinary chapter in my life. I want to give the biggest thanks to my best friend and future wife, Stephanie Moreno. Her unending support and love have carried me through a lot of the seemingly unending hours.

Abstract

Positive-strand RNA viruses amplify their genomes in membrane-bound structures associated with intracellular membranes and organelles called replication complexes (**RCs**). Here, we begin to elucidate mechanisms of *Nodamura virus* (**NoV**; family *Nodaviridae*) RC assembly. The literature reports that NoV-infected muscle tissue exhibits mitochondrial aggregation and rearrangement of mitochondrial structure, leading to disorganization of the muscle fibrils. However, the molecular basis for this pathogenesis and the role of mitochondria in NoV infection remained unclear until now. We tested the hypothesis that NoV establishes RCs in association with mitochondria in cultured mammalian cells at physiological temperature. We used immunofluorescence confocal microscopy and biochemical methods to determine that the aggregated mitochondria represent the sites of NoV RCs. We determined that the NoV RdRp (protein A; **NA**) uses two membrane-associated regions to localize to mitochondria as an integral membrane protein. Cells expressing NA exhibit mitochondrial morphologies similar to that described for diabetes, neurodegenerative disease and cardiovascular disease. Mitochondrial morphology is controlled by a cyclical mechanism referred to as mitochondrial dynamics, which involves fission and fusion pathways by which mitochondria cycle between two distinct forms: organelle and tubular. The tubular form resembles the clustered phenotype we observe in the presence of NA. This led us to hypothesize that NA disrupts mitochondrial fission, leading to accumulation of clustered mitochondria. In this dissertation we present evidence that NA interacts with the cellular machinery controlling mitochondrial morphology, which we interpret as the viral polymerase subverting mitochondrial dynamics to establish its RCs.

Table of Contents

Acknowledgements.....	v
Abstract.....	vi
Table of Contents	vii
List of Tables	ix
List of Figures.....	x
Chapter 1: Background and Significance	1
1.1 Family <i>Nodaviridae</i>	2
1.2 Ecology and Natural Host Range	3
1.3 Nodavirus Virion Structure and Genome Packaging	10
1.4 Nodavirus Genome Organization.....	16
1.5 Nodavirus RNA Replication	19
1.6 RNA Replication Systems.....	26
1.7 Replication Complex (RC) Formation	36
Chapter 2: Subcellular Localization of the NoV RdRp in Mammalian Cells	44
2.1 Introduction.....	44
2.2 Materials and Methods	45
2.3 Results.....	54
2.4 Conclusions	85
Chapter 3: NoV RC Formation Induces Imbalance in Mitochondrial Dynamics	89
3.1 Introduction.....	89
3.2 Materials and Methods	98
3.3 Results.....	103

3.4 Future Experiments	136
3.4.1 Immunofluorescence confocal microscopic analysis of Drp1	
translocation inhibition in multi-labeled cells	136
3.4.2 Kinetics of Drp1 translocation inhibition by the NoV RdRp	137
3.4.3 Effect of NoV RdRp on Drp1 SUMOylation in transfected cells	139
3.5 Conclusions	142
Chapter 4: Discussion.....	147
4.1 NoV RC localization and NA membrane association.....	147
4.2 The NoV RdRp may perturb mitochondrial apoptosis during infection	148
4.3 The NoV RdRp interferes with mitochondrial dynamics possibly by	
disrupting Drp1 and mitochondrial fission	153
4.4 The NoV RdRp may antagonize Drp1 activity by binding SUMO1 and	
preventing mitochondrial fission	157
4.5 Concluding remarks.....	162
References	164
Glossary	193
Appendix I:	199
A1.1 Phylogenetic analysis of genomic RNA segments	199
A1.2 Mitochondrial association of protein A	204
A1.3 Concluding Remarks	205
Curriculum Vita.....	209

List of Tables

Table 1: The family <i>Nodaviridae</i> and natural hosts	4
Table 2: Organisms and cells permissive to NoV infection or RNA Replication ..	11
Table 3: Oligonucleotide primers used for circular PCR-based mutagenesis	50
Table 4: Overlap coefficients calculated for confocal microscopy experiments shown in Figures 16, 17, 19 and 22.....	51
Table 5: Overlap coefficients calculated for confocal microscopy experiments shown in Figures 32, 33, and 34.....	135

List of Figures

Figure 1: <i>Nodamura virus</i> infection in mammals results in fatal hind-limb paralysis	7
Figure 2: NoV infection induces ultrastructural changes to sarcosomes of infected <i>G. mellonella</i> larva muscle cells	9
Figure 3: <i>Nodamura virus</i> particle and coat protein structure	13
Figure 4: Schematic of the nodavirus genome organization	18
Figure 5: Schematic of nodavirus RNA replication	20
Figure 6: FHV cDNA expression using a recombinant Vaccinia viral vector	27
Figure 7: The 5' untranslated regions of the five alphavirus genomic RNA1 segments.....	29
Figure 8: Schematic of the T7 expression vector TVT7R(0,0).....	31
Figure 9: Schematic of the BSR-T7/5 cell culture system	33
Figure 10: Induction of DNA-launched NoV RNA replication in plasmid-transformed yeast cells.....	35
Figure 11: Viral RNA-dependent RNA polymerase (RdRp) activities	37
Figure 12: RNA RC formation by positive-strand RNA viruses	39
Figure 13: FHV infection induces ultrastructural changes to mitochondria of infected <i>Drosophila</i> DL-1 cells	42
Figure 14: NoV RNA replication is unaffected by the presence of a C-terminal HA epitope tag	56
Figure 15: NoV RdRp expression time course analysis	59
Figure 16: NoV RdRp localization time course analysis	61

Figure 17: The NoV RdRp localizes to the surface of mitochondria	63
Figure 18: The NoV RdRp is predicted to contain two membrane-associated regions	66
Figure 19: Subcellular localization of the NoV RdRp is dependent on both MARs	70
Figure 20: Analysis of NoV RdRp intracellular membrane association	73
Figure 21: Deletion of the MARs reduces RdRp expression levels but did not appear to increase proteasome-mediated degradation	78
Figure 22: NoV RdRp-catalyzed RNA synthesis localizes to mitochondria in transfected BSR-T7/5 cells	80
Figure 23: Deletion of the MARs on the NoV RdRp results in a severe defect in RNA replication	83
Figure 24: Mitochondrial morphology dynamics	90
Figure 25: General schematic of reversible SUMO modification.....	95
Figure 26: Predicted SUMO site conserved among alphanodaviruses	104
Figure 27: NoV protein A is SUMOylated <i>in vitro</i>	106
Figure 28: SUMOylated NA species were not detected after immunoprecipitation from cultured mammalian cells	109
Figure 29: The NoV RdRp co-immunoprecipitates with SUMO1.....	112
Figure 30: Mutating the three predicted SUMO consensus motifs abolishes the interaction between NA and SUMO1 in mammalian cells.....	116
Figure 31: The predicted domains and motifs on the NoV RdRp	121
Figure 32: The NoV RdRp and SUMO1 co-localize in the cytoplasm of transfected	

BSR-T7/5 cells	125
Figure 33: The subcellular localization of Drp1 in BSR-T7/5 cells	128
Figure 34: The NoV RdRp alters the subcellular localization of Drp1 in transfected BSR-T/5 cells	131
Figure 35: Potential topologies adopted by the NoV RdRp in its interaction with the OMM	149
Figure 36: A hypothetical model of inhibition of mitochondrial fission by the NoV RdRp membrane protein.....	160
Figure 37: Phylogeny among the alpha- and betanodavirus RNA1 segments.....	200
Figure 38: Phylogeny among the alpha- and betanodavirus RNA2 segments.....	202
Figure 39: Sequence identity of alphanodavirus genomic RNAs	206
Figure 40: Sequence identity of betanodavirus genomic RNAs	207
Figure 41: Topology predictions for protein A from FHV, GGNNV, NoV, PaV.....	208

Chapter 1: Background and Significance

Viruses with RNA genomes currently comprise the largest genetic class of viruses. Many of these are human pathogens for which there is a lack of curative treatments or federally approved vaccines (20). One of the most unique and genetically simple families in the expansive class of RNA viruses is the *Nodaviridae*. In 1956, the *Nodaviridae* came into the scope of biological sciences when *Nodamura virus* (**NoV**) was discovered. NoV was found in *Culex tritaeniorhynchus* mosquitoes captured in a pig-baited magoon trap during a screen for *Japanese Encephalitis virus* in Nodamura, Japan. The *Nodaviridae* is a diverse family with a worldwide presence with terrestrial and water dwelling hosts. Ever since their discovery the nodaviruses have served as excellent model systems for the study of RNA replication, virus assembly and structure, and replication complex (**RC**) formation (58, 123, 124, 127, 229).

This doctoral dissertation presents the results of novel studies in NoV research that localizes the viral RNA-dependent RNA polymerase (**RdRp**) and RCs to specific sites in mammalian cells (**Chapter 2**) and defines the mechanism by which RCs are formed, which we hypothesize to involve subversion of an essential cellular process (**Chapter 3**). The implications of these findings for nodavirus research and for viral RNA replication mechanisms are described in this dissertation's Discussion (**Chapter 4**). Further studies that redefine the phylogenetic relationships between NoV and other members of the family *Nodaviridae*, while peripheral to the other projects described herein, are considered in **Appendix I**.

1.1 Family *Nodaviridae*

NoV is the type species of the alphanodavirus genus of the virus family *Nodaviridae*. The family *Nodaviridae* consists of two genera: the alphanodavirus genus, including NoV, *Flock House virus* (**FHV**), and *black beetle virus* (**BBV**), which primarily infect insects; and the betanodaviruses, including *greasy grouper nervous necrosis virus* (**GGNNV**) and *Atlantic halibut nodavirus* (**AHNV**), which have been isolated only from fish (18, 19). The alphanodaviruses cause stunting, hind-segment paralysis and death in invertebrate hosts, while NoV causes similar infections in both invertebrate and mammalian hosts (15, 104, 293). All betanodaviruses have been isolated from fish and cause fatal viral nervous necrosis (**VNN**) or viral encephalopathy and retinopathy (**VER**). Fish afflicted with VNN or VER display abnormal swimming, belly-up floating, and lesions or necrosis of the central nervous system (**CNS**) and retina (32, 238).

A number of unclassified nodaviruses have been isolated from organisms including farmed and wild fish, ornamental fish, and shrimp (9, 29, 31, 49, 56, 153, 192, 255, 263, 270). In China, *Wuhan nodavirus* (**WhNV**) was isolated from larvae of the Small White butterfly (*Pieris rapae*). *Macrobrachium rosenbergii* nodavirus (**MrNv**) was isolated from the freshwater giant river prawn *Macrobrachium rosenbergii*, whose natural habitat ranges from Southeast Asia to northern Australia (8). *Penaeus vannamei* nodavirus (**PvNV**) was isolated from *Penaeus vannamei*, a shrimp found along the eastern Pacific from Mexico and to South America (255). These prawn and shrimp nodaviruses cause similar disease in these animals as the betanodaviruses cause in fish (8, 255). Additionally these two crustacean nodaviruses are the most related or similar to NoV based on their RNA1 sequence with these two forming a clade that is a

sister group to NoV (**Appendix I**). Next, we consider the ecological aspects of NoV and other nodaviruses and their natural host range.

1.2 Ecology and Natural Host Range

The *Nodaviridae* have a worldwide presence and are capable of being carried by or replicating in a variety of animals. For a current complete list of nodaviruses, refer to **Table 1**. Nodaviruses primarily affect arthropod and fish populations, and the ecological effects of these viruses are not fully known. *Pariacoto virus (PaV)* has economic importance as a potential biological pest control since it was isolated in Peru from infected Southern armyworms (*Spodoptera eridania*), which are pests of various crops including sweet potatoes and tomatoes (293). Conversely, the betanodaviruses pose a great challenge to the safety of the world's aquaculture industry, primarily those rearing fish for human consumption (30, 36, 171, 173, 245, 246, 290). The nodaviruses infecting freshwater and oceanic crustaceans apply additional pressure to seafood sources with an increased risk of human exposure to nodavirus-infected animals. In addition, the risk of possible emergence of NoV-like viruses in the human population from either fresh standing water or carrier animals remains to be determined. This can be unsettling considering the discovery of novel nodavirus-like sequences isolated from the stool of children afflicted with acute flaccid paralysis in South Asia (275).

Metagenomic analysis have played an important role in virus discovery and elucidated the many possible places on this planet in which a virus may be waiting for a host (35, 73). Nodaviral sequences closely related to both alpha- and betanodaviruses were discovered in bat guano collected in Texas and California, USA, further expanding

Table 1: The family *Nodaviridae* and natural hosts.

Virus	Natural Host Range
Insect Isolates	
American nodavirus (ANV)	Unknown, isolated from <i>Drosophila</i> Schneider 2 (S2) cell line (283)
Black beetle virus (BBV)	<i>Heteronychus arator</i> (African black beetle) (154)
Boolarra virus (BoV)	<i>Oncopera intricoides</i> (<i>Hepialidae</i> moth) (209)
Flock House virus (FHV)	<i>Costelytra zealandica</i> (Grass grub) (232)
<i>Lymantria ninayi</i> virus (LNV)	<i>Lymantria ninayi</i> (<i>Lymantriidae</i> moth) (100)
Manawatu virus (MwV)	<i>Costelytra zealandica</i> (Grass grub) (233)
New Zealand virus/ <i>Drosophila</i> line 1 virus (NZV/DLV)	Unknown, isolated from a New Zealand subline of <i>Drosophila</i> line 1 (DL1) cells (77, 233)
Nodamura virus (NoV)	<i>Culex tritaeniorhynchus</i> (<i>Culex</i> Mosquito) and/or <i>Sus scrofa domesticus</i> (domesticated pigs) (220)
Pariacoto virus (PaV)	<i>Spodoptera eridania</i> (Southern armyworm) (293)
Wuhan nodavirus (WhNV)	<i>Pieris rapae</i> (Small white butterfly, larvae) (153)
Fish Isolates	
Atlantic cod betanodavirus (ACNV)	<i>Gadus morhua</i> (Atlantic cod) (246)
Atlantic halibut nodavirus (AHNV)	<i>Hippoglossus hippoglossus</i> (Atlantic halibut) (102)
Asian sea bass nervous necrosis virus (SBNNV)	<i>Lates calcarifer</i> (Asian sea bass or barramundi) (207)
Barfin flounder nervous necrosis virus (BFNNV)	<i>Verasper moseri</i> (Barfin flounder) (182)
<i>Dicentrarchus labrax</i> encephalitis virus (DIEV)	<i>Dicentrarchus labrax</i> (Sea bass) (53)
Dragon grouper nervous necrosis virus (DGNNV)	<i>Epinephelus lanceolatus</i> (Dragon grouper) (76)
Golden pompano nervous necrosis virus (GPNNV)	<i>Trachinotus blochii</i> (Golden pompano) (208)
Guppy nervous necrosis virus (GNNV)	<i>Poecilia reticulata</i> (Guppy) (112)

Table 1 Continued: The family *Nodaviridae* and natural hosts.

Virus	Natural Host Range
Greasy grouper nervous necrosis virus (GGNNV)	<i>Epinephelus tauvina</i> (Greasy grouper) (50, 253)
Iberian betanodavirus (IBNNV)	<i>Solea senegalensis</i> (Senegalese sole) (56)
Japanese flounder nervous necrosis virus (JFNNV)	<i>Paralichthys olivaceus</i> (Japanese flounder) (182)
Malabaricus grouper nervous necrosis virus (MGNNV)	<i>Epinephelus malabaricus</i> (Brown spotted grouper) (172)
Mouse grouper nervous necrosis virus (MgNNV)	Family <i>Serranidae</i> (sea bass and groupers)
Redspotted grouper nervous necrosis virus (RGNNV)	<i>Epinephelus akaara</i> (Red spotted grouper) (171, 182)
Seven-band grouper nervous necrosis virus (SGNNV)	<i>Epinephelus septemfasciatus</i> (Seven-band grouper) (139)
Striped jack nervous necrosis virus (SJNNV)	<i>Pseudocaranx dentex</i> (Striped jack) (172)
Tiger grouper nervous necrosis virus (TGNNV)	<i>Mycteroperca tigris</i> (Tiger grouper) (183)
Tiger puffer nervous necrosis virus (TPNNV)	<i>Takifugu rubrides</i> (Tiger puffer) (182)
Turbot nodavirus (TNV)	<i>Psetta maxima</i> (Turbot) (30)
White star snapper nervous necrosis virus (WSNNV)	<i>Lutjanus stellatus</i> (White star snapper) (183)
Crustacean Isolates	
<i>Macrobrachium rosenbergii</i> nodavirus (MrNV)	<i>Macrobrachium rosenbergii</i> (Giant river prawn) (8)
<i>Penaeus vannamei</i> nodavirus (PvNV)	<i>Penaeus vannamei</i> (now <i>Litopenaeus vannamei</i> , Pacific white shrimp) (255)
Bat Guano Isolates	
Bat guano-associated nodavirus (BGNV)	Unknown (isolated from guano of the bat <i>Antrozous pallidus</i>) (149)

the range of this family and the potential interactions with other hosts and vectors (149). A wide variety of alpha- and betanodaviruses have been identified in water samples from Lake Needwood in Maryland, USA (64). The viral sequences found include NoV (alpha), *Atlantic cod nervous necrosis virus* (**ACNV**, beta), AHNV (beta), *Boolarra virus* (**BoV**, alpha), PaV (alpha), WhNV (unclassified), *Dicentrarchus labrax nervous necrosis virus* (**DIEV**, beta), and FHV (alpha). An updated phylogenetic analysis of these and other nodaviruses is presented in **Appendix I** of this dissertation.

Nodamura virus. NoV was isolated from *Culex tritaeniorhynchus* mosquitoes in 1956 during a screen for *Japanese encephalitis virus* in Nodamura, Japan using a pig-baited Magoon trap (220). Although it has not been shown to infect humans, NoV-seroreactive (neutralizing [**N**] antibody producing) pigs and herons were found in the region of Japan where NoV was isolated (220, 222). Cattle in Japan that were immunized against bluetongue-like virus appeared to have had either a natural NoV infection prior to vaccination or a parallel NoV infection at the time of immunization (220). Mosquitos can transmit NoV among suckling mice in the laboratory (220) and nursing mothers that eat infected pups were shown to pass immunological protection to the remaining offspring and to foster-fed offspring from unexposed mothers (14, 220).

NoV is also unique in that it infects insects and mammals, including wax moth larvae, suckling mice and suckling hamsters (**Figure 1**) causing fatal hind segment/limb paralysis, respectively (11, 220). Light microscopy examination of tissues from NoV-infected suckling mice revealed necrosis of the spinal cord neurons and brown fat tissues, degeneration of limb skeletal muscle, and atrophy of paravertebral muscles (222). Transmission electron micrographs (**TEM**) shown by Scherer *et al.* (1968) of

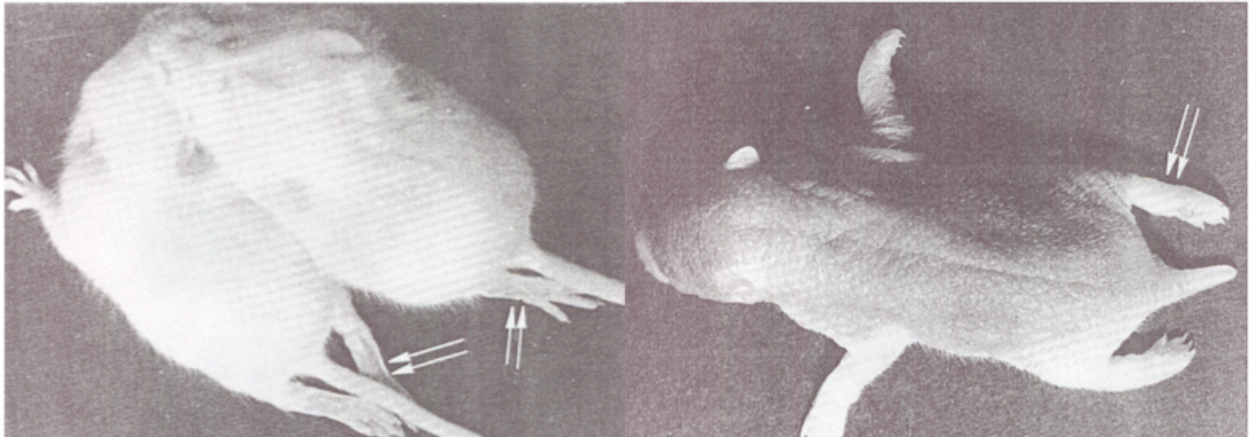


Figure 1: *Nodamura virus* infection in mammals results in fatal hind-limb paralysis. NoV is unique in that it infects both vertebrates and invertebrates, resulting in fatal hind-limb or hind-segment paralysis, respectively. NoV can be transmitted to suckling mice via mosquito transmission. The hind limbs (double arrows) of infected mice (left) and hamsters (right) are afflicted with acute viral flaccid paralysis, causing the hind legs to be dragged. Adapted from Garzon & Charpentier, 1991 (88).

tissues from NoV-infected suckling mice showed that NoV was present in the brain and heart tissues (222). Murphy *et al.* (1970) used TEM to detect NoV in the hind limb skeletal muscles, fibroblasts, macrophages, and liver tissues from infected suckling mice (174). NoV-infected *G. mellonella* tissues examined by light microscopy revealed lesions on nerve ganglia, in muscle cells and in the salivary and molting glands (86).

Both NoV-infected suckling mice and *G. mellonella* larvae exhibit an array of cytopathology including: accumulation of a virogenic stroma comprised of smooth membrane vesicles, increases in ribosomes and polysomes, deformed and swollen mitochondria, and membrane-enclosed paracrystalline arrays of viral particles (86, 174). Cytoplasmic vesicular accumulation and double-membrane bound viral particles are characteristic of enterovirus infection (223, 224). Murphy *et al.* (1970) showed that NoV-infected liver Kupffer cells from suckling mice contained large double membrane enclosed paracrystalline arrays of particles (174) that greatly resemble the autophagosomes observed to release poliovirus particles in the absence of cell lysis (138, 258). Garzon *et al.* (1990) studied mitochondrial involvement in NoV infection by TEM and described disorganization of the mitochondrial inner membrane architecture, mitochondrial swelling and aggregation around the nucleus, which all lead to disorganization of the muscle fibrils on the tissue level (**Figure 2**) (87). For a list of organisms supporting NoV infection and RNA replication, refer to **Table 2**.

NoV affects many tissue types in fatally infected animals and the exact cause of death in these animals is not fully understood. Asymptomatically infected mosquitos may carry and transmit NoV and cause fatal paralytic disease in neonates, while other asymptomatic animals are able to control the infection by producing N-antibodies,

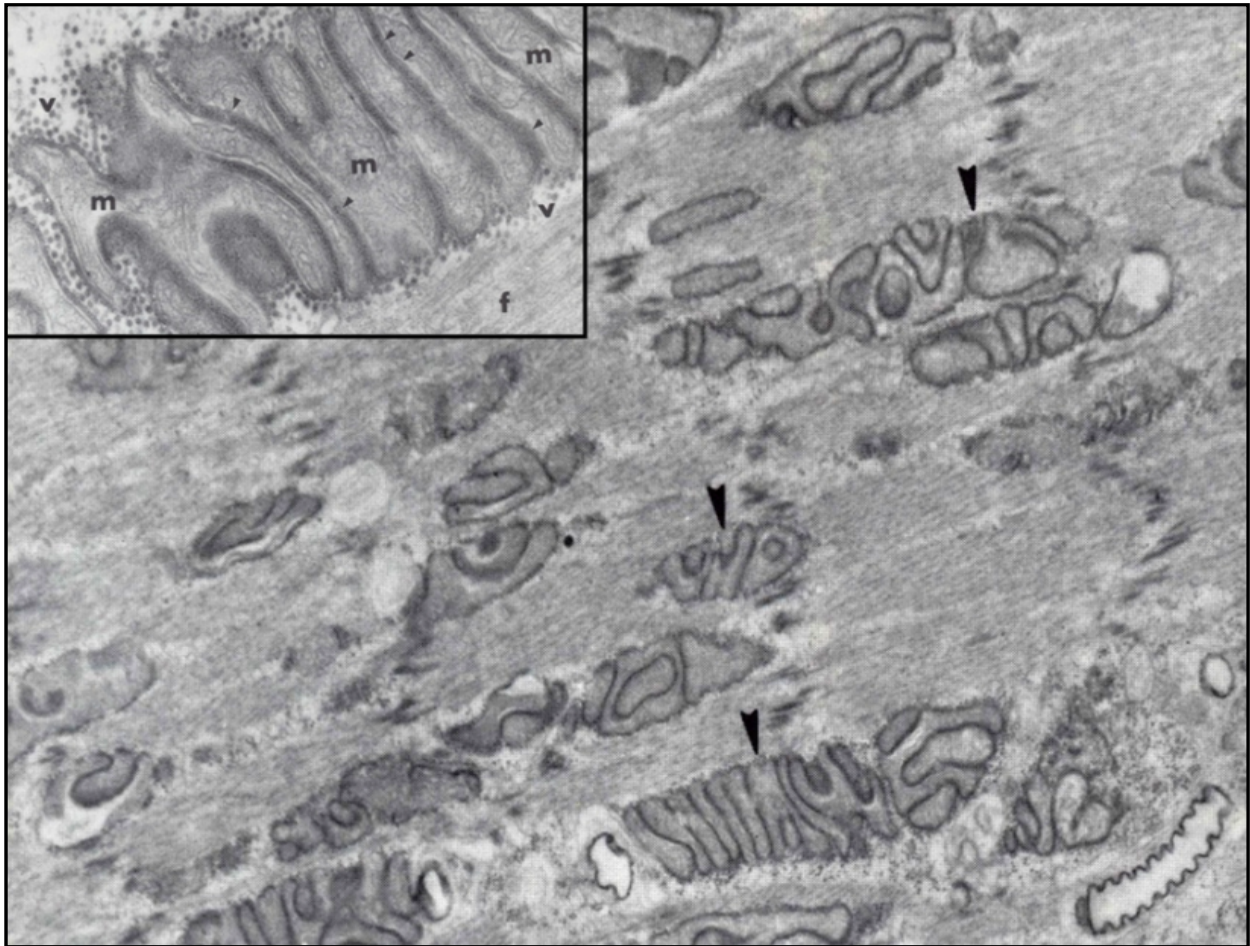


Figure 2: NoV infection induces ultrastructural changes to sarcosomes of infected *G. mellonella* larva muscle cells. Transmission electron micrograph of NoV-infected *G. mellonella* larva muscle tissue reveals the clustered and fused sarcosomes (mitochondria) with a mostly elongated tubular morphology. Areas where these stacked mitochondria appear fused by their outer membranes (long arrows) are noted and may be induced by NoV infection. The fused mitochondria are associated with an electron dense paracrystalline array of viral particles (inset, v). Inset: magnified image of approximately 10 fused mitochondria highlighting the disruption of myofibrils (f) in the sarcoplasm, loss of mitochondrial cristae, and sharing of the mitochondrial matrices (m). Adapted from Garzon & Charpentier, 1991 (88).

suggesting there may exist a natural host-vector reservoir system harboring NoV in Japan and perhaps elsewhere, based on the metagenomic studies described earlier. Many of these studies used EM to study the morphology of nodavirus particles and viroplasm in infected cells and animal tissues. Extensive work was performed to characterize the structure of the nodavirus particle, its geometric symmetry and the contents of a mature nodaviral capsid. The results of these structural and genomic encapsidation studies are briefly summarized in the next section.

1.3 Nodavirus Virion Structure and Genome Packaging

The structure of a nodavirus particle is characterized by its small size, absence of a lipid envelope and an icosahedral capsid encasing a bipartite positive-strand RNA genome. The nodavirus coat protein (**CP**), protein alpha (**α**), is encoded by the RNA2 genome segment and undergoes autocatalytic cleavage after assembly to produce proteins beta (**β**) and gamma (**γ**), which is required to form a mature infectious particle (225). Cleavage of protein **α** does not go to completion, leaving 10-25% of protein **α** uncleaved for BBV and FHV, but this is sufficient to confer infectivity on the particles (118). [³⁵S]-labeled NoV particles purified from cells expressing both NoV genomic segments contain protein **α** and one of its cleavage products, protein **β** (124). Johnson *et al.* (2003) found that protein **γ** was not detected in the viral preparation because the radiolabeled residue (Met) remained with protein **β** after cleavage (124). However, protein **γ** was detected by Western blot in cells expressing NoV RNA1 and RNA2 suggesting NoV undergoes maturation cleavage of protein **α** into proteins **β** and **γ** (124).

Table 2: Organisms and cells permissive to NoV infection or RNA Replication.

Organism/Cell type	Species common name
<i>Aedes aegypti</i> ¶#	<i>Aedes</i> Mosquito (12, 220)
<i>Aedes albopictus</i> ¶#	<i>Aedes</i> Mosquito (12, 259)
<i>Aedes albopictus</i> (ATC-15) cells #	<i>Aedes</i> Mosquito (198)
<i>Aedes pseudoscutellaris</i> (AP-61) cells #	<i>Aedes</i> Mosquito (198, 259)
African green monkey kidney (Vero) cells \$	Monkey (125)
<i>Anopheles albimanus</i> (alb) cells \$#	<i>Anopheles</i> Mosquito (198)
<i>Anopheles gambiae</i> (MOS-55) cells \$#	<i>Anopheles</i> Mosquito (198)
<i>Apis mellifera</i> ¶	Honeybee (11)
Baby hamster kidney (BHK-21) cells #	Syrian hamster (12, 14, 177)
Baby hamster kidney (BSR-T7/5) cells #	Syrian hamster (124)
Chinese hamster ovary (CHO) cells \$	Chinese hamster (14)
<i>Culex tarsalis</i> ¶	<i>Culex</i> Mosquito (220)
<i>Culex tritaeniorhynchus</i> *¶	<i>Culex</i> Mosquito (220)
<i>Drosophila</i> (Schneider's) line 1 (DL1) cells \$	<i>Drosophila</i> (14, 82)
<i>Galleria mellonella</i> larvae ¶	Greater wax moth (11, 12, 86)
<i>Helicoverpa zea</i> (FB33) cells #	Corn earworm (198)
Human bone osteosarcoma (143B) cells \$	Human (14)
Human epithelial adenocarcinoma (HeLa) cells \$	Human (14)
Human epithelial (HEp-2) cells \$	Human (14)
Monkey (BSC40) cells \$	Monkey (14)
Mouse fibroblast (C127) cells \$	Mouse (14)
<i>Ornithodoros savignyi</i> ¶	Soft-bodied tick (220)
<i>Plodia interpunctella</i> larvae ¶	Indian meal moth larvae (220)
Porcine kidney (PK15) cells \$	Porcine (14)
Primary chicken embryo fibroblasts (CEF) \$	Chicken (14)
<i>Saccharomyces cerevisiae</i> \$	Budding yeast (202)
Suckling <i>Mesocricetus auratus</i> ¶	Syrian hamster (222)
Suckling <i>Mus musculus</i> ¶	Mouse (222)
<i>Toxorhynchites amboinensis</i> ¶	<i>Toxorhynchites</i> Mosquito (259)
<i>Toxorhynchites amboinensis</i> (TRA-171) cells #	<i>Toxorhynchites</i> Mosquito (125, 198)
Turtle heart cells \$	Turtle (14)

*Potential natural host; ¶ whole animal infection; # infection of cultured cells; \$ supports NoV RNA replication after transfection

Table 2 Continued: Organisms and cells permissive to NoV infection or RNA Replication.

Other (Near NoV Isolation Location)	Detail
<i>Sus scrofa domestica</i> Domestic pigs *	Produce NoV neutralizing (N) antibodies (222)
<i>Nycticorax nycticorax</i> Herons	Produce NoV N antibodies (222)
<i>Oryctolagus cuniculus</i> Rabbits	No illness, produce N antibodies after infectious challenge (222)
<i>Bos taurus</i> Cattle	Natural infection with NoV before or in parallel with bluetonguelike virus immunization (220)

*Potential natural host; ¶ whole animal infection; # infection of cultured cells; \$ supports NoV RNA replication after transfection

There are currently no solved crystal structures of complete betanodavirus particles to study whether these viruses undergo this maturation cleavage process (120, 257)

High-resolution 3D structures for BBV, FHV, NoV and PaV particles have been solved using x-ray crystallography and cryo-EM (117, 118, 256, 282). Nodaviral particles are comprised of 180 CP subunits that encase a single strand each of RNAs 1 and 2 forming a 29-32 nm (exterior diameter) icosahedral capsid structure with T=3 symmetry (**Figure 3**) (118, 174). Cryo-EM was used to determine *malabaricus grouper nervous necrosis virus* (**MGNNV**) virus-like particles (**VLPs**) have T=3 symmetry, but the CP has two domains with high similarity to tombusvirus and calicivirus members not seen on alphanodavirus capsids, suggesting the betanodaviruses have a slightly different exterior capsid structure (257). Tang *et al.* (2001) described a dodecahedral cage structure of partially double-stranded genomic RNA underlying the protein capsid, which these authors interpreted as being formed via interactions between the N-

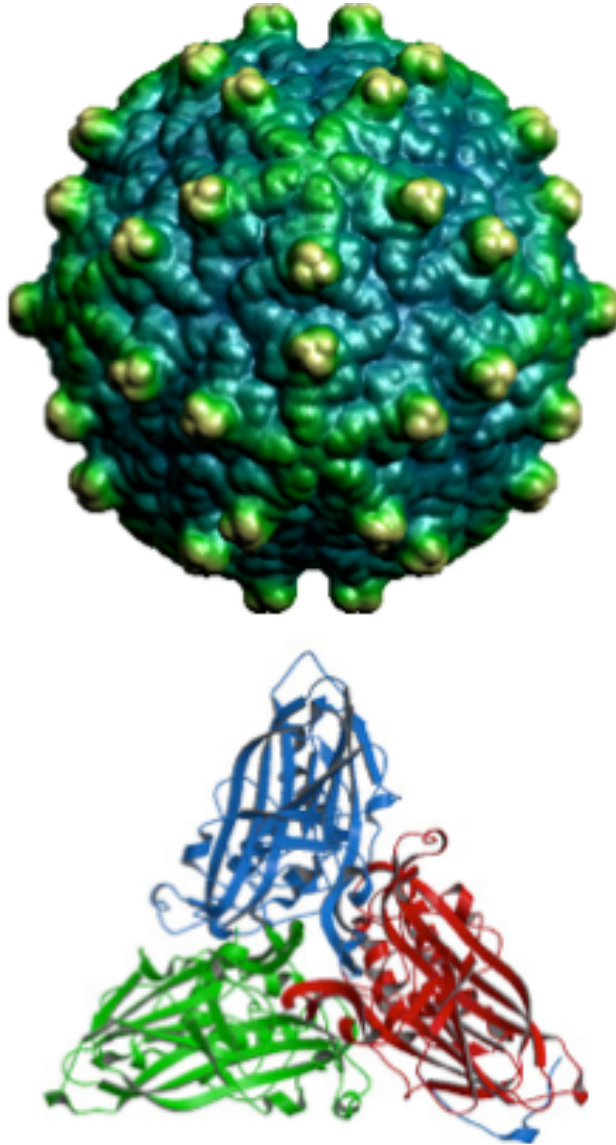


Figure 3: *Nodamura virus* particle and coat protein structure. Above: The three-dimensional structure of the complete NoV particle has been solved using x-ray crystallography (296). The NoV capsid is comprised of 180 protein α subunits (below) arranged with icosahedral symmetry, forming a $T = 3$ structure. Protein α is cleaved during particle maturation to produce proteins β and γ found in the virion. Image source: http://viperdbscripps.edu/info_page.php?VDB=1nov.

terminal basic residues of the CP and the RNA genome (256). This finding suggests that coordinated interactions between the elements within the CP structure and the genomic RNA structure and sequence are critical to encapsidation and virion assembly, but the mechanism in which the nodavirus genome is specifically recognized for packaging is poorly understood. Re-evaluation of the cryo-EM structure data previously generated for FHV revealed the presence of a similar RNA cage structure not previously described in the literature (261); presumably one is also formed from the structurally similar NoV (296).

Nodavirus particle assembly is a dynamic process, as many studies on FHV encapsidation illustrate. FHV RNA1 is not required for particle assembly and maturation when RNA2 is expressed in insect cells, and particles formed in the absence of RNA1 replication (226). The FHV CP has residues on both termini that are involved in recognition and co-packaging of each genomic segment independently of each other (228). Venter *et al.* (2009) showed this RNA co-packaging is mediated in part via an arginine-rich motif (**ARM**) on the CP N-terminus, which specifically recognizes and packages RNA1 (273). The RNA binding activity of the CP is further complimented by the basic and aromatic residues on the N- and C-termini (55, 67, 175). FHV protein γ uses three C-terminal phenylalanine residues to selectively interact with genomic RNAs and mutations at these sites result in progeny packaging a mixture of viral and cellular RNAs (228). The N-terminus of FHV protein β contains sequences that are responsible for trafficking the CP to replication complexes and specifically packaging both genomic segments independent of each other (162, 272). Genomic RNA2 plays its role in encapsidation by utilizing a bulged stem-loop as a packaging signal (294). Venter *et al.*

(2007) found that FHV CP encapsidates the FHV genome if the CP was synthesized from a replicating RNA template, whereas the particles that assembled from CP that synthesized from a non-replicating template packaged random cellular RNAs with the same duplexed dodecahedral cage described above (271). Nodaviruses appear to have adapted to maximize their CP usage potential by requiring their CPs to not only preferentially interact with genomic RNA when it is present, but also interact with cellular RNAs when viral segments are not present. Consequently, FHV does not form VLP like other RNA viruses (89), although its CP will package a steady amount of RNA into a capsid whether it is viral or cellular (94).

In addition to its role in encapsidation, the nodavirus CP confers stability and protection to the particle under physical and chemical assaults. Several nodavirus particles are resistant to 1% SDS (except BoV) (113), and mature FHV particles resist 1% deoxycholate, 1 M urea, 20 mM EDTA or 1% SDS plus either 10 mM magnesium or calcium ions (83). Gallagher and Rueckert (1988) noted that immature FHV particles were more susceptible to these treatments and lost significant infectivity after treatment. Mature FHV particles remain stable after freezing and incubation at 40°C for 10 minutes, but lose 91% and 99% infectivity at 53°C and 58°C, respectively (227, 232). NoV, FHV and BBV remain stable at pH 3, but NoV is unstable in solutions containing chloride ions (174, 179, 232).

NoV uniquely combines the properties of arbovirus transmission with the physical and pathogenic characteristics of a paralytic picornavirus. NoV can be experimentally transmitted to mammalian hosts via a mosquito vector, but the significance of this transmission in the ecology of the virus is unknown. Unlike officially recognized

arboviruses such as *Dengue virus* (**DENV**) and *Tick-borne encephalitis virus* (**TBEV**), NoV lacks a lipid envelope, as evidenced by its resistance to lipid solvent treatment and subsequent appearance of particles seen by EM after infection (88, 220-222). NoV resembles a picornavirus with its small particle size, positive-sense RNA genome, and paralytic disease. However, NoV lacks the hallmarks of picornavirus genome structure such as polyadenylation, internal ribosome entry sites (**IRES**), or genome-linked viral proteins (**VPg**) (20, 75, 178, 194, 243). For these reasons and because it did not share immunogenicity with any known virus at the time of its discovery, NoV was defined as the type species of a new virus family, the *Nodaviridae* (180).

The nodavirus capsid is a shell protecting the secrets encoded by this simple, yet complex virus. Once a mature NoV particle enters the cell by binding to a yet-to-be determined receptor, the capsid releases its message into the cytoplasm where the awaiting ribosomes translate it. The organization of these viral messages and the products they encode are considered in the next section.

1.4 Nodavirus Genome Organization

Nodaviruses have a bipartite, single-stranded positive-sense RNA genome. The mRNA-sense genomes are infectious in the sense that their delivery into the cell by transfection of purified virion RNA or cDNA copies of the genomic RNA will initiate a complete replicative cycle and produce infectious virions (13, 14). The total genetic material of NoV is approximately 4.5 kb in length and encodes 4 proteins. The 3' ends of the genomic and subgenomic RNAs lack polyadenylation (178) and are resistant to chemical modification due to the high degree of RNA secondary structure, which is important for RNA replication and packaging (212, 294). The viral RNA segments are 5'-

capped with a monomethylated 5' ^{m7}GpppG (cap zero) structure (124, 178), which is presumably catalyzed by a predicted methyltransferase-guanylyltransferase (**MTase-GTase**) core region on the nodavirus RNA dependent RNA polymerase (**RdRp**) (5).

Genome replication and capsid functions are divided between RNA1 and RNA2, which are co-packaged into the same virion and both of which are required to produce infectious progeny (**Figure 4**). NoV RNA1 (3204 nt for NoV) encodes the 110 kDa protein A (**NA**), the viral contribution to the RdRp. NoV RNA2 (1336 nt) encodes the 43 kDa protein alpha, which is cleaved upon assembly into proteins beta (40 kDa) and gamma (3 kDa). This process was described in further detail in the previous section (**1.3**). NoV subgenomic RNA3 (472 nt) is synthesized during RNA1 replication and is not encapsidated into progeny virions. RNA3 is 3' co-terminal with RNA1 and the 5' end of RNA3 corresponds to nucleotide 2732 on RNA1 (124, 128). NoV RNA3 encodes protein B1 and two versions of protein B2 from separate and overlapping open reading frames (**ORFs**), in which the B2 ORF extends slightly past the B1 and NA ORFs (124). For FHV, the orientation of the B1 and B2 protein ORFs on RNA3 are switched and Boolarra virus does not encode a B1 protein (110). Proteins B1 and NA are encoded by the same ORF such that B1 represents the C-terminal fragment of NA. For NoV the function of B1 is currently unknown and B2 inhibits the RNAi response in insect, plant and mammalian cells (125, 148, 251); FHV B2 also suppresses RNAi in insect, plant, mammalian cells, and in *Drosophila melanogaster* and *Caenorhabditis elegans* animals.

The betanodavirus *redspotted grouper nervous necrosis virus* (**RGNNV**) protein B2 initiates apoptosis when expressed in grouper liver cells (**GL-av**) where it was shown

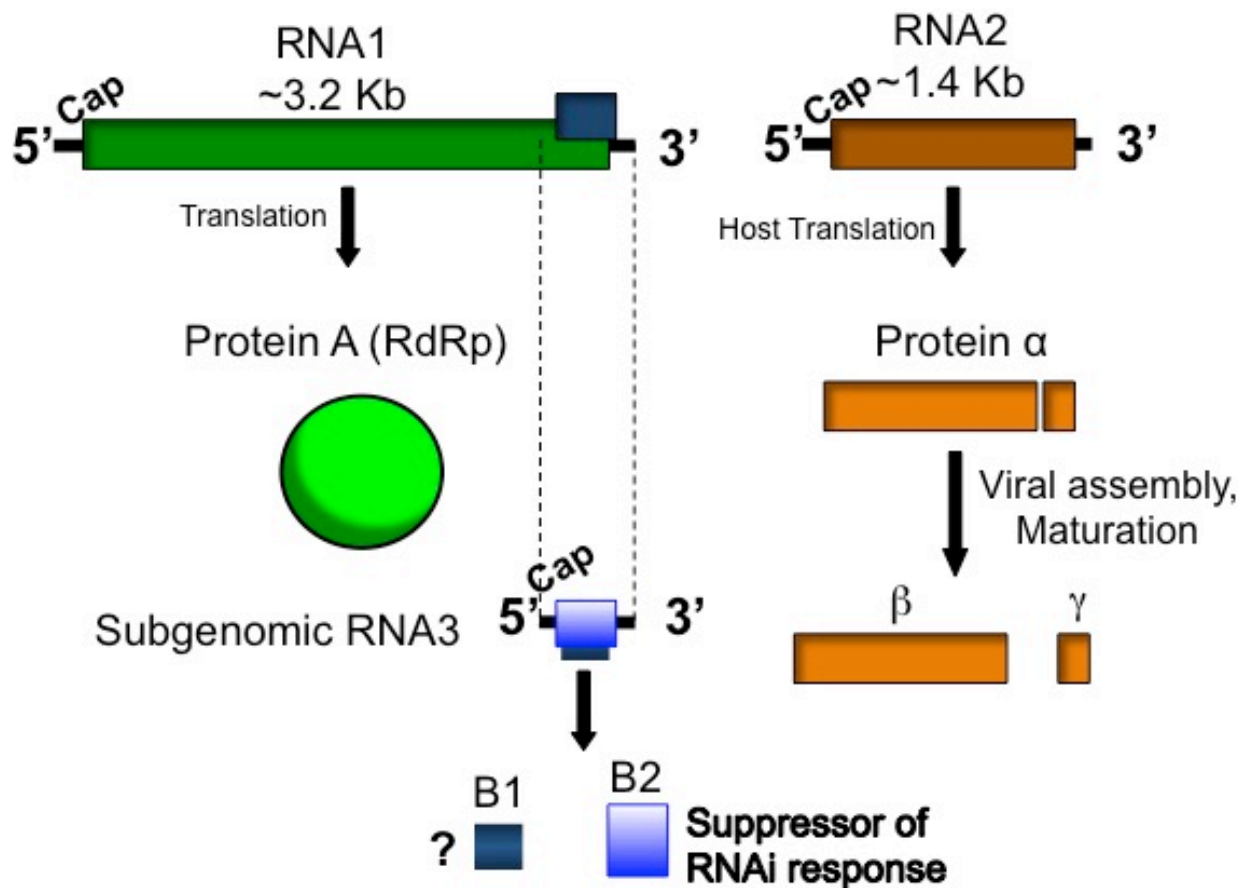


Figure 4: Schematic of the nodavirus genome organization. Genomic RNAs 1 and 2 are co-packaged into virions and both are required for infectivity. RNA1, 3204 nt for NoV, encodes the viral contribution to the NoV RdRp, protein A (**NA**). RNA2, 1336 nt for NoV, encodes the capsid precursor, **α**, which undergoes an autocatalytic maturation cleavage to produce proteins beta (**β**) and gamma (**γ**) on the mature particle. During RNA1 replication, subgenomic RNA3 is synthesized. RNA3 is 3' co-terminal with RNA1 and encodes proteins B1 and B2. For NoV, the function of B1 is currently unknown, and B2 inhibits the cellular RNAi response. Adapted from Johnson *et al.* 2003 (124).

to upregulate pro-apoptotic Bax expression and induce the loss of mitochondrial membrane potential (**MMP**) (249). It was later shown that RGNNV B2 contains a mitochondrial targeting signal (**MTS**) that traffics B2 to the mitochondrial matrix where it inhibits complex II activity (ATP synthesis) in fish (**GF-1**) and human (**HEK293T**) cells (250). Such localization to mitochondria has not been described for the FHV and NoV B2 proteins and, while FHV does induce apoptosis in cultured cells (234). NoV apparently does not induce apoptosis during infection (124) or expression of RNA1 (84). RGNNV protein B1 was shown to inhibit the pro-apoptotic effects of B2 early during expression (45).

After the nodavirus RdRp is synthesized, RNA replication ensues and the next major step of the life cycle begins. During this phase in the replicative cycle, the cell accumulates viral genomic RNA to levels comparable to the cellular ribosomal RNA (**rRNA**), such that it can be readily detected on a denaturing formaldehyde-agarose gel by staining with EtBr. The following section is a brief summary of this process.

1.5 Nodavirus RNA Replication

The mechanism of nodavirus RNA replication in cells (**Figure 5**) has been studied extensively but many details remain to be determined (13, 14, 16, 81). Upon cell entry, the nodavirus genome is released into the cytoplasm, possibly by a co-translational mechanism, where ribosomes pull the RNA from the capsid as described for *Semliki forest virus* (264) and *Tobacco mosaic virus* (235). NoV RNA replication begins when NA binds to a *cis*-acting RNA signal in RNA1 and synthesizes a negative-strand replication intermediate, which serves as a template to synthesize high levels of

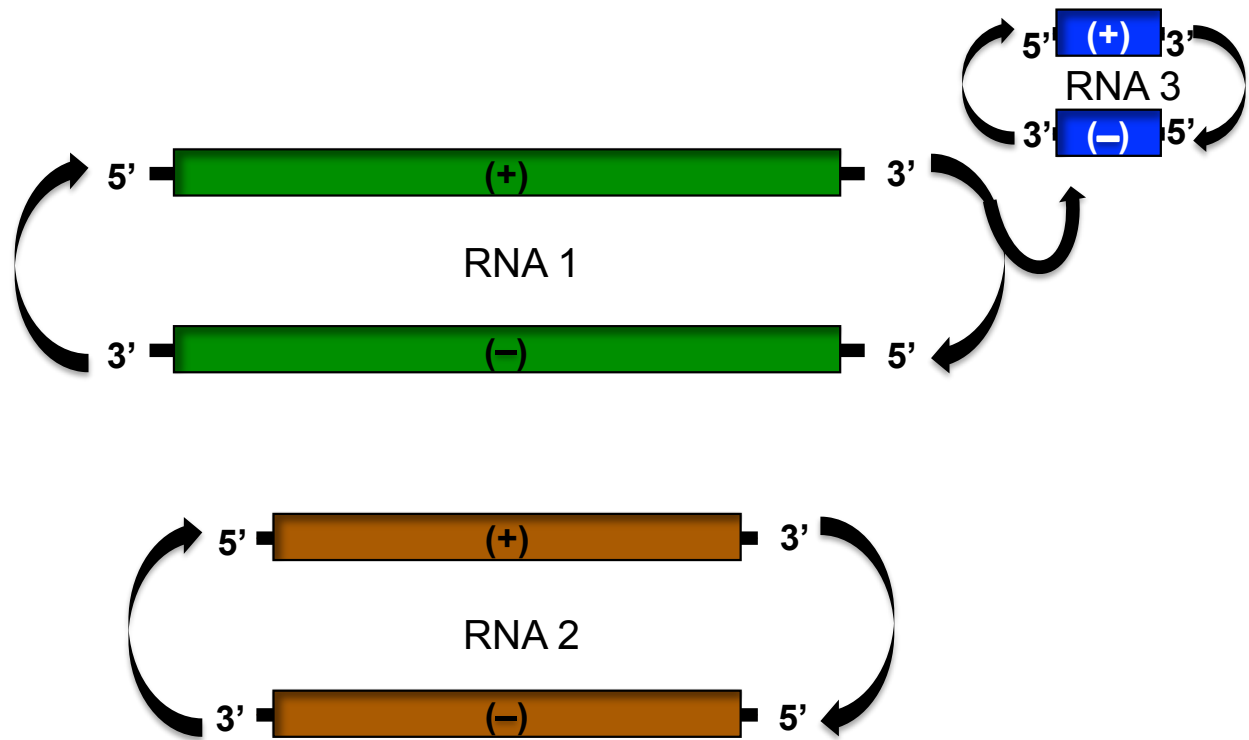


Figure 5: Schematic of nodavirus RNA replication. Once the RdRp is translated from RNA1, it begins to synthesize negative strand replication intermediates of RNA1 and subgenomic RNA3. These are subsequently used as templates for synthesis of further positive strands. In the presence of RNA2, it is also replicated via negative strand replication intermediates. The progeny positive strands can be used for translation, co-packaging of the genomic RNAs into progeny virions, or as templates for synthesis of more replication intermediates. The RdRp activity (curved arrows) is essential for RNA replication and for infectivity.

positive-strand genomic RNAs with a ratio of positive- to negative-sense molecules of approximately 100:1 (1, 16). A 3' stem loop structure on RNA1 may serve as the *cis*-acting signal as shown for NoV RNA2 (212), while a recently-defined 3'-terminal structural element may serve a similar function for RNA1 (92). The catalytic activity of the nodavirus RdRp is unhindered by actinomycin D (**ActD**), which blocks DNA-dependent RNA synthesis, allowing for labeling of the RdRp-specific products with modified (e.g., radioactively tagged or Br-labeled) nucleotides (14, 16, 81, 84).

Nodavirus RNA replication relies on intracellular membranes and lipids, but the role of membranes in nodavirus RNA replication and RNA synthesis initiation are not yet clear. BBV and FHV protein A activity is dependent on membrane association *in vitro* and solubilization of protein A from membrane-containing fractions results in loss of RdRp activity as measured by incorporation of [³H]-uridine (103, 284). Studies using membrane-bound FHV protein A (**FA**) purified from infected cells showed FA synthesizes negative-strand copies, but was unable to synthesize positive-strand genome copies (284). Upon addition of glycerophospholipid (**GPL**) to the *in vitro* system, the polymerase extract was able to synthesize single-stranded positive-strand RNA, suggesting a role for lipids in RNA synthesis initiation. Initiation of a new strand from a template by the FHV RdRp has been shown to occur in a primer-independent fashion (*de novo*) in an *in vitro* replicase assay (286), which has also been described for bacteriophage Q β (252) and *Hepatitis C virus* (**HCV**) (206). Further biochemical studies are required to understand how the presence of lipids allows *de novo* RNA synthesis to proceed for nodaviruses.

Deletion of the membrane-associated regions (**MARs**) from the NoV RdRp severely inhibits accumulation of negative-stranded RNAs 1 and 3 and abolishes accumulation of the positive-strand complements (84). WhNV protein A is a transmembrane protein and its attachment to the outer mitochondrial membrane (**OMM**) is required for the polymerase to recruit and accumulate RNA synthesis products (204). These observations suggested nodavirus RdRps are dependent on membrane and/or lipid associations that are required for some steps in RNA replication (285). Further consideration of nodaviral RdRps, membranes and RC formation is further discussed in **section 1.7**.

Nodavirus RNA replication is temperature sensitive with NoV RNA1 replication being more thermostable than that of FHV RNA1 replication. NoV RNA1 and RNA3 replication is stable at temperatures ranging from 28°C to 37°C (14). However, NoV RNA2 replication is significantly reduced at temperatures higher than 30°C (Johnson and Ball, unpublished data), which we interpret as meaning that NoV protein A may have a *cis*-preference (preferential replication of the RNA1 template that encodes it), at least early in infection, or that there is selective pressure to maintain replication of RNA1 higher temperatures, thereby ensuring survival of the genome propagation mechanism in cells. Dasgupta *et al.* (1994) discuss this further with regards to *Drosophila* cells persistently-infected with FHV, where FHV RNA2 accumulated mutations leading to smaller virus plaques and relieving the virus of needing to produce functional CP in the absence of RNA packaging and virion assembly (57). Following prolonged time course analyses that compared the kinetics of NoV RNA replication in NoV-infected baby

hamster kidney BHK-21 and mosquito TRA-171 cells, Johnson *et al.* (2003) suggested that NoV may establish persistent infections in mammalian cells (124).

NoV and FHV RdRps have unique template specificities. Gallagher (1987) performed a study of the alphanodavirus protein A RNA template specificity using purified genomic RNA segments from BBV, BoV, FHV and NoV to transfect *Drosophila* cells (82). In this study, NoV protein A did not replicate the RNA2 segment from BBV, BoV and FHV; however, FHV protein A replicated BoV RNA2 (82). Price *et al.* (2005) found a NoV RNA1 mutant bearing the R59Q mutation in B2 was able to support heterologous replication of FHV RNA2-based replicons in yeast cells to yield RdRp activity-dependent yeast colony formation, but only under selective pressure (200).

Because it encodes the viral RdRp, NoV RNA1 is able to replicate autonomously in the absence of RNA2 or the protein products it encodes, yielding high accumulation of RNAs 1 and 3, comparable to levels of cellular ribosomal RNA (13, 14, 81, 123, 124). This useful characteristic makes NoV reverse genetics attractive for robust heterologous expression of foreign proteins, including chloramphenicol acetyl transferase (**CAT**), the cystic fibrosis transmembrane regulator (**CFTR**), green fluorescent protein (**GFP**) (Johnson and Ball, unpublished observation) and the yeast HIS3 gene (202), in many cells types (**Table 2**). During NoV infection or transfection of NoV genomic RNA, synthesis of RNA1 and RNA3 occurs first with RNA2 synthesis occurring only after RNA3 replication and both genomic RNAs are synthesized up to 30 hours post-infection (14, 180). After RNA2 synthesis commences, RNA3 replication ceases and the capsid protein precursor, α , becomes the most abundantly translated viral protein.

RNA2 and RNA3 are involved in a counter-regulatory relationship where RNA3 synthesis initially occurs and its accumulation activates RNA2 synthesis *in trans* (**transactivates**) (68). Subsequent accumulation of RNA2 provides feedback to suppress RNA3 replication (81, 295). Eckerle *et al.* (2002) showed that FHV RNA2 replication does not commence in a mutant genome that does not synthesize RNA3, independently of the RNA3 translation products B1 and B2, and that exogenously supplied RNA3 could rescue this lack of RNA2 replication (68). Johnson *et al.* (2003) and Price *et al.* (2005) provided evidence that NoV RNA3 replication was required for replication of RNA2 in mammalian cells and in yeast, which simultaneously showed the counter regulatory transactivation/suppression mechanism occurs for also for NoV and corroborated the above results from mammalian cells for FHV by Eckerle *et al.* (2002) (124, 202). It is proposed that RNA2 transactivation prevents uncoordinated RNA synthesis and subsequent imbalanced protein synthesis, thereby leading to synthesis of roughly equal amounts of genomic strands for encapsidation. For this reason, RNA2 and RNA3 are considered to be counter-regulatory (68).

Replication of RNA1 initiates synthesis and RdRp-catalyzed replication of subgenomic RNA3. The mechanism of initiating N3 synthesis from an N1 template has yet to be uncovered, but there are two proposed mechanisms for synthesis of RNA3 using FHV as a model (69). The first is the internal initiation mechanism, where the RdRp transcribes positive-strand RNA3 from an internal signal on the minus-strand RNA1 strand. The second is the premature termination mechanism, where the RdRp transcribes a minus-strand RNA1 strand from positive-strand RNA1 and prematurely terminates resulting in synthesis of a minus-strand RNA3 strand that is used as a

template to synthesize a positive-strand of RNA3. The presence of RNA3 minus-strands favors the premature termination model. RNA3 synthesis for WhNV has been shown to initiate by internal initiation from a promoter on the negative-sense RNA1 replication intermediate (203), which could suggest that alpha- and betanodaviruses may use different mechanisms for RNA3 synthesis.

During FHV and NoV RNA replication, the RdRp synthesizes single-stranded head-to-tail homodimers of covalently linked RNA1, RNA2, and RNA3 (approximately 6408, 2672 and 944 nt for NoV RNA1, RNA2 and RNA3 homodimers, respectively), and covalently linked head-to-tail heterodimers of RNAs 2 and 3 (6, 124, 201, 202). The NoV RNA1 and RNA3 homodimers and NoV RNA1+3 heterodimers were readily detected in previously published works assessing RNA RC formation (84, 212) and are also displayed in this dissertation (**Chapter 2**). The proposed role of the homo- and heterodimers in RNA replication is to serve as replication intermediates, although this remains to be definitively determined (6).

The mechanism of nodavirus RNA replication can be harnessed as a powerful tool for biological sciences to study aspects of the RNA virus replicative cycle in different host cells, to characterize host-protein interactions, or expresses heterologous genes in cells using the nodaviral RdRp to replicate genes in the context of RNA replicons, among other experimental opportunities. Years of impactful studies with nodavirus replication systems will be briefly considered in the next subsection, since they provide a means of initiating synthesis of primary transcripts in a wide variety of cell types.

1.6 RNA Replication Systems

NoV RNA replication can be propagated in a variety of cells and tissues following either viral infection, or by transfection of viral RNA or of plasmids encoding NoV cDNA clones (14, 124, 199, 202, 259). As reviewed in **section 1.2**, NoV can infect suckling mice, suckling hamsters, and a variety of arthropods including mosquitoes, honeybees, soft-bodied ticks, and larvae of the greater wax moth *Galleria mellonella* (**Table 2**) (220-222, 259). When introduced by transfection, NoV RNA can replicate in a wide variety of cell types (**Table 2**). These attributes make NoV an attractive and versatile model system to study positive-sense RNA viruses safely. Two key technologies have immensely enhanced our ability to study these viruses: recombinant DNA technology and viral reverse genetics. In 1981, Racaniello and Baltimore generated a full-length cDNA clone of the *poliovirus* positive-strand RNA genome that could initiate a complete viral infectious cycle in transfected mammalian cells, including production of infectious particles (205). Three years later, Ahlquist *et al.* reported the generation of cDNA clones of *Brome mosaic virus* (**BMV**) and the infectivity of *in vitro* transcribed RNAs from these clones in barley seedlings (2, 3, 205). Soon after, Dasmahapatra *et al.* reported the first use of cDNA clones of an animal virus (the alphanodavirus black beetle virus, BBV) to produce RNA transcripts that are infectious to cultured *Drosophila* cells (58). Early attempts to launch nodaviral RNA replication from DNA used linearized plasmids encoding cDNA copies of genomic sequence under SP6 transcriptional control. These plasmids resulted in RNA1 transcripts with 20 additional 5' nucleotides and 4 additional nucleotides on the 3' end. These transcripts retained up to 10% infectivity compared to

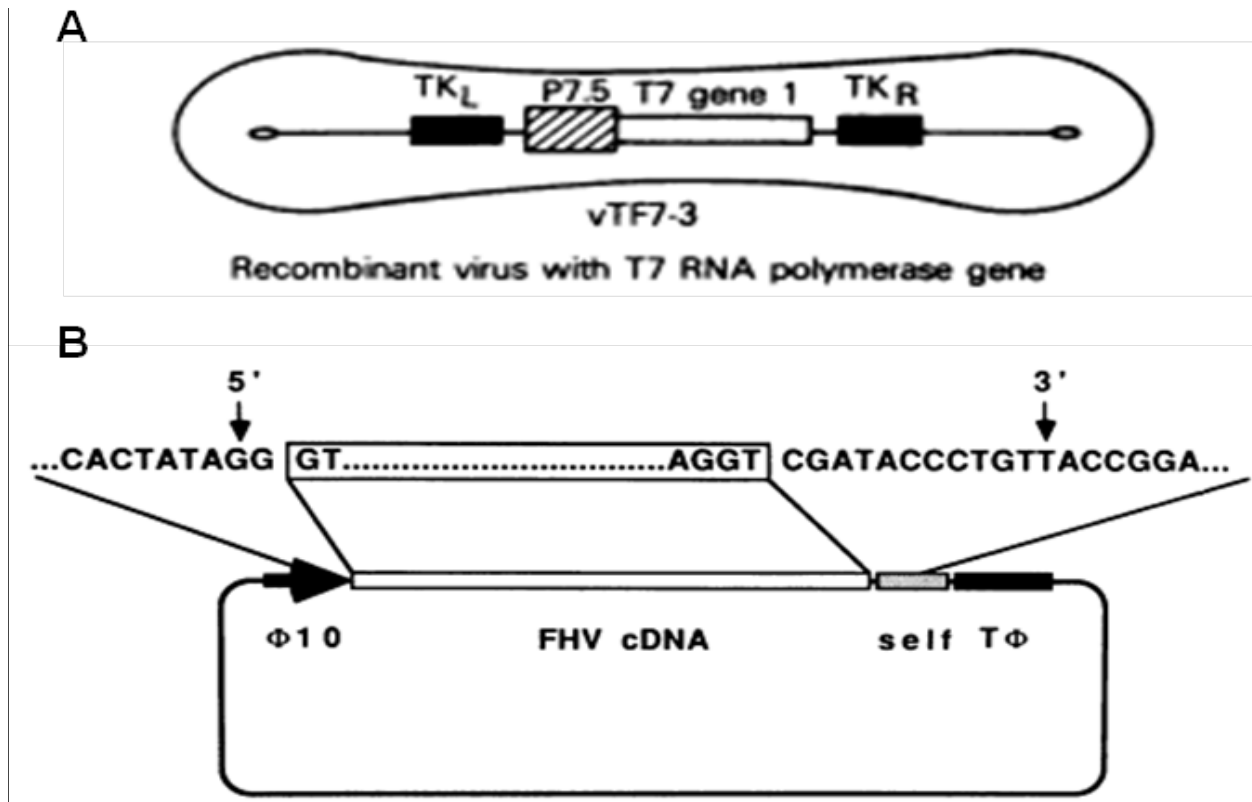


Figure 6: FHV cDNA expression using a recombinant Vaccinia viral vector. (A) Recombinant vaccinia virus vector engineered to express bacteriophage T7 RNA polymerase in cells. Adapted from Fuerst *et al.* 1986 (79). This vector is used to drive transcription of (B) T7 expression vectors that contain the full-length cDNA of FHV genes (13). These plasmids contained the full-length cDNA copies of FHV RNA1 or RNA2 (open box) preceded by a T7 bacteriophage promoter sequence (Φ10) and followed by a sTobRV self-cleaving ribozyme (self) and ending with a T7 bacteriophage transcription termination sequence (TΦ). Adapted from Ball *et al.* 1992 (13).

that of purified virion RNA and the RdRp did not copy the additional 5' nucleotides. However, internal sequences within the ORF would be copied by the replicase (58).

The Ball lab generated the first expression system that replicated the full-length genome of FHV. This system used a previously-developed recombinant vaccinia virus vector to express bacteriophage T7 RNA polymerase (**Figure 6A**) in the cytoplasm of infected baby hamster kidney cells (**BHK21**) to drive primary transcription of FHV cDNAs from T7 expression vectors (79). The plasmids contain the full-length cDNA copies of the FHV genome segments, each upstream of a self-cleaving ribozyme from satellite tobacco ringspot virus (**sTobRV**) followed by a T7 transcriptional terminator (**Figure 6B**). Primary transcripts from these plasmids were capable of protein synthesis and replication, but the transcripts still contained 12 additional 3' nonviral nucleotides derived from the sTobRV ribozyme (13, 79). The sTobRV ribozyme was later replaced with the antigenomic ribozyme from hepatitis delta virus (**HDV**), which is able to self-cleave without adding any exogenous nucleotides (195). Ribozyme cleavage yields an authentic 3' viral end on the primary transcripts, thereby increasing the accumulation of RNA1 replication products (16, 17, 195).

Further experimentation led to the construction of the T7 expression plasmid FHV1(1,0), which expresses FHV RNA1 that has 1 additional nonviral nucleotide on the 5' end and an authentic 3' viral terminus (hence the nomenclature 1,0). T7 plasmids having no additional 5' nts on FHV RNA1 are unable to produce detectable primary transcripts and launch RNA replication as a result of abortive initiation by T7 RNA polymerase (152). T7 RNA polymerase would stutter over a stretch 4 uracil bases (**U₄**, **Figure 7**) at the 5' end of FHV RNA1 during transcription and become inactivated (17).

<u>RNA1 5' Untranslated Region</u>		
BBV	5'- GUUUUGAAAC	...
FHV	5'- <u>GUUUUC</u>GAAA	...
BoV	5'- GUUUUUCAAC	...
NoV	5'- GUAUUGAAUC	...
PaV	5'- AUGUUGUAGU	...

Figure 7: The 5' untranslated regions of the five alphanodavirus RNA1 segments. The nucleotide sequence of the first 10 bases of RNA1 for each alphanodavirus. Underlined is the U₄ sequence of FHV that causes stuttering of T7 RNA polymerase during transcription of FHV RNA1 cDNA. This U₄ stretch is disrupted in NoV by an adenine at nt 3, allowing transcription of an authentic 5' terminus by placing a T7 promoter just before the NoV sequence [(0,0) configuration]. For PaV the U₄ sequence is also disrupted by a guanine at nt 3. The 5' end sequence of BBV, FHV, BoV and NoV is 5'-GU... while PaV is 5'-AU... This is also true of genomic RNA2 and subgenomic RNA3.

This problem was unique for FHV RNA1 and was not observed when constructing *Pariacoto virus* (**PaV**) or NoV RNA1 T7 expression vectors in the (0,0) configuration (**Figure 7**). Primary transcripts from FHV1(1,0) produce levels of self-directed RNA replication up to 97% of levels produced by purified FHV RNA1. When combined with FHV2(0,0), which expresses FHV RNA2 with authentic termini, this T7 expression system initiates a full FHV replicative cycle. Ball and colleagues showed that it is critical for replication ability to important to maintain the sequence of the 5' and 3' ends of transcripts, since extensions made to the 5' or 3' termini of FHV genome transcripts resulted in loss of infectivity or inability to detect RNA replication in cells (13, 16, 58).

The TVT7R(0,0) vector (126) was critical in moving toward expressing nodavirus genes in cells without the use of a confounding virus vector. Johnson *et al.* (2000) described the construction of TVT7R(0,0): For this vector nodaviral cDNA copies can be inserted between the T7 promoter transcription start site and a self-cleaving HDV ribozyme sequence followed by a T7 transcription terminator (126). This vector facilitates T7 transcription to yield RNA with precise 5' and 3' termini by positioning the cDNA between the transcriptional start site and the ribozyme element (126). The 5' and 3' termini of NoV genomic and subgenomic RNA segments were mapped and full-length NoV cDNA clones were generated and characterized [NoV RNA1: **AF174533**, NoV RNA2: **AF174534**] (124, 128). Soon after PaV was isolated, the 5' and 3' termini of the PaV genome segments were also mapped and the full-length PaV cDNA clones were generated [PaV RNA1: **AF171942**, PaV RNA2: **AF171943**] (**Figure 8B**) (126, 293). The full-length cDNAs of RNA1 and 2 for both NoV and PaV were cloned into TVT7R(0,0)

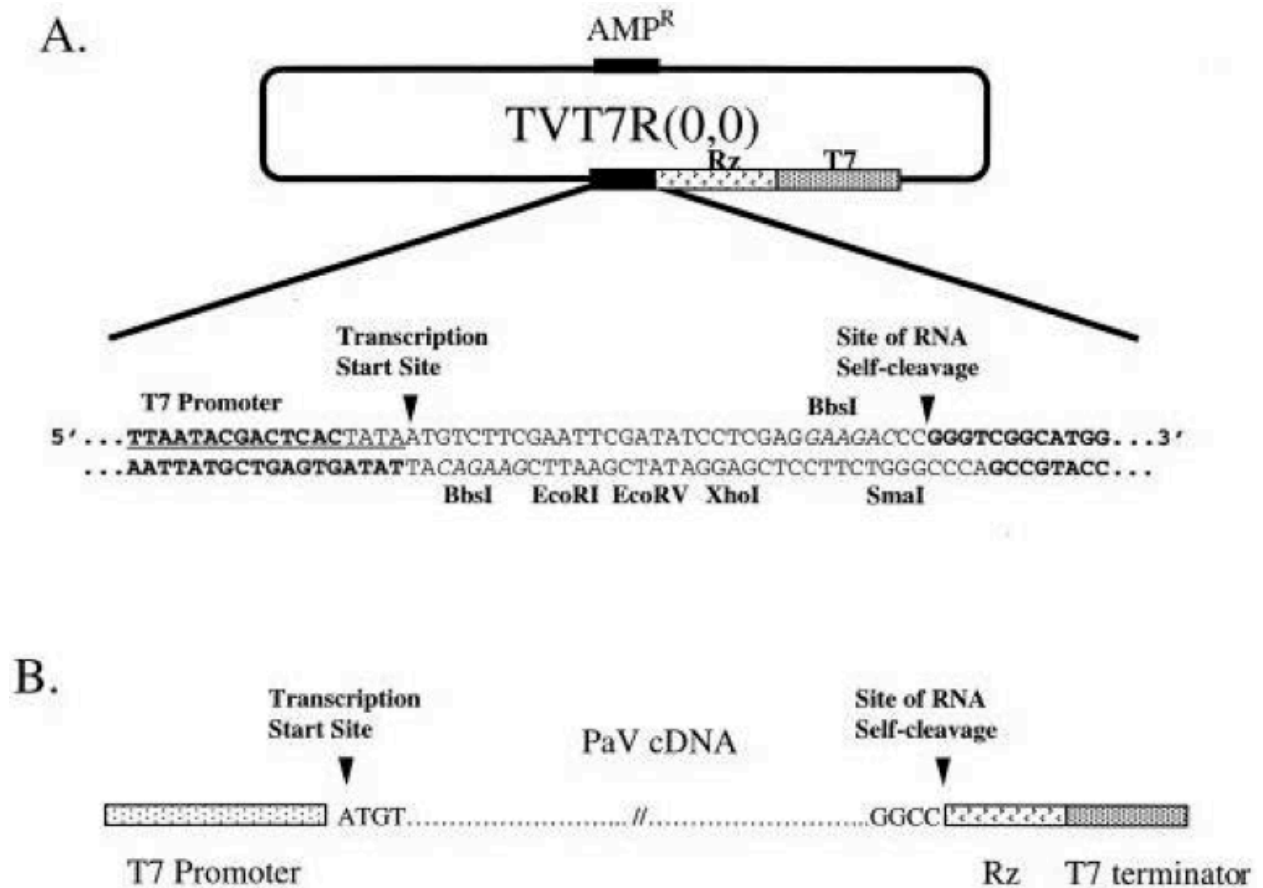


Figure 8: Schematic of the T7 expression vector TVT7R(0,0). (A) Multiple cloning site (MCS) between the T7 promoter (underlined), transcription start site (arrow), and site of RNA cleavage (arrow). The positions of the HDV antigenomic ribozyme (Rz) and T7 terminator are shown on the plasmid map. (B) Highlighting the position of PaV cDNAs in the context of the transcription plasmid TVT7R(0,0). NoV cDNAs were also ligated into the MCS of this plasmid (129). Adapted from Johnson *et al* 2000 (126).

(**Figure 8A**). This resulted in generating pNoV1(0,0) [NoV RNA1], pNoV2(0,0) [NoV RNA2], pPaV1(0,0) [PaV RNA1], and pPaV2(0,0) [PaV RNA2]..

The development of a BHK21 cell line that stably expresses bacteriophage T7 RNA polymerase, BSR T7/5 (**Figure 9** and reference (39)), was pivotal in allowing expression of nodaviral cDNA from T7 expression vectors without the need of a vaccinia helper virus, i.e. in uninfected cells (39). When these cells are transfected with DNA containing a T7 promoter and cDNA copies of a nodavirus genome (i.e. TVT7R(0,0)), a full replicative cycle is initiated with robust RNA synthesis, protein expression and particle production. Albarino *et al.* (2001) pioneered the use of this cell system to study FHV RNA dimeric negative-strand RNA replication intermediates and their template properties (6). BSR-T7/5 cells continue to serve as a powerful mammalian cell model for NoV research and have the potential for elucidating mechanisms for many other viruses (7, 68, 69, 84, 124, 125, 127, 129, 130).

Although plant virus RNA replication studies in budding yeast were underway (121), the nodaviruses (FHV) were the first animal viruses shown to fully replicate their genomes and produce infectious particles in the budding yeast, *Saccharomyces cerevisiae*, adding even more utility to virus research allowing for the characterization of virus-interacting host proteins (199). Price *et al.* (1996) transformed *S. cerevisiae* spheroplasts with the FHV genomic RNAs and found that these cells fully supported FHV RNA replication, produced infectious particles, and replicated a *URA3* yeast selectable marker in the context of FHV RNA2 (199). The cells supporting RdRp-catalyzed heterologous replication of the RNA2-*URA3* RNA maintained a *URA*⁺ phenotype and produced RNA replication-dependent colonies.

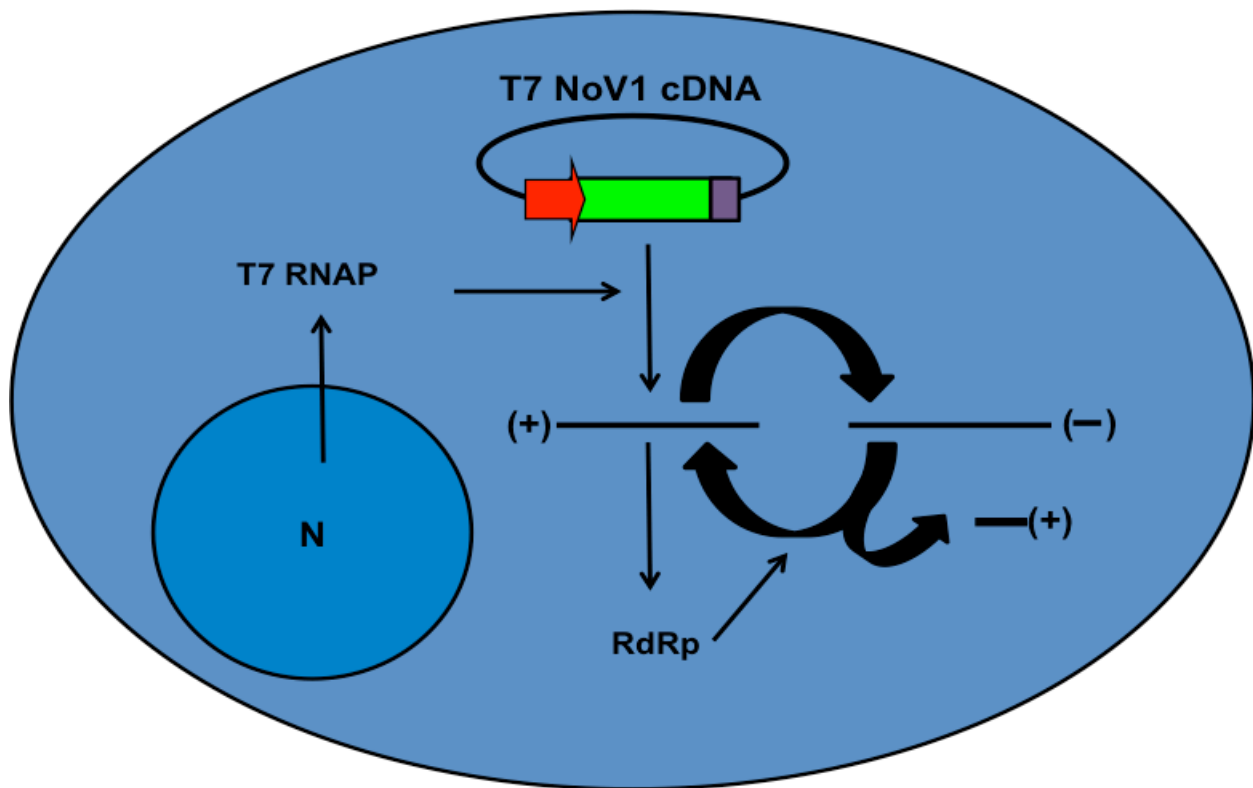


Figure 9: Schematic of the BSR-T7/5 cell culture system. BSR-T7/5 cells, which are derivatives of BHK-21[C-13] cells, are genetically engineered to stably express bacteriophage T7 RNA polymerase in their cytoplasm under G-418 selective pressure (39). This cell line permits cytoplasmic synthesis of primary transcripts from T7 promoter-containing plasmids, which closely recapitulates a natural NoV infection or transfection of *in vitro*-synthesized transcripts. Full-length NoV1 cDNA transcribed from the T7VT7R expression vector will have authentic ends generated by promoter positioning and 3'-Rz cleavage as shown in Figure 8. Primary RNA1 transcripts are translated to produce the RdRp, initiating a viral RNA replication cycle in the cells as described. (124).

NoV also replicates to high levels and produces infectious particles in *S. cerevisiae* after transfection with purified virion RNA or plasmids expressing NoV RNA1 and RNA2 cDNAs from plasmids YEplac112 (91) and Yep351 (114), respectively (202). In addition to supporting NoV RNA replication, yeast cells can heterologously express the *URA3* or *HIS3* selectable markers and GFP from RNA2-based replicons when co-transformed with the NoV RNA1 cDNA clone (202). The introduction of these yeast metabolic genes into RNA2 allowed replication-dependent colony formation. Full-length NoV RNA1 was transcribed from the strong inducible yeast *polIII* promoter, *GAL1*, using plasmid pN1 (202). Primary transcription from this plasmid is induced by galactose in the growth media and is shut off conversely by transferring the cells to a galactose-free growth media (**Figure 10**) (202). The inducible expression of NoV RNAs in the BY4733 yeast strain (*MATa his3Δ200 leu2Δ0 met15Δ0 trp1Δ63 ura3Δ0*) (33) results in a powerful and controllable unicellular system to study the nodavirus life cycle with relative ease (201, 202, 212).

Positive-strand RNA virus replication occurs in the cytoplasm after synthesis of the RdRp. RNA replication for many studied positive-strand RNA viruses occurs in close association with intracellular membranes, which are the sites of viral RCs. The following section will consider these sites and how they are utilized by positive-strand RNA viruses to set up discrete locations to amplify their genomes, protected from cellular defense mechanisms.

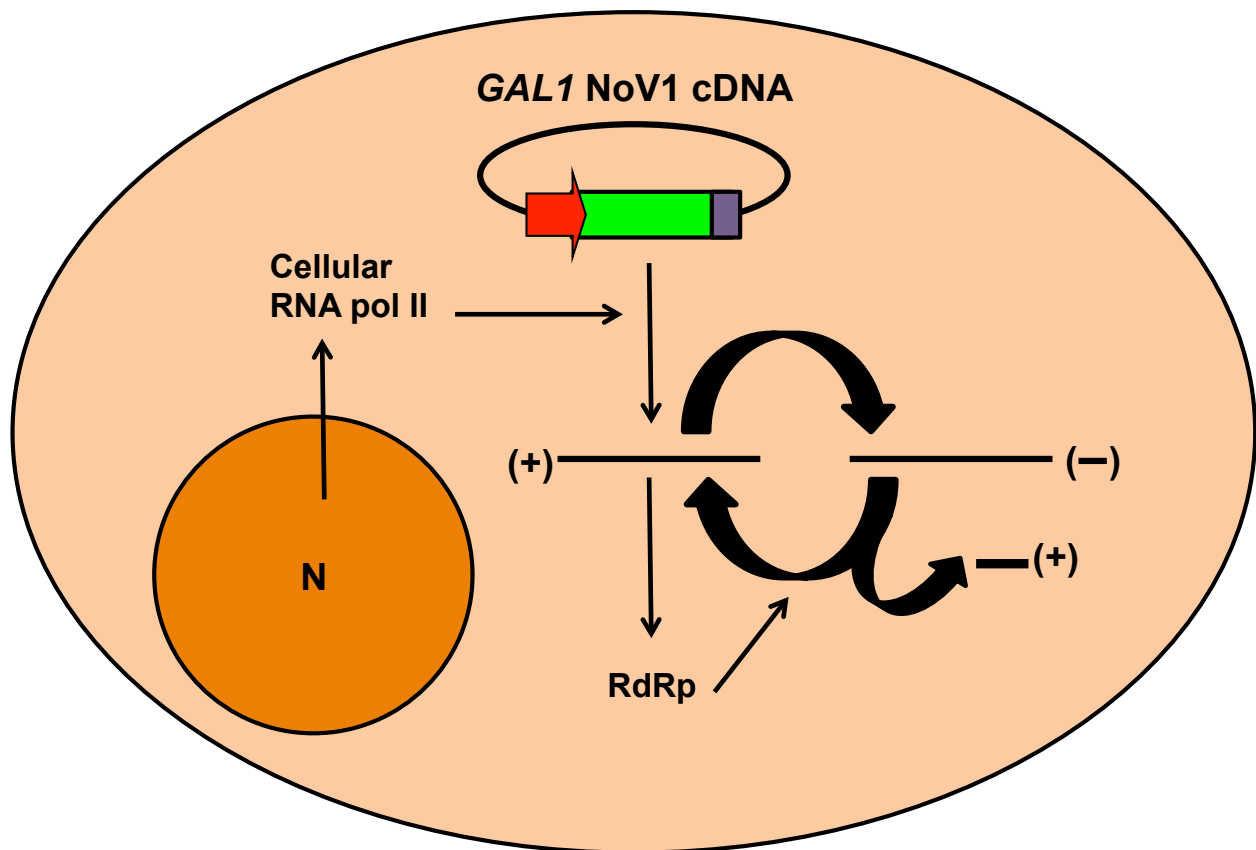


Figure 10: Induction of DNA-launched NoV RNA replication in plasmid-transformed yeast cells. Primary transcription from TpG-NoV1 is under control of the yeast inducible *GAL1* promoter and catalyzed by cellular RNA polymerase II. Transcription is induced by growing cells in media containing galactose. Complete viral replication can be initiated from the transcripts, which have authentic 5' and 3' termini as a result of promoter placement and the self-cleaving HDV ribozyme as described in the legend to **Figures 8 and 9** (202).

1.7 Replication Complex (RC) Formation

Cellular membranes play a significant role in the life cycle of many of the positive-strand RNA viruses studied to date by assisting in viral assembly, progeny release and genome replication (23, 184). Once translated, the viral RdRp binds to the viral genomic RNA(s) and initiates synthesis of full-length negative-strand replication intermediates, which are then used to amplify positive-strand genomic RNAs to high levels (**Figure 11**). Generally, the negative-strand replication intermediates for nodaviruses accumulate to 1-5% of the total levels of positive-strand RNA in cells (16). The negative-strand replication intermediates experimentally serve as a marker for RdRp activity as measured by Northern blot hybridization. The process of RNA replication depicted in **figure 11** generally happens within discrete RC sites.

Numerous ultrastructural studies of animal and plant cells infected by various positive-strand RNA viruses revealed that viral RdRps and RNA replication are associated with networks of rearranged intracellular membranes, which include membrane-bound vesicles and invaginations at the surface of organelles (**Figure 12**) (24, 25, 78, 101, 214). These membrane structures were originally thought to have been virus-induced (i.e., the result of *de novo* membrane synthesis induced by a viral infection), but it was subsequently shown for poliovirus that these vesicles represent ER-derived cellular transport vesicles that were prevented from reaching the Golgi apparatus and subverted by *poliovirus* nonstructural proteins, facilitating subsequent RC formation (224). Viral RNA, the replicase and other viral nonstructural proteins, and (generally) host proteins can be found within these RCs for most positive-strand RNA viruses studied (61). RCs for several positive-strand RNA viruses have been shown to

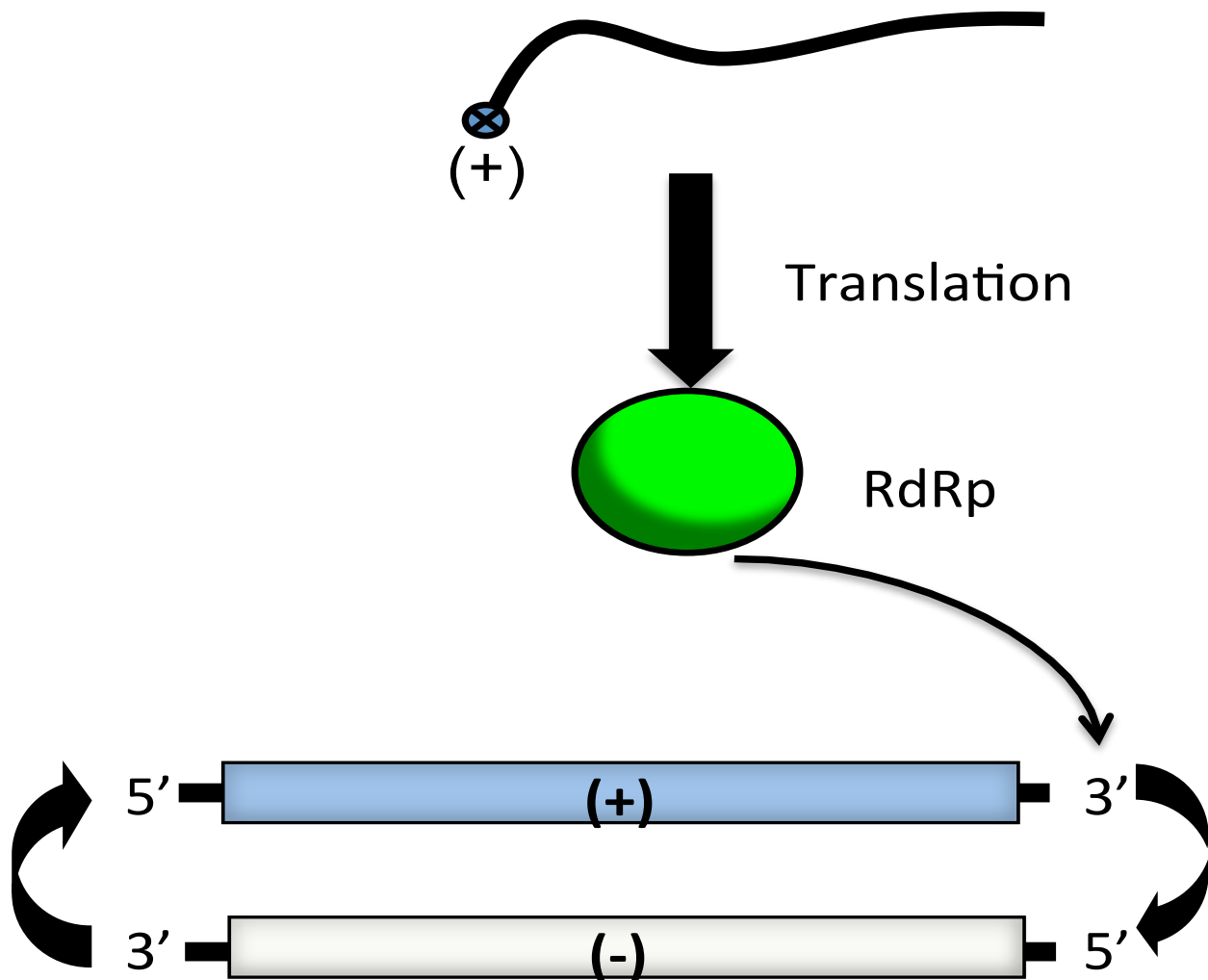
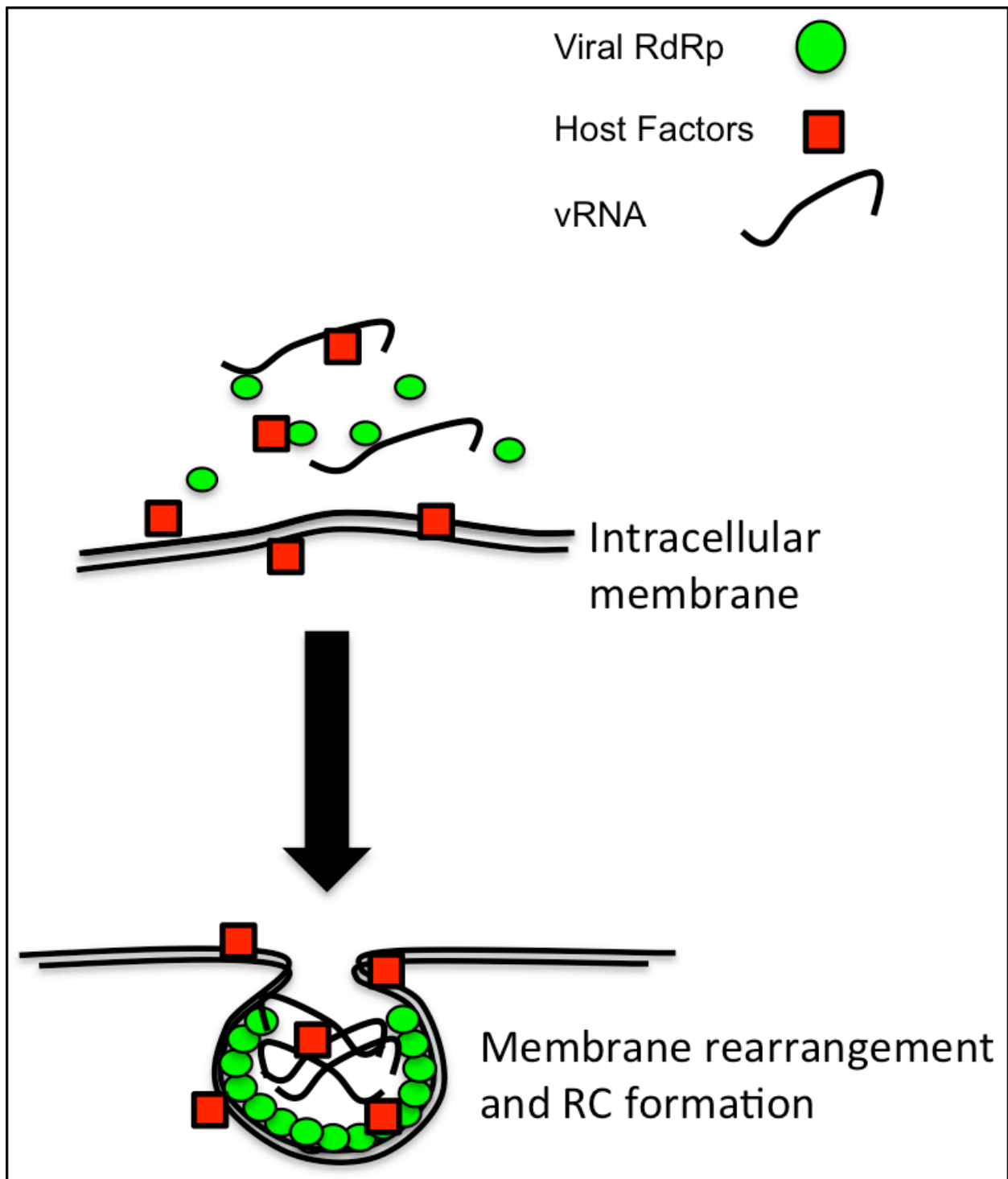


Figure 11: Viral RNA-dependent RNA polymerase (RdRp) activities. Upon translation, viral RdRps catalyze synthesis of a complementary-strand copy of the genomic strand, shown here for a positive strand RNA genome. The complementary replication intermediate is used to make copious amounts of genomic positive strands to be used for translation, packaging and further RNA replication. This activity is essential for infectivity.

form on various modified intracellular membranes including the endoplasmic reticulum (ER; *Poliovirus* and *Brome mosaic virus*), cytoplasmic ER-derived convoluted membranes (*Dengue virus*), lysosomes or late endosomes (*Rubella virus*), multi-vesicular bodies within peroxisomes (*Tomato bushy stunt virus*), and mitochondria (tombus- and nodaviruses) (25, 41, 84, 141, 142, 158, 159, 224, 230). The exact functional role of membranes in RNA replication is not fully understood. It has been proposed that their role is to shield RNA replication and viral RNA from cellular defense mechanisms such as proteases, RNases, RNA interference (RNAi), and recognition of double-stranded viral RNA by toll-like receptor 3 (TLR3) and subsequent production of type I interferons (60, 131, 184). Another proposed role is to sequester RNA templates and replicase proteins in a generalized area within the cell to increase the local concentrations of molecules required for genome replication (60, 131).

The existence or localization of RCs for nodavirus remained unclear until 2001. Prior to that, Garzon and Charpentier (1991) performed ultrastructural analysis of NoV-infected muscle tissues and showed aggregation of mitochondria that exhibit structural rearrangement of the outer membrane (**Figure 2**, inset, structures labeled “v”) and noted that these altered mitochondria were in close association with NoV particles (88). However, the significance of this finding for the NoV life cycle remained unclear until the studies described in this dissertation (**Chapter 2**). Miller *et al.* (2001) showed FA to be a transmembrane protein that localized to mitochondria and induced formation of spherules at the outer mitochondrial membrane in FHV-infected *Drosophila* cells and transformed yeast, which are the sites of FA-catalyzed RNA synthesis (**Figure 13**) (167, 168). FA is the only protein in FHV infection required to selectively induce accumulation

Figure 12: RNA RC formation by positive-strand RNA viruses. Positive-strand RNA virus genome replication occurs in replication complexes (**RCs**) in association with intracellular membranes. RCs are comprised of viral replicase proteins, viral genomic RNA, and cellular factors. The source of intracellular membranes used for RC formation varies with each virus, but typical membrane sources include endoplasmic reticulum, peroxisomes, ER-derived endosomal, and mitochondrial. Alphanodaviruses require RCs to remain membrane-associated for full activity. Upon RC formation, intracellular membrane accumulation and rearrangement can be seen using transmission electron microscopy.



of FHV genomic RNA1 at spherules on mitochondrial membranes in *Drosophila* and yeast cells (142, 244). WhNV was recently shown to interact with mitochondrial membranes and membrane association was required for its RdRp activity (204).

Two members of the betanodaviruses also utilize mitochondrial membranes during infection or transfection of protein A expressing plasmids. GGNNV protein A was predicted to have two N-terminal transmembrane domains (**TMD**) at amino acids 153-173 and 229-249 that facilitate mitochondrial membrane association in cultured sea bass cells (106). AHNV protein A was predicted to have two TMDs at amino acids 1-40 and 225-246 with MTS activity. AHNV protein A localized to mitochondria in infected fish cells and transfected African green monkey kidney COS-7 cells when expressed from a plasmid in the absence of viral RNA replication, but the significance of this localization for the life cycle of the virus is unknown (166).

It is difficult to simply extrapolate the localization of NA from that of FA since the two proteins are markedly different. Although both NA and FA contain canonical RdRp domains, they share only 44% sequence identity at the amino acid level (128). Additionally, the two proteins have different template specificities, with each viral RdRp preferring its own RNA templates (82, 201). Finally, enzymatic activity of NA is more thermostable than that of FA, in that it retains enzymatic activity at temperatures up to 37°C, while FA is inactive at temperatures above 31°C (14). Nevertheless, the literature does suggest a role for mitochondria in the NoV life cycle. Transmission electron micrographs of muscle tissue from NoV-infected mice show localized increases in the number of mitochondria, rearrangement of mitochondrial membranes, and aggregation of mitochondria. Similar rearrangements in muscle tissue are also visible in NoV-

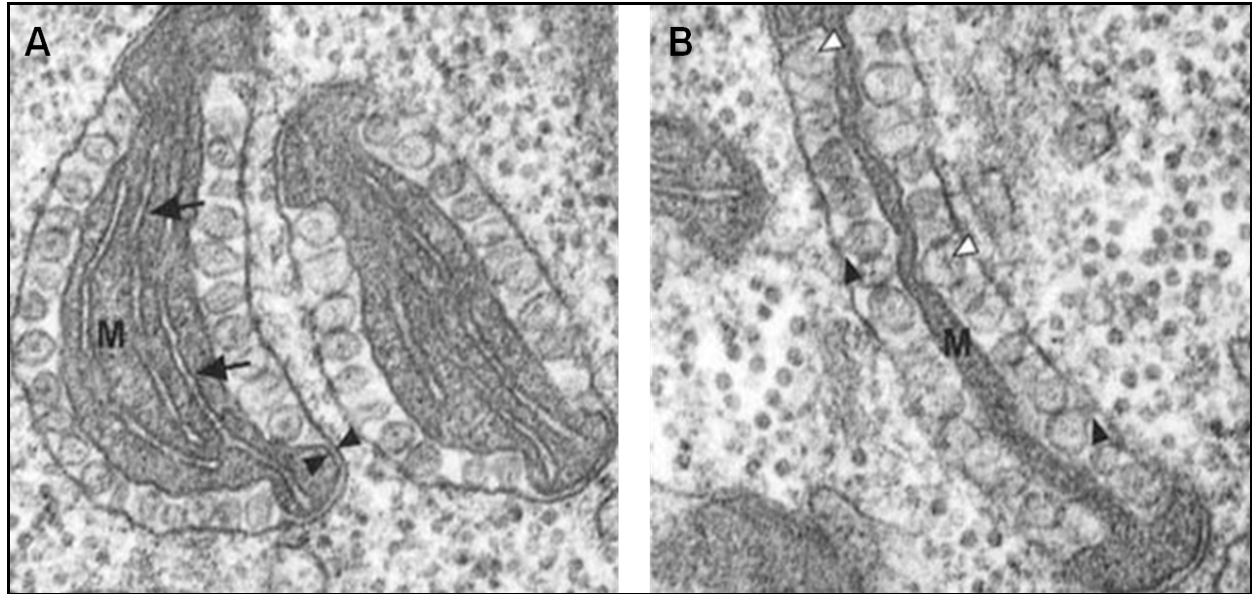


Figure 13: FHV infection induces ultrastructural changes to mitochondria of infected *Drosophila* DL-1 cells. Transmission electron micrographs of FHV-infected *Drosophila* cells at (A) 8 hours post-infection and (B) later during infection highlighting the altered shapes of mitochondria with a condensed matrix (M), inner membranes and cristae (A, arrows) and double membrane structures (A, closed arrowheads). The appearance of virus-induced RC spherules (B, open arrowheads), open to the cytoplasm via bottleneck openings (B, closed arrowheads), can be seen on the outer mitochondrial membrane (167). Similar structures were observed in plasmid-transformed yeast cells (168). Adapted from Miller *et al*, 2001 (167).

infected larvae of the greater wax moth, *Galleria mellonella*, which exhibit hind-segment paralysis on infection with NoV (86-88).

In pursuit of characterizing the formation of RNA RC formation for NoV we first determined the subcellular localization of NA and NA-catalyzed RNA synthesis. In **Chapter 2** we provide evidence that NoV establishes RNA RCs on the OMM, and NA is an integral membrane protein that localizes to clustered mitochondria in cultured mammalian cells (84). The cells in this study repeatedly displayed a mitochondrial morphology that is reminiscent to the clustered morphology observed in studies that focused on disrupted mitochondrial morphology control mechanisms (134, 239). To further understand how NoV RNA RC formation occurs and the role mitochondrial morphology plays in this process, we studied how NA interacts with the controllers of mitochondrial division (**fission**). **Chapter 3** considers a possible mechanism by which NoV RC formation occurs on clustered mitochondria via inhibition or subversion of the vital mitochondrial fission process mediated by dynamin related protein 1 (**Drp1**). The implications of the results from these two studies are discussed in **Chapter 4**.

Chapter 2: Subcellular Localization of the NoV RdRp in Mammalian Cells

2.1 Introduction

Positive-strand RNA viruses replicate their genomes in RCs associated with intracellular membranes, often via interactions between the membranes and one or more viral nonstructural proteins (4, 169, 217). The source of the membranes varies with the virus: many viral RCs are associated with modified membranes derived from the ER, including members of the arteri-, bromo-, corona-, flavi-, and picornavirus families (22, 25-28, 223, 224, 230, 241, 267). However, the RCs of other virus families localize to membranes derived from other organelles, including chloroplasts and peroxisomes (tombusviruses), endosomes and lysosomes (togaviruses), and mitochondria (tombus- and nodaviruses) (63, 159, 167, 213, 215). For the nodaviruses, RNA replication complexes lose activity when solubilized from membranes and therefore, this membrane association may also play a functional role in RNA replication, for example by crowding the RdRp and RNA together to enhance replication (103, 284, 285). Little is known about the mechanism of replication complex formation in cells infected with NoV. Nevertheless, the literature does suggest a role for mitochondria in the NoV life cycle. As mentioned in **Chapter 1**, NoV-infected muscle cells exhibit mitochondrial aggregation and membrane rearrangement, leading to disorganization of the muscle fibrils on the tissue level and ultimately in hind limb/segment paralysis. However, the molecular basis for this pathogenesis and the role of mitochondria in NoV infection was unclear for 24 years.

In this study, we tested the hypothesis that NoV establishes RNA RCs that associate with mitochondria in mammalian cells. We reported that NA contains two

predicted membrane-associated regions (**MARs**). Our results demonstrate that NA localized to mitochondria and caused them to cluster in cultured mammalian cells. Deletion of the predicted MARs from NA resulted in loss of mitochondrial localization, abolition of mitochondrial clustering, and reductions in NA protein levels and of NoV RNA1 replication products. The results of selective membrane permeabilization and confocal microscopy experiments show that NA was targeted to the OMM, where it remained exposed to the cytoplasm. We also demonstrated using biochemical assays that NA was closely associated with intracellular membranes. These results firmly established the role of mitochondria and mitochondrial membranes in NoV RNA replication in mammalian cells and form the basis for further studies on the mechanism of NoV RC formation.

2.2 Materials and Methods

Cells, virus stocks and tissue culture. All recombinant plasmids were amplified in *Escherichia coli* strain NEB10b (New England Biolabs) grown in 2X YT broth or on 2X YT-agar plates supplemented with ampicillin (10). BSR-T7/5 cells were grown at 37°C in Glasgow MEM or DMEM (GIBCO) supplemented with 1 mg/ml G-418 (Life Technologies), 5% each newborn calf serum and fetal bovine serum (39). The full-length RNA1 cDNA clone of NoV was derived from the Mag-115 strain, as described previously (124). Its GenBank ID is AF174533.

BSR-T7/5 cells were seeded in 6-well plates (10 cm² wells) at a density of 5 x 10⁵ cells/well; for immunofluorescence microscopy, the cells were plated over sterilized glass coverslips. Cells were transfected with 2 µg of the appropriate pNoV1(0,0)-based

plasmid using Lipofectamine 2000 and serum-free Opti-MEM (Invitrogen, Carlsbad, CA), as described (124). Cells were incubated with DNA-liposome complexes for 4 h at 37°C, supplemented with complete growth media and the incubation was continued for 20 h prior to harvest. For the proteasome inhibition assays, transfected cells were treated with the cell-permeable proteasome inhibitor MG132 (262) at a concentration of 5 mM for the 8 h prior to harvest, beginning at 16 hours post-transfection (**hpt**).

***In silico* predictions and sequence alignments.** Computer protein topology predictions were performed on the primary sequence of the NoV RdRp ORF using the following prediction programs: TopPred II (51); PSIPRED (38, 165); and SOSUI (115). Hydrophobicity was calculated by TopPred II using the method of Kyte and Doolittle (144) with a core window size of 11 aa and a full window size of 21 aa. We computed the identity between the NoV and GGNNV RdRp primary sequences using the ClustalW2 multiple sequence alignment program (146).

Plasmid constructions. Expression of NoV RNA1 and the viral RdRp in mammalian cells is directed by plasmid pNoV1(0,0), in which the full-length NoV RNA1 cDNA (Accession # NC_002690.1) is under transcriptional control of a bacteriophage T7 promoter (124). The predicted MARs were deleted from the RdRp ORF in pNoV1(0,0), either singly (Δ 12-34 and Δ 42-64) or together (Δ 12-64) by circular PCR-based mutagenesis with the overlapping oligonucleotide primers shown in **Table 3**, followed by *DpnI* selection, as described (218). These deletions were confirmed by DNA sequencing and, in each case, a small fragment containing the deletion was introduced back into parental pNoV1(0,0) with *SapI* and *MluI* restriction enzymes, resulting in plasmids pT7-N1 Δ 12-34, pT7-N1 Δ 42-64, and pT7-N1 Δ 12-64. To facilitate

immunodetection of wild type and mutant forms of the NoV RdRp, we inserted an in-frame C-terminal influenza virus hemagglutinin (**HA**) epitope tag between the last amino acid of the RdRp and its stop codon using circular PCR-based mutagenesis with overlapping oligonucleotide primers (**Table 3**) followed by *DpnI* selection, as described (218). The insertion was confirmed by DNA sequencing and a small DNA fragment containing the insertion was cloned back into WT and mutant versions of pNoV1(0,0), resulting in plasmids pT7-N1-HA, pT7-N1Δ12-34-HA, pT7-N1Δ42-64-HA, and pT7-N1Δ12-64-HA.

Immunofluorescence confocal microscopy. BSR-T7/5 cells were mock transfected or transfected with plasmids as described above. In some experiments (where indicated in the text), MitoTracker[®] Red CM-H₂XRos (**MTR**; Life Technologies) was used as a vital dye to stain the mitochondria of living cells prior to immunofluorescence (500 nM MTR in serum-free Opti-MEM for 1 hour at 37°C), as described (167). After MTR treatment, cells were fixed, permeabilized in 100% methanol, and blocked at room temperature in phosphate-buffered saline (**PBS**) supplemented with 1% bovine serum albumin, 1% nonfat milk, 0.1% sodium azide, and 0.1% Tween 20. For the selective membrane permeabilization assays, cells were fixed with 4% paraformaldehyde in PBS at 4°C overnight and permeabilized at room temperature for 10 min with either 0.002% (wt/vol) saponin (Sigma-Aldrich) or 0.002% saponin and 0.2% Triton X-100 (**TX100**; Fisher Scientific) as previously described (167). After permeabilization, cells were blocked and washed with PBS lacking Tween-20.

Immunofluorescence was performed as described (167) with the following modifications. Antigens were detected within blocked BSR-T7/5 cells with primary

antibodies specific for the hemagglutinin epitope tag (HA; mouse monoclonal IgG₃; Santa Cruz Biotechnology), newly-synthesized viral RNA (BrU; mouse monoclonal IgG₁; Sigma-Aldrich), the outer mitochondrial membrane marker monoamine oxidase (**MAO**; rabbit polyclonal IgG; Santa Cruz Biotechnology), or the inner mitochondrial membrane marker cytochrome c oxidase subunit III (**COX3**; goat polyclonal IgG; Santa Cruz Biotechnology). Binding of primary antibodies to their respective antigens was detected with the following fluorescently labeled secondary antibodies (Santa Cruz Biotechnology): fluorescein isothiocyanate (**FITC**)-labeled goat anti-mouse to detect either HA or BrU, Texas Red (**TR**)-labeled goat anti-rabbit to detect MAO, or TR-labeled rabbit anti-goat to detect COX3.

To minimize photo-bleaching effects, all staining steps were performed in the dark. Cell nuclei were counterstained with 4',6-diamidino-2-phenylindole (**DAPI**; Life Technologies). Coverslips were mounted with fluorescence mounting media (Dako) and sealed to prevent drying and fluorescence fading. High-resolution digital fluorescent images were captured using a Zeiss LSM 700 confocal microscope equipped with a 63X immersion oil objective and ZEN 2009 software (Zeiss, New York, NY) for acquisition and processing of confocal images. Single-plane images were sequentially scanned using a one Airy unit pinhole setting for each channel and acquired at a 1024 x 1024 pixel resolution. The same software was used to visualize co-localization of the red and green signals and to export the images as TIF files. Adobe Photoshop software was used to crop, rotate, and resize panels where needed to ensure the images were all the same size and scale, using the scale bars embedded in each image as a guide.

ZEN 2009 software was also used to evaluate the grade of co-localization between two fluorescently labeled intracellular targets. Regions of interest (**ROIs**) were demarcated manually within captured images to reduce background contribution. The degree of co-localization of two selected signals was determined as described (160), using a squared Manders' overlap coefficient (**OC**) of dual-color images (specifically the green and red emission fluorescence signals), executed on a pixel-by-pixel basis. OC values are expressed as the percentage of overlap between red pixels (MTR or TR) and green pixels (FITC) and are shown in **Table 4**. An OC of zero indicates a lack of overlap between pixels of two defined signals within the selected ROI, whereas a value of 1 represents perfectly co-localized signals of all pixels in a selected ROI (160).

Cell fractionation and differential centrifugation. Cells were harvested by scraping and crude subcellular fractions were prepared as previously described (96-98, 284), with the following minor modifications. Transfected BSR-T7/5 cells were washed twice with ice-cold PBS, harvested by scraping into PBS, and collected by centrifugation. Cell pellets were gently resuspended in hypotonic lysis buffer (1 mM Tris-HCl, pH 7.4; 0.1 mM EDTA; 15 mM NaCl) (106) supplemented with 1 mM each benzamidine (Sigma-Aldrich) and phenylmethylsulfonyl fluoride (**PMSF**; Sigma-Aldrich). Cells were homogenized with a glass Dounce and unbroken cells, large cell debris and nuclei were removed by centrifugation. The resulting post-nuclear lysate (**PNL**) was centrifuged at 20,000 x *g* for 30 min to pellet intracellular membranes. The supernatant was carefully removed and centrifuged at 100,000 x *g* for 1 hour to pellet microsomal membranes and the supernatant was carefully collected as the cytosolic fraction. All centrifugation steps were performed at 4°C. Membrane pellets were resuspended in 2X

Table 3: Oligonucleotide primers used for circular PCR-based mutagenesis.

Sequence Name	Sequence (5'-to-3')
DMAR1plus	CGAGACAATCATCAACGGCGCAGTCGCGGGGTCCTGCGTG GTG
DMAR1minus	CACCACGCAGGACCCCGCGACTGCGCCGTTGATGATTGTCT CG
DMAR2plus	GTCGCGGGGTCCTGCGTGGTGCAGCACCGTCTGCCGATGG CC
DMAR2minus	GGCCATCGGCAGACGGTGCTGCACCACGCAGGACCCCGCG AC
DMAR1+2plus	CGAGACAATCATCAACGGCGCACAGCACCGTCTGCCGATG GCC
DMAR1+2minus	GGCCATCGGCAGACGGTGCTGTGCGCCGTTGATGATTGTCT CG
NA-HA-QCplus	CCCAGCTGGGTGCGGTGGGCGTGGTAAAGGCTACCCATAC GACGTGCCAGACTACGCCTGAGTGATTCATCGTCCCATCTG ACGAAACCC
NA-HA-QCminus	GGGTTTCGTCAGATGGGACGATGAATCACTCAGGCGTAGTC TGGCACGTCGTATGGGTAGCCTTTACCACGCCCACGCGACC CAGCTGGG

Table 4: Overlap coefficients calculated for confocal microscopy experiments shown in Figures 16, 17, 19 and 22.

CONFOCAL MICROGRAPH BY EXPERIMENT	OVERLAP COEFFICIENT (OC)*
Time Course (Figure 16)	
4 hpt	0
8 hpt	88 ± 2.6
12 hpt	86 ± 3.3
16 hpt	89 ± 2.9
20 hpt	82 ± 6.1
24 hpt	83 ± 3.1
Selective Permeabilization (Figure 17)	
Saponin Alone, MAO, Merge	82 ± 2.1
Saponin Alone, COX3, Merge	0
Saponin + Triton X-100, COX3, Merge	88 ± 2.9
MAR Deletion Mutants (Figure 19)	
WT, Merge	86 ± 2.3
Δ12-34, Merge	88 ± 12.4
Δ42-64, Merge	85 ± 5.7
Δ12-64, Merge	47 ± 4.2
BrU Labeling (Figure 22)	
Mock, Merge	0
WT, Merge	94 ± 1.5
Δ12-64, Merge	0

*OC is defined as the percentage overlap between red (MTR or TR) and green (FITC) pixels ± standard deviation, as described in this chapter's Materials and Methods section (2.2) and in reference (160).

Laemmli sample buffer, resolved by SDS-polyacrylamide gel electrophoresis (**PAGE**), and analyzed by Western blotting as described below.

Membrane flotation and membrane disassociation assays. The 20,000 x g pellet from transfected BSR-T7/5 cells was extracted as described above and resuspended in TED buffer (50 mM Tris-HCl, pH 8.0; 10 mM NaCl; 1 mM EDTA; 1 mM dithiothreitol [DTT] and 5% glycerol) (219, 284), supplemented with 1 mM each benzamidine and PMSF. Nycodenz was added to membrane suspensions to a final concentration of 37.5% (wt/vol). Membrane suspensions were loaded under 5 to 35% (wt/vol) discontinuous Nycodenz gradients as previously described (168) and centrifuged to equilibrium in a swinging-bucket rotor at 100,000 x g for 20 h. After centrifugation ten 500ml fractions were collected; in this case, the five fractions from the top of each gradient were designated as the low-density (**LD**) fractions, while the bottom five fractions were designated as the high-density (**HD**) fractions. Samples were mixed with 2X Laemmli sample buffer and proteins were resolved by SDS-PAGE and analyzed by Western blotting.

Membrane disassociation assays were performed as previously described (80, 168, 186), with the following minor modifications. The 20,000 x g membrane pellets from transfected BSR-T7/5 cells were collected as described above and resuspended in either 1 M NaCl, 100 mM sodium carbonate (Na_2CO_3 ; pH 11.0), or 1 M NaCl with 1.5% TX100 and incubated on ice for 30 min. Nycodenz was added to the treated membrane suspensions to 37.5% and the samples were centrifuged on discontinuous Nycodenz gradients as described above. After centrifugation we collected ten 500 ml fractions as described above. In this case, the five LD fractions were pooled, as were the five HD

fractions. Equal volume samples from each pooled fraction were mixed with 2X Laemmli sample buffer, resolved by SDS-PAGE, and analyzed by Western blotting.

SDS-PAGE and Western blot analysis. All samples were prepared and resolved by SDS-PAGE as previously described (145). Transferred proteins were subjected to immunodetection with mouse anti-HA monoclonal or rabbit anti-MAO A/B polyclonal antibodies followed by incubation with goat anti-mouse or goat anti-rabbit polyclonal antibodies (Santa Cruz Biotechnology) conjugated to either horseradish peroxidase (**HRP**) or alkaline phosphatase (**AP**). Blots were developed using either AmershamTM ECLTM Prime Western blot Detection Reagent (GE Healthcare Life Sciences) for HRP-conjugated secondary antibodies or Immun-StarTM AP substrate (Bio-Rad) for AP-conjugated secondary antibodies and exposed to x-ray film. Developed films were photographed with a Gel Doc XR Molecular Imager running Quantity One 1-D Analysis Software (Bio-Rad) to generate the digital images shown.

Visualization of RNA replication complexes. Newly synthesized NoV viral RNA was labeled in transfected BSR-T7/5 cells by liposome-mediated introduction of 5-bromouridine 5'-triphosphate (**BrUTP**; Sigma-Aldrich) as previously described (111, 266, 269), but with the following modifications. At 19.5 hpt cellular transcription was inhibited by a 30 min pre-treatment with 20 µg/ml actinomycin D-mannitol (**act D**; Sigma-Aldrich). Lipofectamine 2000 was mixed with serum-free Opti-MEM containing 10 mM BrUTP, incubated at room temperature to allow BrUTP-containing liposomes to form. The BrUTP-liposome complexes were diluted in Opti-MEM with 1% fetal bovine serum and 20 µg/ml act D, applied to the cells, and incubated for 4 h (20-24 hpt). At 24

hpt, cellular mitochondria were stained with MTR for 1 hour, fixed in 100% methanol, and processed for immunostaining and confocal microscopy as described above.

RNA isolation and Northern blot hybridization analysis. Total cellular RNA was isolated from transfected BSR-T7/5 cells using an RNeasy Mini Kit (Qiagen) as described (6). RNA samples (0.5 µg for detection of positive strands or 2 µg for detection of negative strands) were separated on denaturing formaldehyde-agarose gels, stained with ethidium bromide (**EtBr**), and transferred to charged nylon membranes as previously described (212). Northern blot hybridization was performed as described previously (147, 181), using ³²P-labeled riboprobes specific for the positive or negative strand of NoV RNA3, which also detect RNA1 (124, 202, 212). The blots were visualized with a Personal Molecular Imager (Bio-Rad) and quantitated using Quantity One 1-D Analysis Software (Bio-Rad). Levels of NoV RNA1 and RNA3 replication products were normalized to those of cellular 28S rRNA (visualized by ethidium bromide staining of the gel before transfer) and are presented as a percentage of the WT values. The relative RNA values from three independent experiments are presented as mean values ± standard deviations.

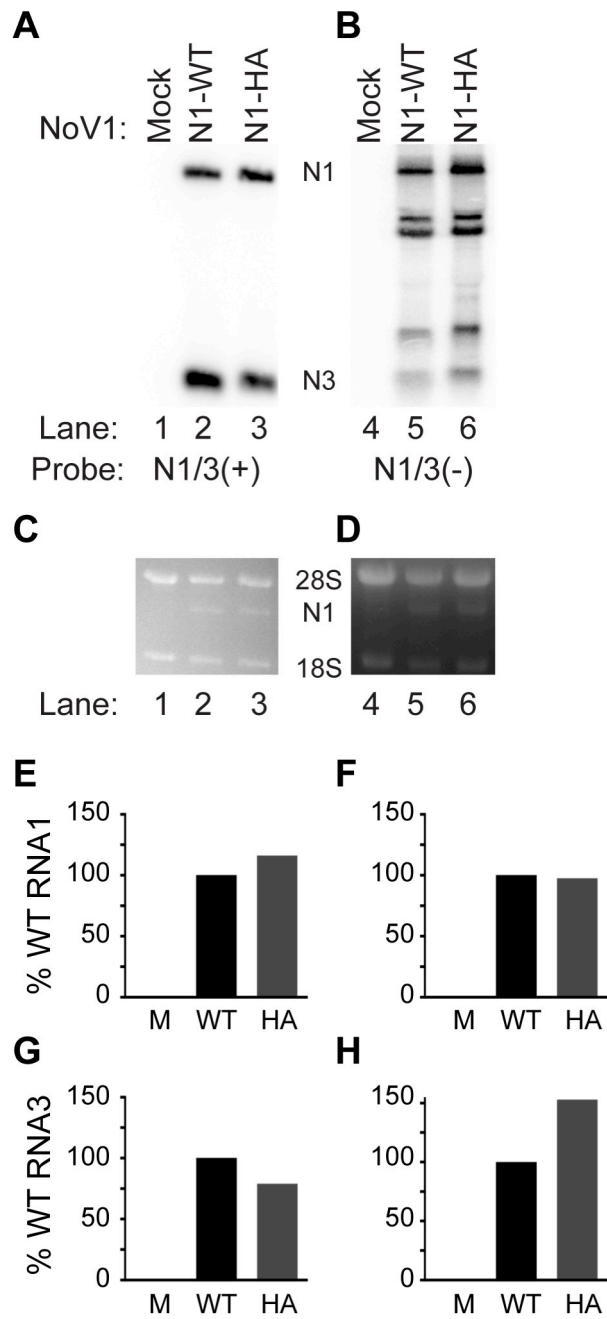
2.3 Results

Expression and localization kinetics of the NoV RdRp in transfected mammalian cells. Previous studies of NoV-infected tissues show close association of NoV viral particles with ultrastructurally malformed mitochondria, implicating this organelle in the NoV infectious cycle (86-88). Additionally, the FHV RdRp associates with mitochondrial membranes in infected *Drosophila* and yeast cells (167, 168). To

determine whether the NoV RdRp localizes to mitochondria in cells, we used a well-defined reverse genetics system in which NoV RNA replication can be initiated in mammalian cells from cloned cDNA copies of the NoV genomic RNAs (124, 125, 202, 212). For example, the entire replicative cycle can be initiated on expression of the NoV RNA1 and RNA2 cDNAs from T7 promoters in plasmid-transfected baby hamster kidney BSR-T7/5 cells (39) that constitutively express cytoplasmic T7 RNA polymerase (124, 125). The replicative cycle launched from this system mirrors the kinetics seen during NoV infection (124).

To facilitate detection of the NoV RdRp, we constructed a version of the full-length NoV RNA1 cDNA in which the RdRp was engineered to contain a 10 amino acid C-terminal influenza virus hemagglutinin (**HA**) epitope tag. To ensure that the HA tag did not hinder the polymerase activity of the RdRp, we transfected BSR-T7/5 cells with plasmids pT7-N1 and pT7-N1-HA, which express WT or HA-tagged versions of the RdRp, respectively. At 24 hpt, we isolated total cellular RNA and analyzed accumulation of viral RNA replication products by Northern blot hybridization using probes specific for the positive or negative strands of RNA1, which also detect subgenomic RNA3. The HA-tagged version of the RdRp synthesized negative strand RNA replication intermediates (**Figure 14B**, lanes 5 and 6) and positive strand RNA replication products (**Figure 14A**, lanes 2 and 3) to levels that matched or exceeded that of the WT (compare the quantitation presented in **Figure 14**, panels E-H). Therefore, we concluded that the tagged RdRp was as functional as the WT in catalyzing viral RNA replication when expressed in transfected BSR-T7/5 cells and that the 30 nucleotide

Figure 14: NoV RNA replication is unaffected by the presence of a C-terminal HA epitope tag. Total cellular RNAs were isolated from BSR-T7/5 cells transfected with either pT7-N1 (**WT**) or tagged pT7-N1-HA, separated on denaturing gels, and subjected to Northern blot hybridization analysis using probes specific for the positive (**A**) or negative (**B**) strands of RNA1, which also detect subgenomic RNA3. Prior to transfer, gels were stained with ethidium bromide to allow visualization of 18S and 28S rRNAs for use as loading controls (**C** and **D**). Quantitation of positive (+) and negative (-) strands of NoV RNA1 (**N1**) and NoV RNA3 (**N3**) relative to WT levels are shown in panels **E-H**: **E**, N1(+); **F**, N1(-); **G**, N3(+); and **H**, N3 (-). The relative RNA values for a single representative experiment are shown.



insertion encoding the tag did not affect the ability of RNA1 to serve as a template for RNA replication (**Figure 14**).

We explored the kinetics of RdRp expression in transfected mammalian cells by Western blot analysis (**Figure 15**) and by indirect immunofluorescence and confocal microscopy (**Figure 16**). Duplicate sets of BSR-T7/5 cells were mock transfected or transfected with pT7-N1-HA and analyzed at four-hour intervals between 4 and 24 hpt. Cell lysates were prepared at each time point as described in this chapter's Materials and Methods section (**2.2**) and HA-tagged RdRp was analyzed by Western blot with a monoclonal antibody directed against the HA epitope tag (**Figure 15**). As shown in **Figure 15**, the RdRp was already detectable at 4 hpt and its levels increased up to 20 hpt, with maximal expression maintained through at least 24 hpt.

The duplicate set of transfected cells was analyzed by confocal microscopy over the same time period. At each time point, mitochondria were stained with MitoTracker[®] Red CM-H₂XRos (**MTR**) and the cells were fixed and permeabilized. The viral RdRp was visualized by immunostaining with anti-HA primary and FITC-labeled secondary antibodies followed by confocal microscopy, as described in this chapter's Materials and Methods section (**2.2**). For each panel, co-localization of the red and green signals was determined using a squared Manders' overlap coefficient (**OC**) of dual-color images, expressed as the percentage of overlap between the red (**MTR**) and green (**FITC**) pixels, as described (160). The OC values calculated for the images shown in **Figure 16** are summarized in **Table 4**.

In untransfected cells (**Figure 16**, panel B, cell in upper right designated by an open arrowhead), MTR treatment consistently resulted in a diffuse cytoplasmic staining

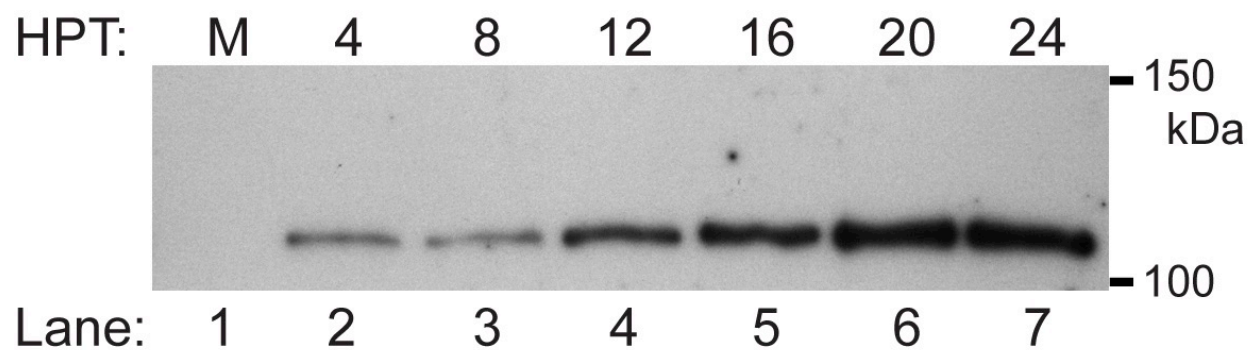


Figure 15: NoV RdRp expression time course analysis. BSR-T7/5 cells were transfected with pT7-N1-HA and PNLs were prepared at 4 h intervals between 4 and 24 hpt. Proteins were resolved on a 7.5% SDS-PAGE gel, proteins transferred, and the HA-tagged RdRp was detected by immunoblotting with anti-HA antibodies. Mock (**M**) transfected PNL was harvest at 24 hpt. Exposed film was imaged using a Gel-Dock XR (Bio-Rad).

pattern characteristic of mitochondria (red signal). A similar pattern was observed at 4 hpt in cells transfected with pT7-N1-HA (**Figure 16**, panel A). In both cases, MTR and FITC were not observed to co-localize, exhibiting an OC value of 0% (**Table 4**). However, in contrast to the untransfected cells, at 8 hpt some of the mitochondria had begun to clump or cluster together (**Figure 16**, panel B, cell in lower left designated by a closed arrowhead). This clustering progressed over time thereafter, such that by 24 hpt all of the visible mitochondria appeared in clustered networks (**Figure 16**, compare panels B-F with panel A). In these same cells, immunofluorescence staining of the NoV RdRp showed the appearance of clustered structures in the cytoplasm that were excluded from the nucleus (**Figure 16**, green signal designated by the closed arrowhead) and localized with MTR (**Figure 16**, panel F, yellow signal designated by the closed arrowhead), with high levels of red (MTR) and green (FITC) pixel overlap detected between 8 and 24 hpt, reaching a maximal OC of nearly 90% at 16 hpt (**Table 4**). Interestingly, the co-localization of the viral RdRp with MTR depended on the presence of actively replicating RNA1, since localization was diminished when the RdRp was expressed from a non-replicating template (**data not shown**). These results suggest that the NoV RdRp localized to mitochondria in transfected mammalian cells, and this interaction induced clustering of mitochondria into networks. Since maximal RdRp expression and mitochondrial clustering were observed at 24 hpt (**Figures 15 and 16**, respectively), we selected this time point for all of the subsequent analyses presented here.

NoV RdRp localizes to the mammalian outer mitochondrial membrane. The localization of NoV RdRp to mitochondria (**Figure 16**) prompted us to determine the

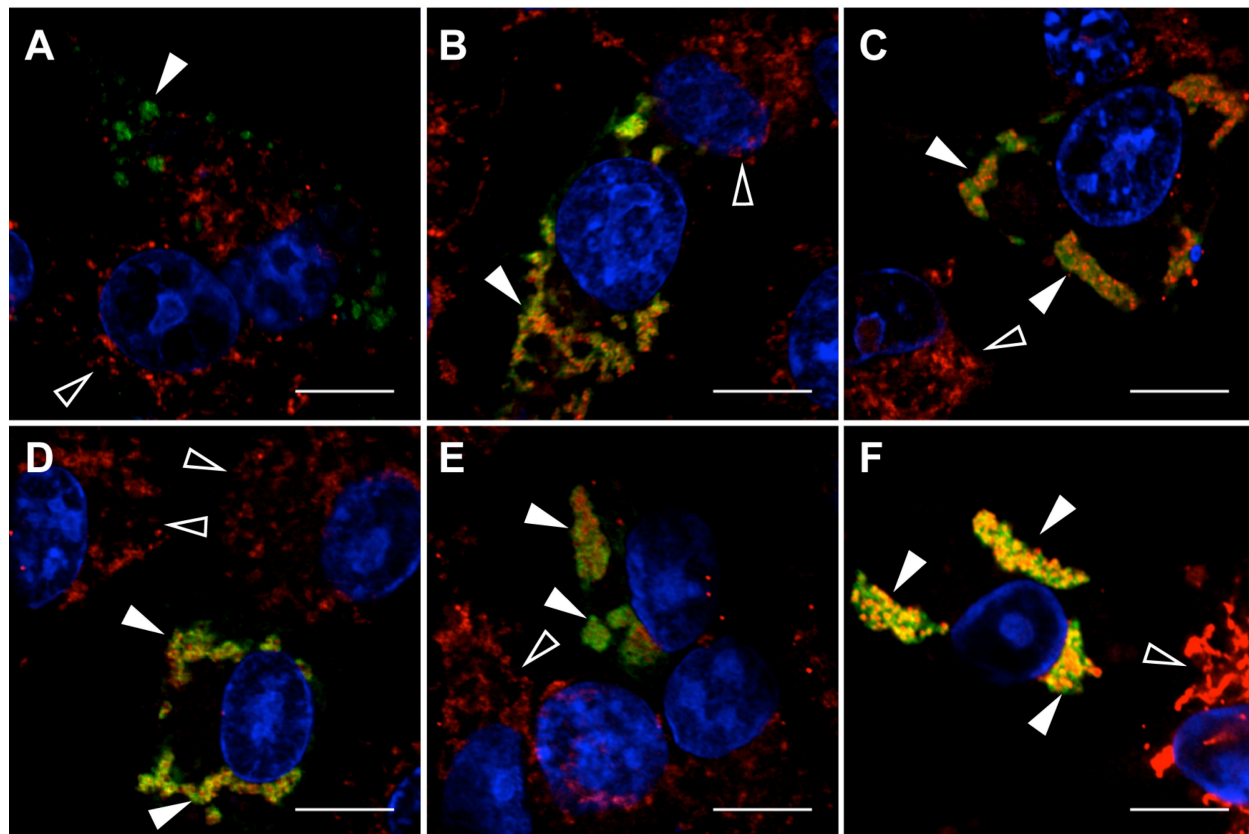


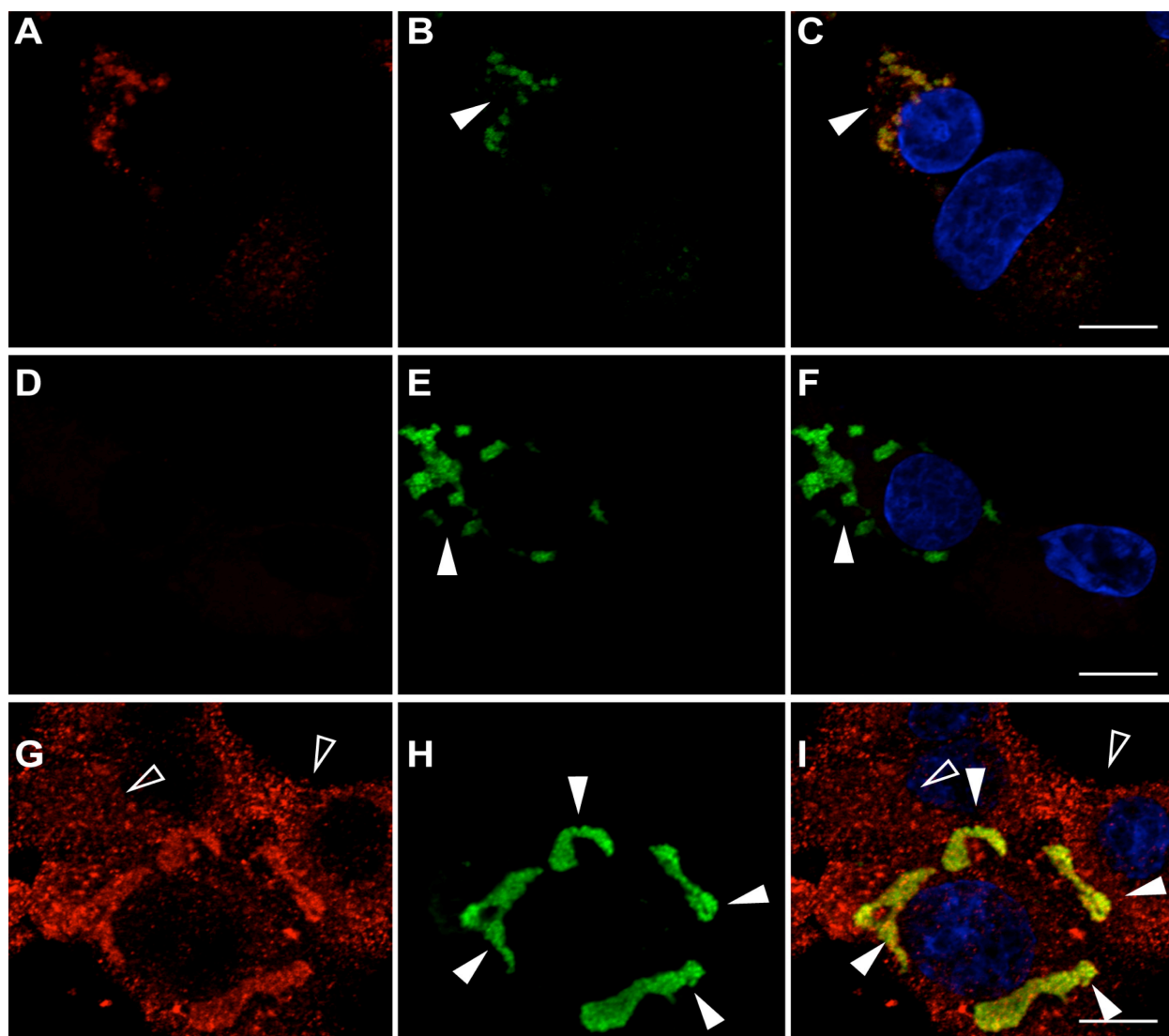
Figure 16: NoV RdRp localization time course analysis. BSR-T7/5 cells were transfected with pT7-N1-HA and incubated as described in the legend to **Figure 14**. At each time point, the RdRp was detected by immunostaining with anti-HA primary and FITC-labeled secondary antibodies (green). Nuclei were visualized by staining with DAPI (blue) and the morphology of mitochondrial networks was visualized by staining with MitoTracker Red CM-H₂XRos (red). Each panel represents a different time point: **A**, 4; **B**, 8; **C**, 12; **D**, 16; **E**, 20; **F**, 24 hpt. Immunofluorescence confocal microscopy images showing merged signals are shown; yellow signal on merge indicates co-localization. Closed arrowheads indicate RdRp expression in transfected cells; open arrowheads indicate untransfected cells. Scale bar = 10 μ M.

specific mitochondrial compartment (outer or inner membrane or matrix) that was involved, using a selective membrane permeabilization procedure. These experiments rely on the affinity of the detergent saponin for cholesterol in membranes. The plasma membrane contains a higher concentration of cholesterol than do mitochondrial membranes (144, 216). Therefore, at the low concentration used in this study, saponin permeabilizes the plasma membrane without compromising the integrity of the mitochondrial membranes. However, when cells are treated with the same concentration of saponin in the presence of Triton X-100 (**TX100**), their mitochondrial membranes become permeabilized as well.

Therefore, BSR-T7/5 cells were transfected with pT7-N1-HA as before and we performed selective membrane permeabilization prior to analysis by immunofluorescence confocal microscopy (**Figure 17**). Following appropriate incubation, the transfected cells were fixed with paraformaldehyde and permeabilized with saponin alone (**Figure 17**, panels A-F) or saponin and TX100 together (**Figure 17**, panels G-I), as described in this chapter's Materials and Methods section (2.2). They were then subjected to immunofluorescence confocal microscopy as before. The positions of the blue DAPI-stained nuclei are shown in the merged images (**Figure 17**, panels C, F, and I).

When the cells were permeabilized with saponin alone, RdRp immunofluorescence appeared in clustered structures (**Figure 17**, panels B and C, closed arrowheads) that localized to the outer mitochondrial membrane marker monoamine oxidase (**MAO**), as evidenced by an OC value of 82% (**Table 4**). Under these permeabilization conditions the inner mitochondrial membrane marker cyto-

Figure 17: The NoV RdRp localizes to the surface of mitochondria. BSR-T7/5 cells were transfected with pT7-N1-HA as before and incubated for 24 h. Cells were fixed with paraformaldehyde and permeabilized with saponin, either alone (**A – F**) or together with Triton X-100 (**G – I**). HA-tagged RdRp was immunostained with mouse anti-HA monoclonal primary and FITC-labeled goat anti-mouse secondary antibodies (green; **B**, **E**, and **H**), as described in the legend to **Figure 15**. MAO was immunostained with rabbit anti-MAO polyclonal primary and Texas Red (**TR**)-labeled goat anti-rabbit secondary antibodies (red; **A**). COX3 was immunostained with goat anti-COX3 polyclonal primary and TR-labeled rabbit anti-goat secondary antibodies (red; **D** and **G**). Merged signals, including DAPI staining of the nuclei, are shown in panels **C**, **F**, and **I**; yellow signal on merge indicates co-localization. Closed arrowheads indicate RdRp expression in transfected cells; open arrowheads indicate untransfected cells. Scale bar = 10 μ M.



chrome c oxidase subunit III (**COX3**) was not detected (**Figure 17**, panels D-F) and the corresponding OC value was zero (**Table 4**). When cells were treated with both saponin and TX100 to permeabilize the mitochondrial membranes, COX3 immunofluorescence became visible (**Figure 17**, panel G) and localized with RdRp immunofluorescence (**Figure 17**, panels H and I, closed arrowheads), with an OC value of 88% (**Table 4**). As before, the mitochondria in the cells expressing the RdRp exhibited clustering (**Figure 17**, closed arrowheads), in marked contrast to the diffuse cytoplasmic staining pattern seen in the surrounding untransfected cells (**Figure 17**, open arrowheads). These results suggest that the NoV RdRp interacted with the outer surface of mitochondria and was oriented such that its C-terminus, which contains the HA tag, was exposed to the cytoplasm in transfected mammalian cells.

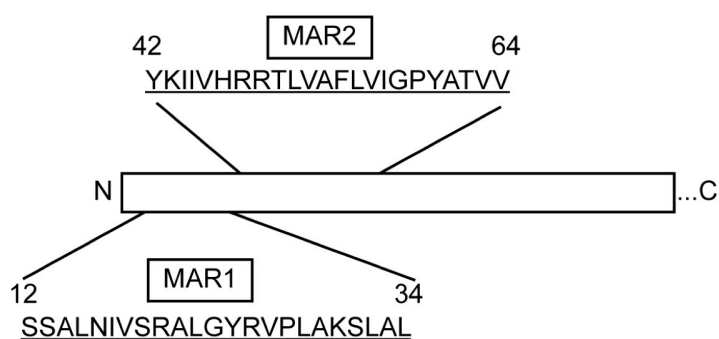
Predicted membrane associated regions of the NoV RdRp. As a first step in characterizing the interaction of the NoV RdRp with mitochondria, we used proteomic *in silico* prediction software to examine its likelihood of interacting with mitochondrial or other cellular membranes. The N-terminal 123 amino acids of NoV protein A (124, 128) are shown schematically in **Figure 18A**. Several of these programs (Pspred, TMPred, and SOSUI) predict the presence of two potential membrane-associated regions (**MARs**) at the RdRp N-terminus, although the exact boundaries of these regions vary slightly among the programs used to predict them (38, 115, 116, 165). For example, Pspred's MEMSAT-SVM topology analysis predicted two MARs in the NoV RdRp, at aa 28-46 and aa 42-57; TMPred predicted potential transmembrane helices at aa 26-46 and aa 44-65; and the SOSUI prediction tool predicted two MARs at aa 12-34 and aa 42-64. We show the SOSUI prediction in **Figure 18B** since it encompasses the other

Figure 18: The NoV RdRp is predicted to contain two membrane-associated regions. (A) The primary sequence of the N-terminal 123 amino acids of NoV protein A is reproduced here; accession # NP_077730.1 and references (124, 128). (B) SOSUI software (115) predicted two potential 23-aa transmembrane domains (underlined), located near the N-terminus of the NoV RdRp, corresponding to aa 12-34 (**MAR1**) and 42-64 (**MAR2**), respectively. (C) The TopPred II topology prediction program identified a large hydrophobic region at the N-terminus of the NoV RdRp that overlaps the predicted MARs. Hydrophobicity was calculated using the method of Kyte and Doolittle with a core window size of 11 and a full window of 21 aa and plotted as a function of amino acid position using GraphPad Prism software. Solid line, upper cutoff; dashed line, lower cutoff.

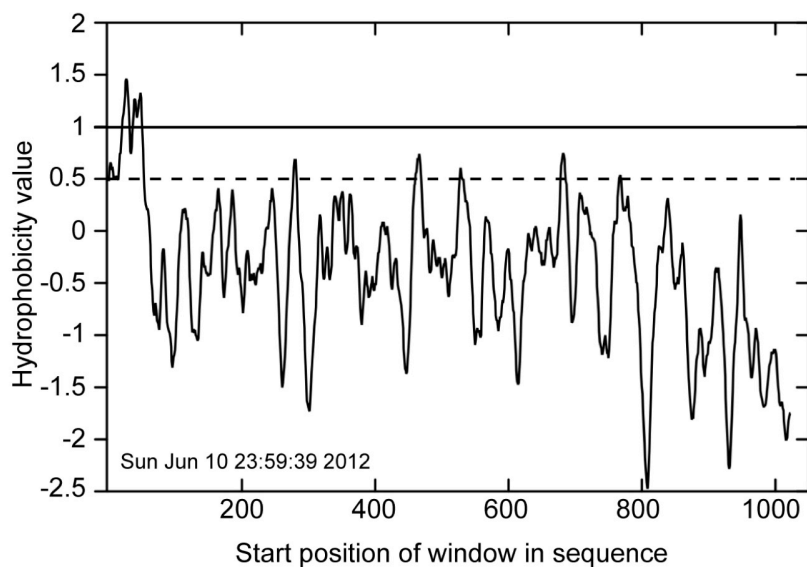
A

1
N-MLNYETIINGASSALNIVSRALGYRVPLAKSLALVAGSCVV
YKIIVHRRTLVAFLVIGPYATVVQHRLPMALQRAII EYTRED
REISLFPQNSIVSAEHARKADNGHPISGGTRDVARETISL...C
123

B



C



two predictions. These regions were designated MAR1 (aa 12-34), which contains the sequence SSALNIVSRALGYRVPLAKSLAL and MAR2 (aa 42-64), which contains the sequence YKIIVHRRTLVAFLVIGPYATVV. Furthermore, TopPred II topology prediction software (51) predicted the presence of two hydrophobic regions near the N-terminus of the RdRp (**Figure 18C**) that overlap the predicted MARs and are likely to interact with membranes.

The MARs predicted for NoV do not share homology with those found within the FHV, GGNNV, or AHNV RdRp sequences (106, 166, 168), which also fail to overlap one another. This is not surprising, since the RdRps of alpha- and betanodaviruses share little (less than 30%) sequence identity at the amino acid level (128). While the RdRps of FHV and GGNNV are both predicted to contain helices that span the membrane (106, 168), the MARs in the NoV RdRp are unlikely to be membrane-spanning alpha helices, due to the presence of charged residues within the predicted helical regions (**Figure 18A**) not found for FHV and GGNNV. Nevertheless, the observation that the N-terminal region of the NoV RdRp encompass two hydrophobic regions and contains multiple predicted MARs warranted further investigation into the RdRps potential for association with membranes.

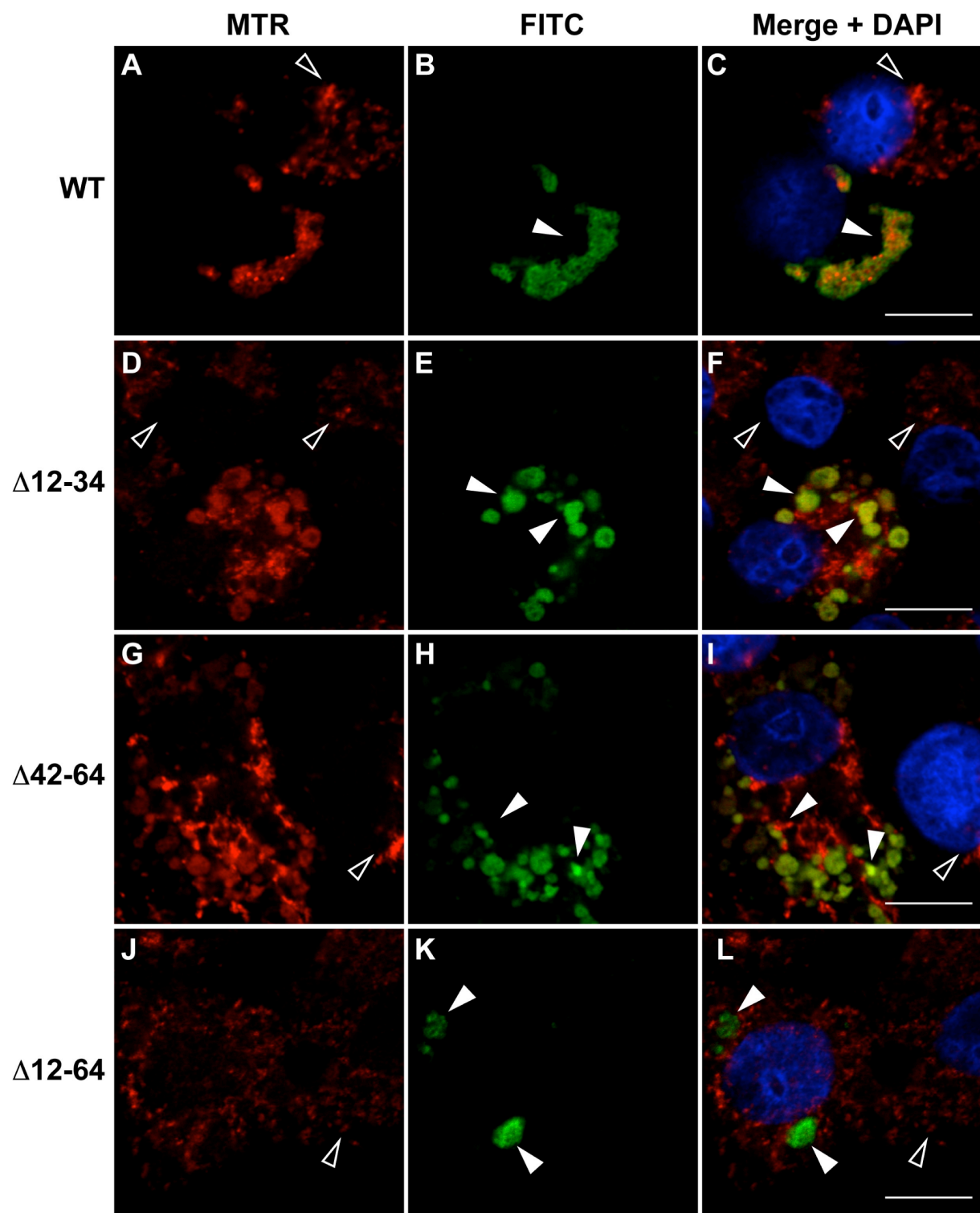
Localization of NoV RdRp MAR deletion mutants in transfected mammalian cells. To determine whether the predicted MARs (**Figure 18**) play a direct role in localizing the RdRp to mitochondria, we deleted the MAR1 and MAR2 regions from our HA-tagged RdRp expression constructs, either singly (N1 Δ 12-34-HA or N1 Δ 42-64-HA, respectively) or both together (N1 Δ 12-64-HA) and tested the effects of these deletions on RdRp localization in mammalian cells. BSR-T7/5 cells were transfected with

plasmids expressing either WT or the MAR deletions and at 24 hpt were stained with MTR, fixed, and processed for immunofluorescence confocal microscopy as described in this chapter's Materials and Methods section (2.2).

For both single MAR deletion mutants ($\Delta 12-34$ and $\Delta 42-64$), the majority of the RdRp staining pattern (green signal designated by closed arrowheads) still localized to mitochondria with OC values of 88% and 85%, respectively (**Table 4**), but many mitochondria now no longer appeared to be associated with the RdRp, judging by the reduction in yellow signal (closed arrowheads) in the merged images (**Figure 19**, compare panels D-I with panels A-C). In contrast, deletion of both MARs resulted in reduction of mitochondrial localization, with the level of overlap between MTR and FITC reduced to 47% (**Table 4**), and a loss of mitochondrial clustering (**Figure 19**). Instead, the double deletion mutant exhibited altered localization, such that the RdRp was now detected in discrete sites within the cell (**Figure 19**, compare panels J-L with panels A-C). These results suggest that complete localization of the NoV RdRp to mitochondria requires both predicted MARs, raising the possibility that the RdRp may interact directly with mitochondrial membranes.

Membrane association of the NoV RdRp in transfected mammalian cells. To determine whether the NoV RdRp interacts with membranes in a MAR-dependent manner, we transfected BSR-T7/5 cells with either pT7-N1-HA or pT7-N1 $\Delta 12-64$ -HA. After incubation, we lysed the cells and performed differential centrifugation to collect intracellular membranes as described in this chapter's Materials and Methods section (2.2). Post-nuclear lysates (**PNLs**) were subjected to centrifugation at 20,000 x g to pellet the majority of intracellular membranes, including the mitochondrial membranes

Figure 19: Subcellular localization of the NoV RdRp is dependent on both MARs. BSR T7/5 cells were transfected with pT7-N1-HA (**B**), pT7-N1 Δ 12-34-HA (**E**), pT7-N1 Δ 42-64-HA (**H**), or pT7-N1 Δ 12-64-HA (**K**). At 24 hpt, mitochondria were labeled with MTR (red) and cells were fixed and permeabilized. HA-tagged RdRp was detected by immunostaining (green) as described in the legend to **Figure 15**. Merged signals, including DAPI staining of the nuclei (blue), are shown; yellow signal on merge indicates co-localization. Closed arrowheads indicate RdRp expression in transfected cells; open arrowheads indicate untransfected cells. Scale bar = 10 μ M.

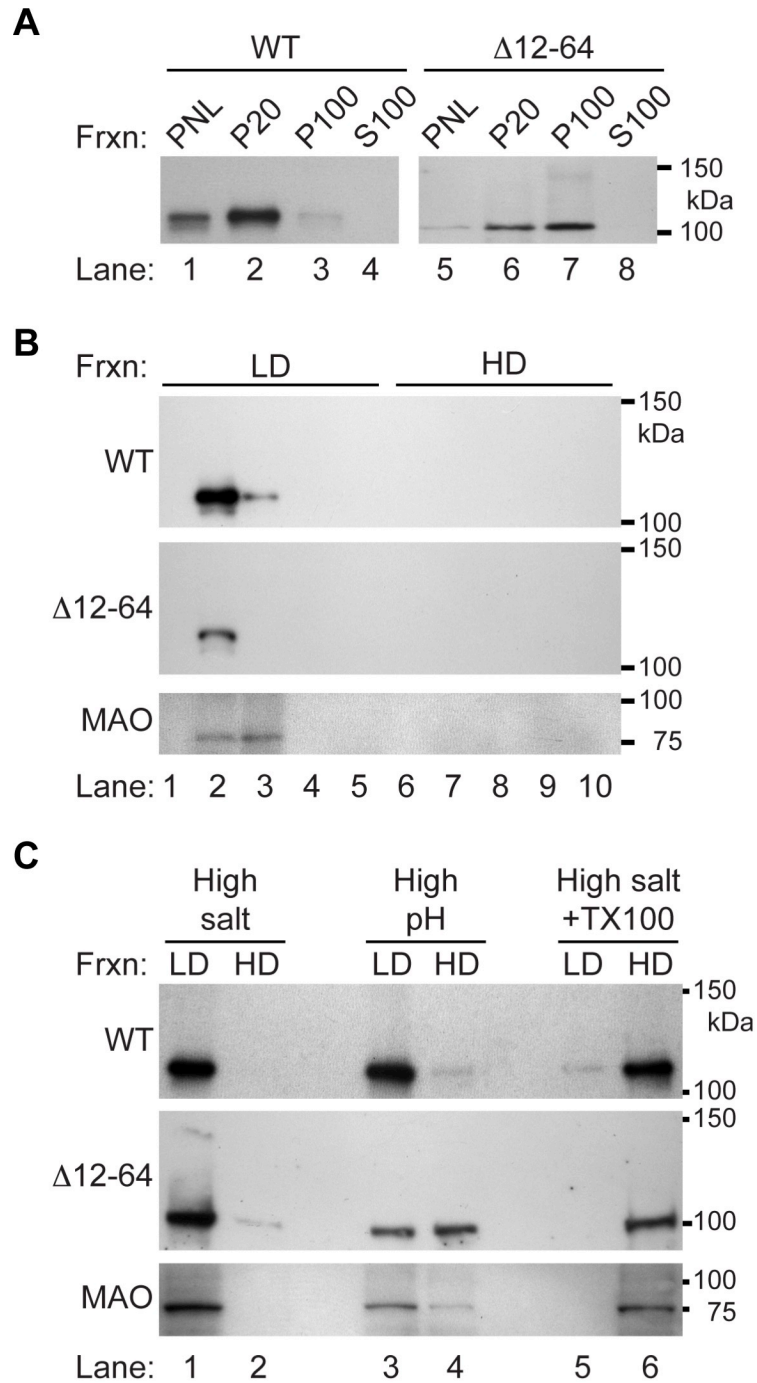


(the **P20** fraction). The resulting supernatant (the **S20** fraction) was subjected to further centrifugation at 100,000 x *g* to pellet microsomal membranes (the **P100** fraction); cytosolic proteins will remain in the supernatant (the **S100** fraction). The PNLs and the P20, P100, and S100 fractions were analyzed by Western blot for the presence of the RdRp using the anti-HA antibodies (**Figure 20A**). Under these conditions, the WT NoV RdRp was found to sediment mostly in the P20 fraction, although some was detected in the P100 fraction as well (**Figure 20A**, lanes 2 and 3). It was not detected in the cytosolic fraction (**Figure 20A**, lane 4). These results suggest that the RdRp may be a membrane-associated protein that sediments with the cellular fraction containing the majority of mitochondrial membranes (96-98).

Since the results of our confocal microscopy experiments suggest that both MARs were required for mitochondrial localization (**Figure 19**), we hypothesized that deletion of the MARs from the RdRp would prevent its association with membranes. However, the $\Delta 12-64$ RdRp mutant was detected in both the P20 and P100 membrane pellets rather than in the cytosolic S100 fraction as we had predicted (**Figure 20A**, lanes 5-8). In contrast to the WT RdRp, however, the mutant was more evenly distributed between the low- and high-speed pellets. These results suggest that $\Delta 12-64$ RdRp mutant remained associated with membrane-containing fractions even in the absence of the MARs, although it no longer associated with mitochondria (**Figure 19**).

To further explore whether the NoV RdRp specifically interacts with intracellular membranes, we used equilibrium density gradients to analyze the flotation profiles of the WT and mutant RdRps isolated from transfected BSR-T7/5 cells (**Figure 20B**), as described in this chapter's Materials and Methods section (**2.2**). We collected fractions

Figure 20: Analysis of NoV RdRp intracellular membrane association. Intracellular membranes were harvested from BSR-T7/5 cells transfected with either pT7-N1-HA or pT7-N1 Δ 12-64-HA by differential centrifugation. Proteins were separated on SDS-PAGE gels and detected by immunoblotting with antibodies specific for the HA tag or for the mitochondrial outer membrane protein MAO as indicated in the figure. The relative positions of the protein standards are indicated at right. **(A)**, proteins were examined in post-nuclear lysates (**PNL**), membrane fractions P20 and P100 (pellets from 20,000 and 100,000 x g spins, respectively), and the cytosolic fraction S100 (supernatant from 100,000 x g spins). The blot for pT7-N1 Δ 12-64-HA (at right) was an overexposure necessitated by the production of lower levels of the mutant protein than the WT. **(B)**, intracellular membranes were fractionated on an equilibrium density gradient, as described in Materials and Methods, and proteins present in the low-density (**LD**) and high-density (**HD**) fractions were examined. **(C)**, membrane fractions were treated with high salt, high pH, or high salt with TX100 prior to fractionation by equilibrium density gradient.



of equal volumes beginning at the top of the gradient and analyzed the distribution of the NoV RdRp and the outer mitochondrial membrane protein MAO by Western blot. Under these conditions, intracellular membranes will float to the low-density (**LD**) fractions closer to the top of the gradient, where they form a membrane “wafer” that also contains membrane-associated proteins (167, 168, 244). In contrast, if a protein is not specifically associated with a membrane, it will be present in the high-density (**HD**) fractions in the bottom portion of the gradient.

The WT NoV RdRp floated to fractions 2 and 3 (**Figure 20B**, top panel), which correspond to the fractions harboring the membrane wafer. MAO, which is an integral membrane protein, was also found in the same two fractions (**Figure 20B**, bottom panel). These results support our previous finding that the NoV RdRp specifically interacts with intracellular membranes in transfected BSR-T7/5 cells. In contrast, the $\Delta 12-64$ mutant protein also specifically floated with intracellular membranes and was detected in fraction 2 of the gradient (**Figure 20B**, middle panel). Together, the data presented in **Figures 19, 20A, and 20B** suggests that, while the WT RdRp associated with mitochondrial membranes, the $\Delta 12-64$ version of the protein was associated with another co-sedimenting membrane present in the P20 fraction but was no longer associated with mitochondria. The implications of the mutant’s altered localization will be explored further in the Conclusions section of this chapter (**2.4**). Nevertheless, we further characterized the nature of the NoV RdRps interaction with mitochondrial membranes by examining the conditions required to disrupt the interaction and remove it from the membranes.

Membrane dissociation suggests the NoV RdRp is an integral membrane protein. The nature of the NoV RdRps membrane association was examined using extraction reagents known to separate integral from peripheral membrane proteins. Under high salt or alkaline pH conditions, peripheral membrane proteins are released from the membrane, while integral membrane proteins remain bound to intact membrane sheets; removal of integral membrane proteins is facilitated by solubilization with detergents (80, 186). Therefore, the P20 membrane fractions from cells transfected with WT or mutant versions of the RdRp were extracted, treated with high salt, high pH, or high salt with TX100, and fractionated on an equilibrium density gradient as described in this chapter's Materials and Methods section (2.2). The gradients were divided into equal volume fractions and MAO and RdRp proteins were detected by Western blot analysis. As before, fractions from the upper portion of the gradient containing the membrane wafer were designated the LD fractions and those from the bottom portion containing the soluble proteins were designated the HD fractions.

Membrane association of the NoV RdRp was not disrupted by the presence of high salt or high pH (**Figure 20C**, top panel, lanes 1-4), but the protein was removed from the LD membrane fraction by treatment with high salt and detergent together (**Figure 20C**, top panel, lanes 5 and 6). Similar results were obtained for the outer mitochondrial integral membrane protein MAO under the same conditions (**Figure 20C**, bottom panel, lanes 1-6). These results suggest the NoV RdRp is associated with intracellular membranes from transfected mammalian cells, with its behavior most resembling that of an integral membrane protein.

In contrast, some of the $\Delta 12-64$ mutant RdRp was removed from membranes by high salt (**Figure 20C**, middle panel, lanes 1 and 2) and just over half was dissociated by treatment with alkaline pH (**Figure 20C**, middle panel, lanes 3 and 4). The detectable amount of mutant RdRp was solubilized by treatment with high salt and TX100 (**Figure 20C**, middle panel, lanes 5 and 6). The partial release of the mutant RdRp by high salt and high pH may suggest that deletion of aa 12-64 mutation alters the RdRps mechanism of membrane association. Clearly, sequences within the hydrophobic 52 aa MAR region play a major role in anchoring the RdRp to intracellular membranes, although the exact nature of that interaction remains to be determined.

The levels of the mutant RdRp proteins detected by confocal microscopy (**Figure 19**) or by Western blot analysis (**Figure 20**) were decreased relative to the WT. However, it was unclear whether this was due to it being synthesized at lower levels or whether it was being degraded at an increased rate after synthesis. To test whether the mutant RdRp was being degraded via a proteasome-mediated pathway, we examined the effect of the proteasome inhibitor MG132 (262) on WT and mutant RdRp accumulation. Cells were transfected with the WT or $\Delta 12-64$ RdRp expression plasmids as before, left untreated or treated with MG132 for the 8 h prior to harvest (starting at 16 hpt), and proteins were subjected to Western blot analysis with the anti-HA antibodies as before (**Figure 21**). In the presence of MG132, the levels of RdRp increased for both WT and the $\Delta 12-64$ mutant (**Figure 21**, lanes 4 and 5, respectively). This data suggests that, while there is turnover of the RdRp protein during the NoV replicative cycle, the $\Delta 12-64$ deletion mutant does not appear to exhibit increased proteasomal degradation compared to the WT RdRp (**Figure 21**). Since there is no apparent increase in

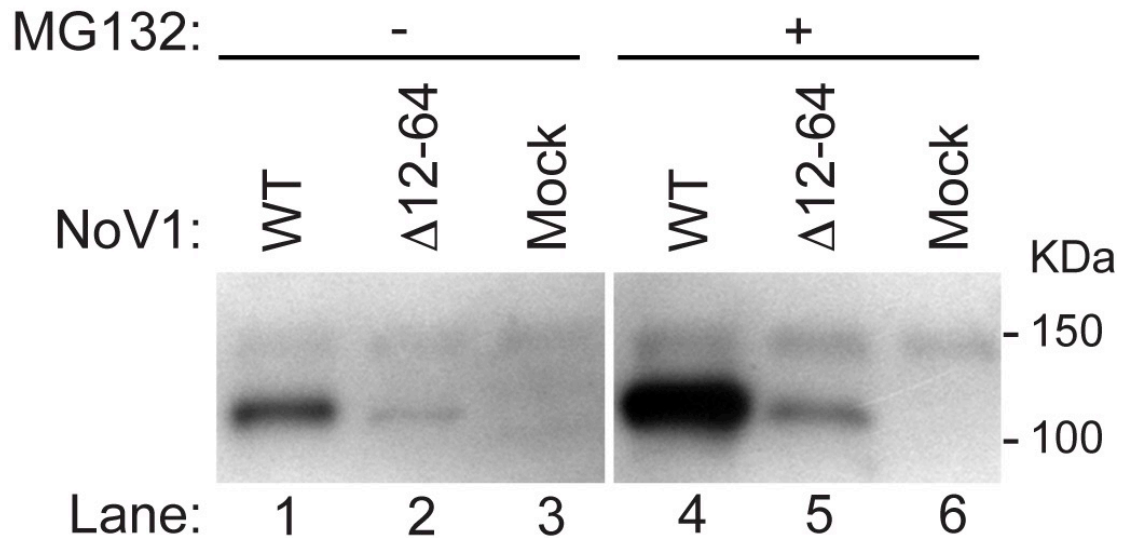


Figure 21: Deletion of the MARs reduces RdRp expression levels but did not appear to increase proteasome-mediated degradation. BSR-T7/5 cells were transfected with pT7-N1-HA or pT7-N1Δ12-64-HA as described for **Figure 14**. Cells in duplicate wells were left untreated (**lanes 1 – 3**) or treated with the proteasome inhibitor MG132 for the 8 h prior to harvest (**lanes 4 – 6**). Proteins were detected by immunoblotting with antibodies specific for the HA tag as described in the legend to Figure 2. The relative positions of the Precision Plus (Bio-Rad) protein standards are indicated at right.

degradation of the mutant RdRp, we conclude that it is being synthesized at lower levels. Since NoV RNA1 serves as both the mRNA for RdRp synthesis and RNA replication template, lower levels of RdRp synthesis could result from an inability of the mutant to establish RNA replication complexes or to replicate NoV RNA1. We will examine each possibility in the following sections.

NoV RdRp-catalyzed RNA synthesis localizes to mitochondria in transfected mammalian cells. In light of the localization of the RdRp to mitochondrial membranes, we wondered whether this also represented the site of RC formation. We therefore transfected BSR-T7/5 cells with pT7-N1-HA and labeled the RdRp-catalyzed viral RNA synthesis products with BrUTP as described in this chapter's Materials and Methods section (2.2). Labeling was performed in the presence of ActD to inhibit transcription by cellular RNA polymerase II; under these conditions, only the products of the viral RdRp are labeled. Mitochondria were also labeled with MTR and cells were fixed and permeabilized. The ActD resistant BrUTP-labeled viral RNA synthesis products were immunostained with monoclonal anti-bromodeoxyuridine primary and FITC-labeled secondary antibodies, as described (2.2).

Mock-transfected cells (**Figure 22**, panel A) and untransfected cells (**Figure 22**, panel D, cell on right indicated by open arrowhead) showed no BrUTP-labeling of newly synthesized RNA (green signal) in the presence of ActD and OC values of zero (**Table 4**); these cells served as internal negative controls. In cells transfected with pT7-N1-HA, the MTR staining pattern (red signal) displayed the distinct clustered networks we observed previously (**Figure 22**, panels D and F, cell on left indicated by closed arrowheads). In these same cells, we detected newly synthesized BrUTP-labeled RNA

Figure 22: NoV RdRp-catalyzed RNA synthesis localizes to mitochondria in transfected BSR-T7/5 cells. BSR-T7/5 cells were transfected with pT7-N1-HA or pT7-N1 Δ 12-64 (Δ **MAR1+2**) and incubated for 19.5 h. Cells were pre-treated with act D for 30 min, then newly synthesized viral RNA was labeled with bromo-UTP (**BrUTP**) for 4 h in the presence of act D. At 24 hpt, mitochondria were stained with MTR (red) and cells were fixed and permeabilized. BrU-labeled viral RNA was detected by immunostaining with monoclonal anti-BrdU primary and FITC-labeled secondary antibodies (green; **BrU**). Merged signals, including DAPI staining of the nuclei (blue), are shown (Merge+DAPI); yellow signal on merge indicates co-localization. Closed arrowheads indicate BrU-labeled viral RNA in transfected cells; open arrowheads indicate untransfected cells. Scale bar = 10 μ M.

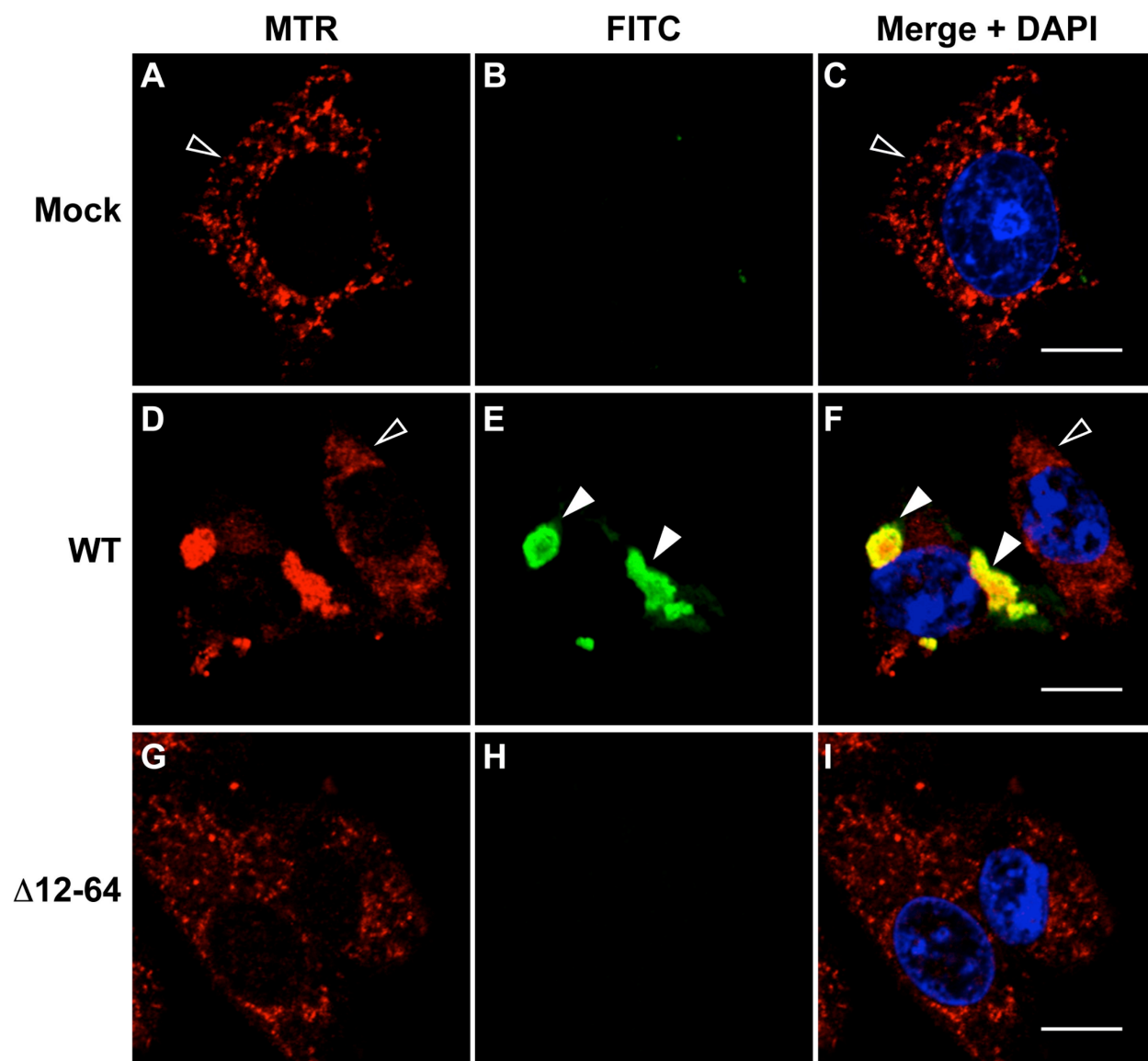
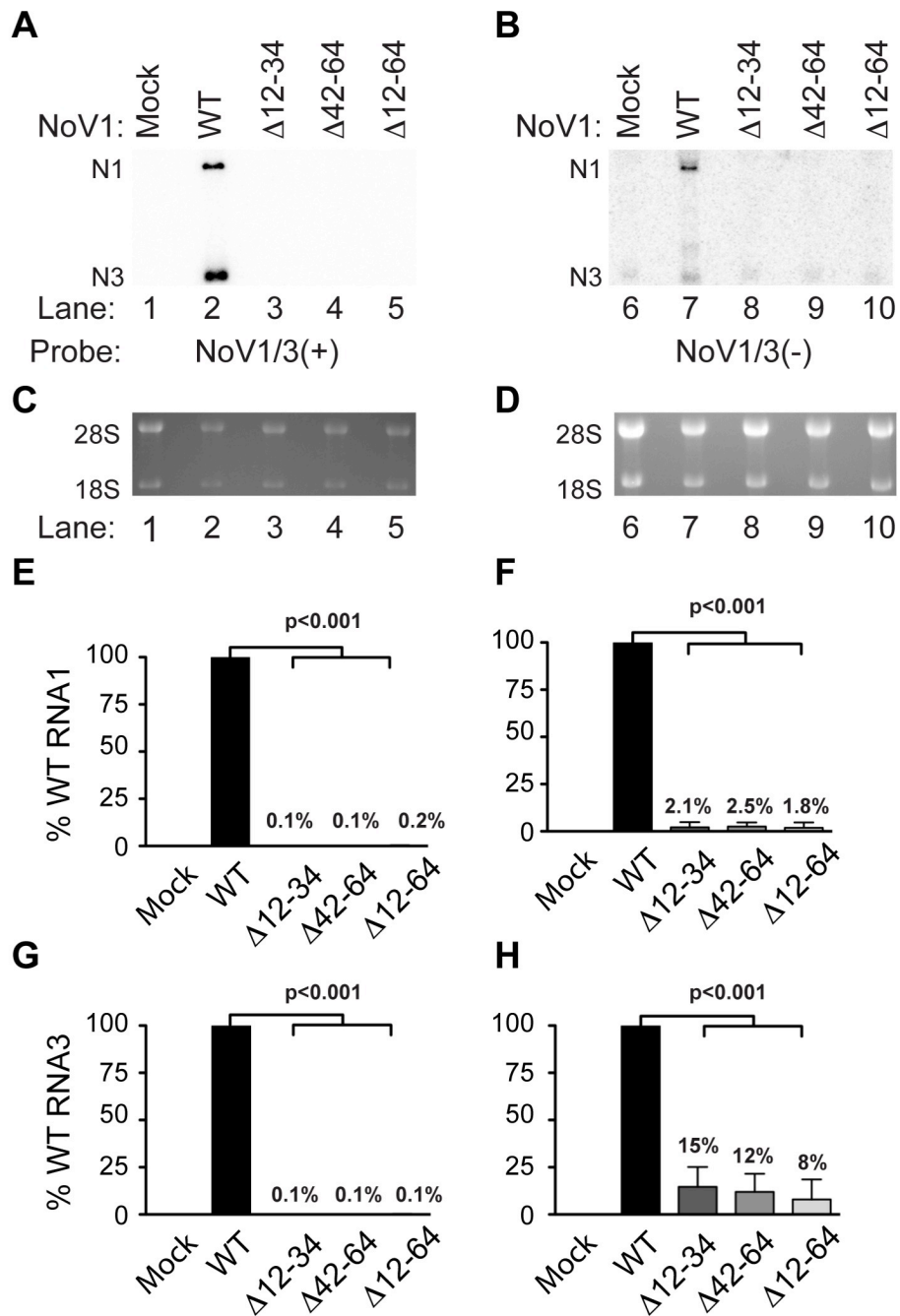


(**Figure 22**, panel E, green signal indicated by closed arrowheads), which appeared in clustered cytoplasmic structures that localized with MTR in the merged image (**Figure 22**, panel F, yellow signal indicated by closed arrowheads), with an OC value of 94% for MTR and FITC (**Table 4**). These results suggest that NoV RNA synthesis occurs in close proximity to the observed clustered mitochondrial networks, which also harbor the RdRp, and that these clusters represent membrane-associated RCs.

Deletion of one or both MARs results in severe defects in RNA replication.

Since deletion of the MARs disrupted mitochondrial localization of the RdRp and the RCs, we tested the effect of these mutations on viral RNA replication. BSR-T7/5 cells were transfected with plasmids expressing the WT RdRp, the single MAR mutations N1 Δ 12-34 and N1 Δ 42-64, or the double mutation that deleted both MARs (N1 Δ 12-64). After incubation, total RNA was isolated and separated on denaturing formaldehyde-agarose gels and viral RNA replication products were detected by Northern blot hybridization using probes specific for the positive (**Figure 23**, panel A) or negative (**Figure 23**, panel B) strands of RNA1 and RNA3 as described for **Figure 1** and in references (124, 202, 212). The positive and negative strands of RNA1 and RNA3 were quantitated by densitometry, as shown in **Figure 23**, panels E-H. All three mutations resulted in severe defects in RNA1 replication and RNA3 synthesis (**Figure 23**). In some experiments, we detected low levels of the negative strand of RNA3 for each mutant (**Figure 23**, panel H). However, the presence of a cross-reactive RNA species in the mock-transfected sample (**Figure 23**, panel B, lane 6) complicated interpretation of this result, so it is possible that this apparent synthesis of an RNA replication intermediate represents a technical artifact. The density from the mock-transfected lane

Figure 23: Deletion of the MARs on the NoV RdRp results in a severe defect in RNA replication. Total cellular RNAs were isolated from BSR-T7/5 cells transfected with either pT7-N1 (**WT**), pT7-N1 Δ 12-34 (**Δ MAR1**), pT7-N1 Δ 42-64 (**Δ MAR2**), or pT7-N1 Δ 12-64 (**Δ MAR1+2**), separated on denaturing gels, and subjected to Northern blot hybridization analysis as described in the legend to **Figure 14**. The positive (**A**) or negative (**B**) strands of RNA1 and RNA3 were detected as described; as before, rRNAs were stained with ethidium bromide for use as loading controls (**C** and **D**, respectively). Quantitation of (+) and (-) strands of N1 and N3 relative to WT is shown in panels **E-H**: **E**, N1 (+); **F**, N1 (-); **G**, N3 (+); and **H**, N3 (-). The relative RNA values from three independent experiments are presented as mean values \pm standard deviations.



was therefore subtracted from the other lanes to reflect this background species (**Figure 23**, panel H). The inability of the double deletion to replicate was not unexpected in light of our observation that this mutant fails to form RCs (**Figure 22**). However, even the single deletions, which appear to retain some ability to interact with mitochondria (**Figure 19**), fail to synthesize detectable RNA replication products.

2.4 Conclusions

Localization of RCs to intracellular membranes is a hallmark of positive-strand RNA viruses. In this study we show that the NoV RdRp localized to the OMM in mammalian cells at 37°C, consistent with the presence of two computer-predicted MARs. Expression of the RdRp in cells induced mitochondria to cluster into distinct cytoplasmic networks between 4 and 8 hpt, but only when the RdRp was expressed from a replicable template (**data not shown**). While not yet visualized at the ultrastructural level, we hypothesize that the clustered phenotype seen in cultured cells represents the same altered mitochondrial morphology and mitochondrial aggregation previously described for NoV-infected muscle tissue (86-88). We further show that RNA synthesis also localizes to these RdRp-induced mitochondrial networks, further establishing the mitochondria as the site of viral RC formation.

Our data suggests that the NoV RdRp interacts with the OMM, although it remains possible that the RdRp could localize to mitochondria-associated endomembranes as well. The results of biochemical assays favor our original interpretation although additional experiments may be required to resolve the issue. Nevertheless, the NoV RdRp co-sedimented with the intracellular membrane fraction

(P20) that contains the mitochondria rather than in the P100 fraction where endosomal proteins would be found. The specific interaction between the NoV RdRp and membranes within this fraction was confirmed by a flotation assay and mimicked that of a mitochondrial integral membrane protein, MAO.

While the topological data presented here suggest that the NoV RdRp is an OMM protein, we pondered the nature of its interaction with these membranes. In **Figure 18** we show that the NoV RdRp contains two extremely hydrophobic regions at its N-terminus. Several secondary structure prediction programs (Pspred, TMPred and SOSUI) predict the presence of two MARs within the bounds of aa 12 to 65 of the NoV RdRp N-terminus. We decided to pursue the SOSUI predictions since they overlap the predictions of the other programs and because the SOSUI predicted MARs are separate stretches of amino acids.

Proper localization of viral nonstructural proteins (including RdRps) to membranes and membrane association is dependent on the integrity of the primary and secondary structure of the protein. For the NoV RdRp, these properties are mediated by the MARs, since their deletion from the RdRp results in a multitude of deleterious phenotypes. Specifically, their deletion resulted in defects in localization of the RdRp to mitochondria and RdRp-induced clustering of the mitochondria (**Figure 19**), in RdRp protein levels (**Figures 20 and 21**), in localization of RCs (**Figure 22**) and in RNA replication (**Figure 23**). Interestingly, the double deletion mutant retained its ability to associate with intracellular membranes (**Figure 20**). However, localization of the mutant RdRp changed from mitochondrial to unidentified but discrete sites in the cytoplasm (**Figure 19**). The presence of the mutant RdRp in both the P20 and P100 fractions in

the differential centrifugation experiments and its retention in the LD portion of the density gradients (**Figure 20**) lends credence to the idea that these discrete sites are associated with cellular membranes.

Our observation that the mutant RdRp exhibits characteristics of a peripheral membrane protein (**Figure 20**) may suggest that the MARs play a role in the interaction of the NoV RdRp with mitochondrial membranes as an integral membrane protein. Yet the question remains as to why an RdRp that lacks the MARs remains associated with membranes rather than becoming soluble, as we had expected. In light of the observation that many viral proteins contain amphipathic alpha helices important for association with membranes and for RNA replication (217), similar structural elements may play a role in the interaction between the NoV RdRp and the OMM. We hypothesize that these interactions remain intact in the MAR deletion mutants. It is also possible that the mutant (and probably the WT) RdRp interacts with one or more membrane proteins that help to direct it to membranes.

As noted above, deletion of the MARs also appears to result in a decrease in RdRp protein expression levels (**Figures 20 and 21**). However, it remained unclear whether less of the mutant RdRp was detected in these experiments because it was being degraded after synthesis or because it was being synthesized at lower levels. To test whether the mutant RdRp was being degraded via a proteasome-mediated pathway, we examined the effect of the proteasome inhibitor MG132 (262) on accumulation of the mutant protein. In the presence of MG132, the levels of RdRp accumulation increased for both WT and the $\Delta 12-64$ mutant (**Figure 21**). These data suggest that, while there is turnover of the RdRp protein during the NoV replicative

cycle, the $\Delta 12-64$ deletion mutant does not appear to exhibit increased proteasomal degradation compared to the WT RdRp (**Figure 21**). Since there is no apparent increase in degradation of the mutant RdRp, we conclude that it is being synthesized at lower levels. This interpretation is supported by the failure of the mutant RNA1 to replicate (**Figure 23**), resulting in greatly reduced levels of the mRNA from which the mutant RdRp is translated.

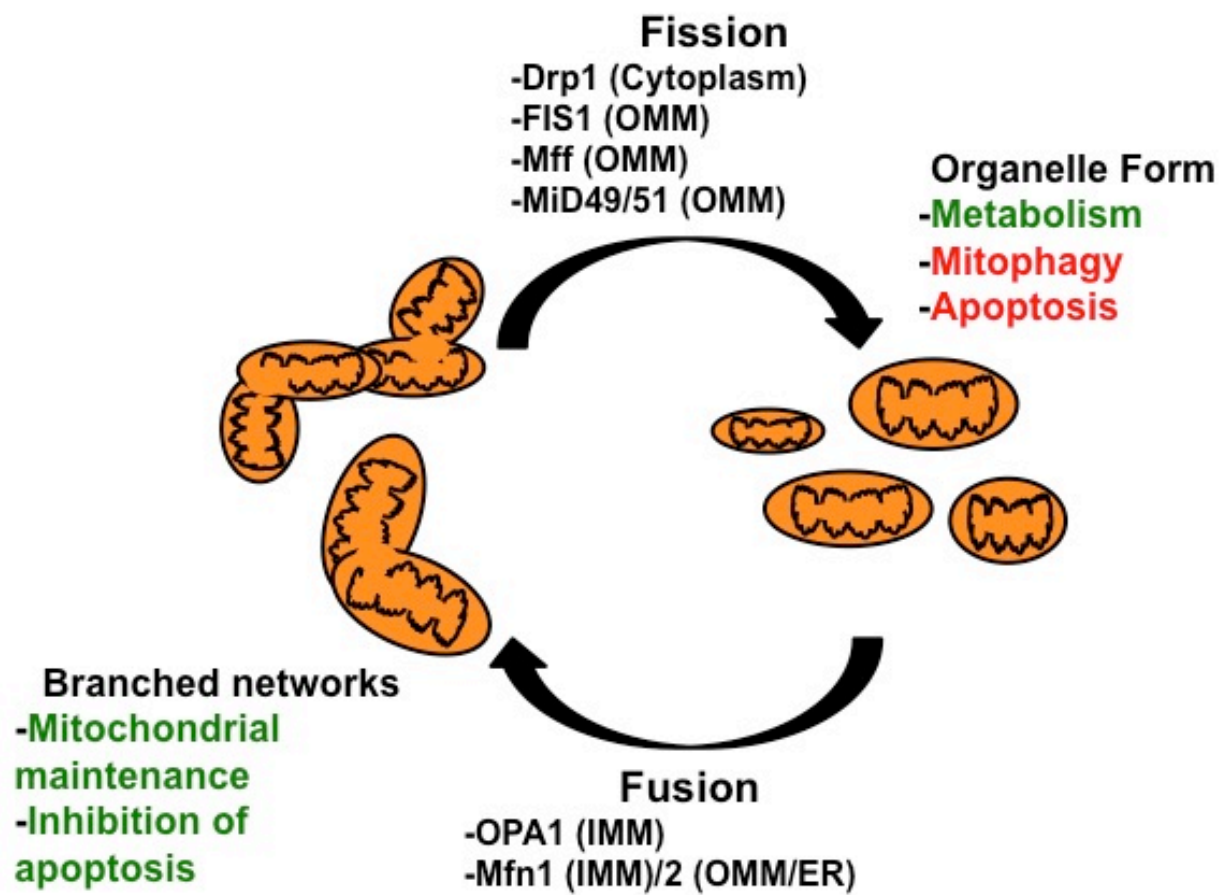
Chapter 3: NoV RC Formation Induces Imbalance in Mitochondrial Dynamics

3.1 Introduction

The central focus of **Chapter 2** was to determine the subcellular localization of NoV RCs in mammalian cells. During the course of that study we discovered the NoV RdRp is an integral membrane protein that establishes RCs on the OMM and induces mitochondrial clustering. In contemplating the mechanism(s) by which RCs are formed and RdRp-mediated clustering occurs, we realized that the morphology of these clustered mitochondria resembled a similarly clustered morphology observed in cells where the system controlling mitochondrial distribution and morphology has been disrupted (239, 240). This led us to hypothesize that NoV may be subverting these control mechanisms as a means of establishing its RCs during the replicative cycle. Therefore, we examined the effect of RdRp expression on key components in these regulatory pathways, which are outlined below.

Mitochondria are structurally unique organelles with a double membrane forming distinct compartments: the outer mitochondrial membrane (**OMM**), intermembrane space, inner mitochondrial membrane (**IMM**), and matrix (164). They function as dynamic compartmentalized machines involved in many vital cellular processes including production of energy in the form of adenosine triphosphate (**ATP**), metabolism of fatty acids and sugars, and synthesis of steroids and lipids. The familiar organelle form exists in equilibrium with a branched interconnected network comprised of several mitochondria joined by fused membranes (185). This balanced morphological cycle is known as mitochondrial dynamics and is driven by opposing processes of fusion and fission (**Figure 24**), controlled by separate sets of proteins. Mitochondrial dynamics are

Figure 24: Mitochondrial morphology dynamics. In healthy cells, mitochondria cycle between a fused poly-organelle reticulum and individual organelle forms in a process known as mitochondrial dynamics. Several proteins participate in mitochondrial dynamics, which is tightly regulated and is involved in several vital cellular processes. Mitochondria undergo fusion to share DNA and maintain organelle integrity in preparation for mitosis or repair. Mitochondrial fission controls the distribution of mitochondria between daughter cells. During cellular stress fission is involved in initiation of apoptosis and degradation of damaged or malfunctioning mitochondria via mitophagy. Reviewed in (21, 237).



integral to maintaining cellular homeostasis by facilitating many processes including maintenance of mitochondrial membrane integrity, mitochondrial inheritance, and apoptosis (21, 185, 291). Mitochondrial dynamics has been shown to play a role in development and progression of diseases. Impairments in mitochondrial dynamics have potential roles in neurodegenerative disease, cardiovascular disease, diabetes, and tumorigenesis (99, 105, 107, 134). Specifically, mutated OPA1 GTPase is involved in Dominant Optic Atrophy, a syndrome that affects optic nerves (59), mutated Mitofusin 2 (**Mfn2**) leads to Charcot-Marie-Tooth neuropathy type 2A, which affects motor/sensory neurons (274), and increased fission and decreased fusion is involved with the progression of Huntington's and Alzheimer's diseases (44, 247, 248).

Mitochondrial fusion (**Figure 24**) is mediated by the coordinated work of several large mitochondrial membrane-bound GTPases (43, 59, 187). Mfn1 and Mfn2 are both transmembrane proteins of the OMM involved in mitochondrial fusion, and Mfn2 is also present on the surface of the ER where it is involved in ER-mitochondria tethering (297). This process involves individual mitochondria being tethered together by their outer membranes by Mfn1 and Mfn2 interactions in which are both Mfns are able to form homo- and hetero-oligomers (43, 143). Mfn oligomerization during tethering occurs through antiparallel interaction between both Mfn C-terminal coiled-coiled domains, which links their heptad repeat regions (**HR2**) (143). The next step of fusion involves OPA1, which is a fusion GTPase expressed as several splice variants in the intermembrane space and as a transmembrane protein of the IMM (59, 187). After mitochondrial tethering, OPA1 finalizes the fusion process by mediating IMM fusion between the tethered mitochondria in a GTP-dependent fashion (297). OPA1 is also

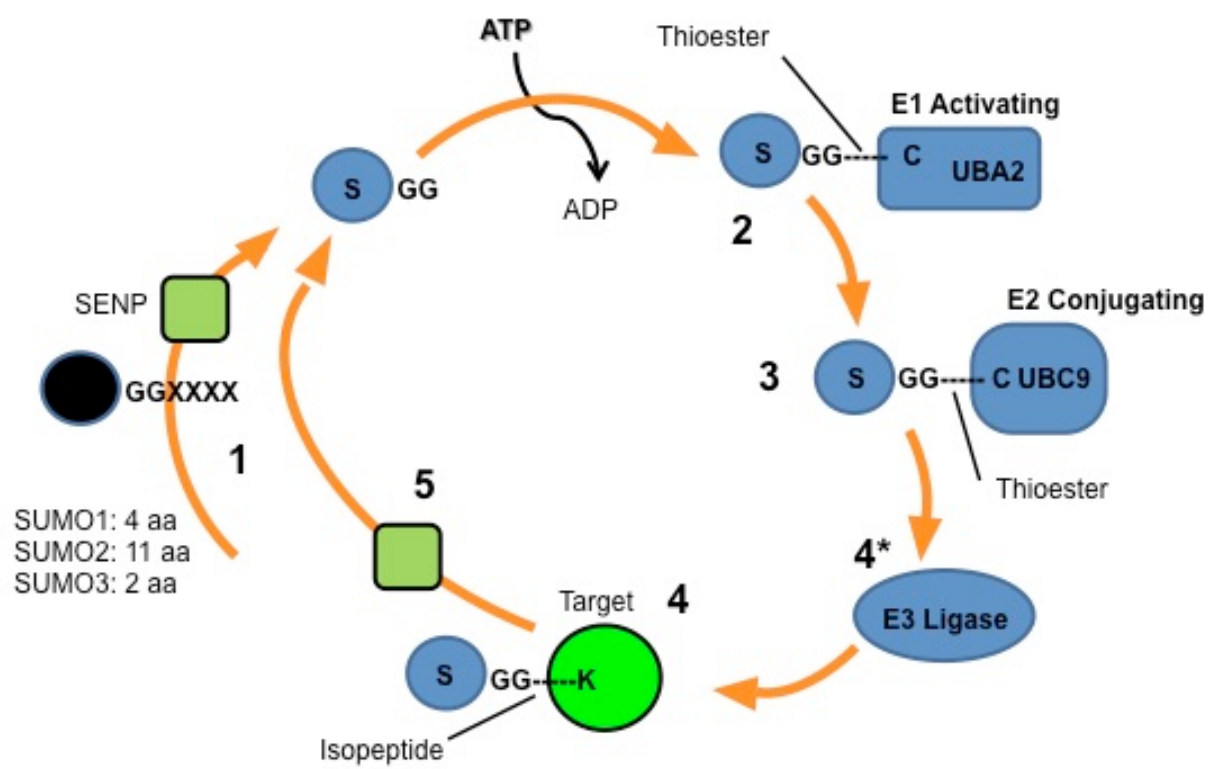
involved in cristae remodeling, which facilitates sharing of crucial mitochondrial factors and DNA (297). Mitochondrial fusion is a vital process involved in regulation of cellular metabolism and assists in repair and degradation of damaged or dysfunctional mitochondria during mitophagy (136, 137, 197, 292).

The converse process is mitochondrial fission (**Figure 24**), in which these branched networks are separated into the organelle form. Fission is primarily catalyzed by the GTPase dynamin-related protein 1 (**Drp1**), which affects both the size and distribution of the organelle forms. Drp1 is recruited to the surface of mitochondria by several OMM integral membrane protein receptors, as follows. Mitochondrial fission protein 1 (**Fis1**) and mitochondrial fission factor (**Mff**) independently recruit Drp1 to the OMM and are proposed to mediate oligomerization of Drp1 at fission sites forming scission rings (156). Recent observations have led to identification of two additional proteins, the 49- and 51- kDa mitochondrial dynamics proteins **MiD49** and **MiD51**, respectively, that appear to promote fission by recruiting Drp1 to the OMM even in the absence of Fis1 and Mff (155, 190). Once recruited to fused mitochondrial networks, Drp1 oligomerizes into spiral structures that pinch mitochondria apart via a GTP-dependent scission function similar to the scission seen with endocytic vesicle formation (119, 155). This vital cellular process is tightly regulated through the use of post-translational modifications (**PTMs**) including **SUMOylation**, phosphorylation, ubiquitination and *N*-nitrosylation (42). Additionally, there are splice variants of Drp1 whose array of functions and roles in mitochondrial dynamics are not yet fully understood (265).

Since our preliminary data suggested a role for RdRp SUMOylation in the NoV replicative cycle (see below), we focused on the role of Drp1 SUMOylation in mitochondrial dynamics as a possible target of RdRp-mediated morphological rearrangement during RC formation. SUMOylation of Drp1 induces mitochondrial fission in a variety of mammalian cell types (231). SUMOylation is a reversible PTM in which a small ubiquitin-like modifier (**SUMO**) protein is conjugated to a protein substrate at a lysine residue. SUMOylation has been described to occur at a SUMO consensus site, **Ψ-K-X-E** (where 'Ψ' is a hydrophobic amino acid and 'X' is any amino acid), or at nonconsensus SUMO sites on the target protein. However, mutagenesis studies of Drp1 (among other proteins) indicate that SUMOylation can also occur on lysine residues not associated with identified SUMO consensus sites (72). The effects of SUMOylation are manifold and vary depending on the target protein, but SUMO can modulate a target protein's subcellular localization and often serves as a mediator of protein-protein interactions, including oligomerization (90, 163).

There are three SUMO paralogues in eukaryotic cells, with SUMO2 and SUMO3 differing by three N-terminal amino acids (commonly referred to as **SUMO2/3**) and both being 50% identical to SUMO1. The SUMO proteins are conjugated to targets at one or more acceptor lysine residues with an isopeptide bond via a reaction cascade (**Figure 25**) involving a heterodimeric E1 activating enzyme (**SAE1/UBA2**), an E2 conjugating enzyme (**Ubc9**), and several different E3 ligases (90). In mammalian cells there are six SUMO-specific isopeptidases (**SEN1-3** and **SEN5-7**) that deconjugate SUMO proteins from substrates (289).

Figure 25: General schematic of reversible SUMO modification. **1)** Nascent SUMO must be proteolytically processed by SUMO-specific proteases to reveal a C-terminal di-glycine motif, yielding mature SUMO. Ulp/SENp proteases will remove 4 C-terminal amino acids from SUMO1, 11 from SUMO2 and 2 from SUMO3. **2)** Heterodimeric E1 activating enzyme SAE1/UBA2 activates mature SUMO by forming a thioester link with the C-terminal Gly on SUMO and residue C173 on UBA2 in an ATP-dependent reaction. **3)** SUMO is transferred to a catalytic Cys residue on Ubc9, the E2 conjugating enzyme. UBC9-SUMO finds and recognizes a SUMO-acceptor site on a target protein. **4)** Mature SUMO is transferred to the target protein and conjugated to the Lys residue on the acceptor site. **4*)** An E3 ligase catalyzes this transfer by forming an isopeptide bond between the C-terminal Gly of SUMO and a Lys side chain on the target. *This step can also occur in the absence of an E3 ligase. SUMO exerts its effect on the target protein. **5)** DeSUMOylation of the target protein is catalyzed by SUMO proteases. Reviewed by Geiss-Friedlander and Melchior (2007) (90).



The abundance of SUMOylated mitochondrial proteins and the discovery of an OMM-bound E3 SUMO ligase named mitochondrial-associated protein ligase (**MAPL**) has unveiled conjugation to SUMO as an important regulatory mechanism in mitochondrial proteins (231). MAPL has a RING-finger domain that has SUMO E3 ligase activity and is able to SUMOylate cytoplasmic substrates and substrates associated with the OMM (34, 176). MAPL is the first SUMO E3 ligase reported to target Drp1 and Drp1 is its major substrate. MAPL conjugates SUMO1 to Drp1, inducing translocation of SUMOylated Drp1 to the OMM, where it presumably binds to Drp1 receptors (Fis1, Mff, MiD49 and MiD51) to induce fission (34). Drp1 is SUMOylated at multiple lysine residues by all three SUMO isoforms with SUMO2/3 modification primarily occurring during oxidative stress (72). The stable association of assembled Drp1 on the mitochondria is reversed by SUMO deconjugation by cytoplasmic SENP5 (298). Once deconjugated, Drp1 dissociates from the OMM and returns to the cytoplasm until further signaling occurs.

In **Chapter 2** we showed the NoV RdRp, NA, is an integral membrane protein that establishes RCs on the OMM and induces mitochondrial clustering that parallels the clustered morphology observed in systems with disrupted Drp1 activity (84, 239, 240). In this chapter we describe our further studies to understand the mechanism by which RC formation occurs. Our preliminary observation that NA could be SUMOylated *in vitro* led us to hypothesize that NA pushes the equilibrium of mitochondrial dynamics toward the fused mitochondrial morphology by interfering with SUMOylation of Drp1 and disrupting Drp1 association with mitochondria. In this study, we tested the hypothesis that NA acts as an antagonist of mitochondrial fission by outcompeting Drp1 for

SUMOylation using immunofluorescence confocal microscopy and biochemical recruitment assays. Our results show that NA is a target for SUMOylation and inhibits translocation of Drp1, leading to increased levels of cytoplasmic Drp1 and reduced amounts of OMM-associated Drp1. This leads to disruption of mitochondrial dynamics. These results are the first steps into understanding the cellular mechanisms of NoV RNA replication complex formation in mammalian cells.

3.2 Materials And Methods

Cells, virus stocks and tissue culture. All recombinant plasmids were amplified in *Escherichia coli* strain NEB10 β (New England Biolabs) as performed in **Chapter 2** (10). BSR-T7/5 cells (39) were grown at 37°C. The full-length N1 cDNA clone of *Nodamura virus* (Family *Nodaviridae*, genus *Alphanodavirus*, species *Nodamura virus*) was derived from the Mag-115 strain, as described previously (124). Its GenBank ID is AF174533.

For protein assays, BSR-T7/5 cells were seeded into 10 cm dishes at a density of 2×10^6 cells/dish and allowed to grow until confluent. These cells were transfected with 10 μ g of the appropriate pNoV1(0,0)-based plasmid using Lipofectamine 2000 and serum-free Opti-MEM (Invitrogen, Carlsbad, CA), as described (124). Cells were incubated with DNA-liposome complexes for 4 hours at 37°C, supplemented with complete growth media and the incubation was continued for 20 hours prior to harvest. For immunofluorescence microscopy experiments, cells were seeded into 6-well plates (10 cm² wells) at a density of 5×10^5 cells/well and allowed to grow until confluent. These cells were transfected with 2 μ g of plasmid, incubated for 4 hours at 37°C,

harvested by trypsinization, diluted 1:100 in complete growth media, transferred to 8-chamber slides, and continued incubation for 20 hours prior to staining.

Plasmid constructions. The plasmid pT7-N1-HA was previously constructed and described in **Chapter 2** and reference (84). The SUMO1-accepting lysine residues within the predicted consensus SUMOylation sites on the NoV RdRp (K523, K655, and K723) were mutated to alanine either singly, pairwise, or all three together by PCR-based mutagenesis followed by *DpnI* selection as described (218). The fragments of DNA containing the mutations were introduced back into parental pT7-N1-HA resulting in plasmids pT7-N1_{K523A}-HA, pT7-N1_{K655A}-HA, pT7-N1_{K723A}-HA, pT7-N1_{K523/655A}-HA, pT7-N1_{K523/723A}-HA, pT7-N1_{K655/723A}-HA and pT7-N1_{K523/655/723A}-HA (pT7-N1_{K-A}-HA, expresses NA_{K-A}). The final reconstructed plasmids were confirmed by DNA sequencing.

Bioinformatic tools for analysis of SUMO consensus motifs and SUMO interacting motifs (SIMs). The SUMOplot (www.abgent.com/doc/sumoplot) and SUMOsp (210, 287) servers were used to predict the location of several consensus SUMOylation motifs within the NA sequence (K523, K655, K723 and K529). To determine whether the SUMO consensus motifs are conserved among the family *Nodaviridae* protein A sequences, multiple sequence alignment was performed using ClustalW with default settings (146, 260). The NoV RdRp was evaluated for the presence of active SIM candidates using a previously described bioinformatics pipeline protocol (276) with modifications. The PATTINPROT server (52) was used to search the FASTA-formatted primary structure of NA for the following SIM core binding site pattern values (122): [IVL]-[IVL]-X-[IVL], [IVL]-X-[IVL]-[IVL], [IVL]-[IVL]-[IVL]-X and [IVL]-[IVL]-

[IVL]-[IVL]. The following modified SIM consensus patterns (170) were also searched in the NoV RdRp using PATTINPROT: [PILVM]-[ILVM]-X-[ILVM]-[DSE], [PILVM]-[ILVM]-[DE]-[IVLAM], and [DSE]-[ILVM]-X-[ILVMF](2). The PATTINPROT server predicted 11 SIMs that were analyzed further using additional bioinformatics tools. The PFAM server (74) was used to predict the functional domains on the RdRp. The globularity/disordered status of the NoV RdRp was predicted using GlobPlot 2 (151) and IUPRED (65, 66) servers. Predicted SIMs that lie within structured functional domains were flagged for low SIM potential. The residues VLRV (aa 953-956) on NA were the only predicted SIM core binding site to meet the pipeline criteria for functional SIM candidacy.

Immunofluorescence confocal microscopy. Immunofluorescence confocal microscopy was performed as previously described in **Chapter 2** (84), with the following modifications. Cells were fixed in 4% paraformaldehyde for 20 min at 37°C, permeabilized with 0.1% Triton X-100 in PBS (PBS-T) for 10 min at room temperature, and blocked in PBS-T supplemented with 1% BSA. Primary antibodies were incubated overnight at 4°C in this blocking buffer. Secondary antibodies were incubated for 1 hour at room temperature in PBS-T.

Antigens were detected within blocked BSR-T7/5 cells with primary antibodies specific for either the hemagglutinin epitope tag (as described in **Chapter 2**), dynamin-related protein 1 (Drp1; rabbit polyclonal IgG, Santa Cruz Biotechnology), or for SUMO1 (mouse monoclonal IgG₃, Santa Cruz Biotechnology). Binding of primary antibodies to their respective antigens was detected using FITC-labeled goat anti-mouse IgG, FITC-labeled goat anti-rabbit IgG, TR-labeled goat anti-mouse IgG, or TR-labeled goat anti-rabbit IgG. Specific combinations of primary antibodies and fluorescently labeled

secondary antibodies are indicated in the text. All secondary antibodies used for immunofluorescence were purchased from Santa Cruz Biotechnology (Santa Cruz, CA). High-resolution digital fluorescent images were captured using a Zeiss LSM 700 confocal microscope and ZEN 2009 software as previously described in **Chapter 2** (84).

Immunoprecipitation. At 24 hours post-transfection, BSR-T7/5 cells were washed in ice-cold PBS and scraped into cold PBS. Equal amounts of cells per sample were harvested by centrifugation. Cell pellets were resuspended in lysis buffer supplemented with 20 mM NEM, 1mM benzamidine and 1 mM PMSF. Lysate was rotated 30 min at 4°C then clarified by centrifugation at 14,000 x *g* for 20 min at 4°C. Clarified lysate was rotated at 4°C for 2 hours with 2 µg of either mouse anti-SUMO1 monoclonal antibody, rabbit anti-Drp1 polyclonal antibody, or rabbit anti-HA polyclonal antibody. Samples were given either goat anti-mouse or goat anti-rabbit MagnaBind™ IgG beads (Thermo Scientific) and were rotated at 4°C for 1 hour. Specifically bound proteins were magnetically precipitated, washed and resolved by SDS-PAGE. Proteins were analyzed by Western blotting as described below.

***In vitro* SUMOylation reactions.** The *in vitro* SUMOylation reactions were performed as previously described (189). The NoV RdRp was synthesized from non-replicating expression plasmid pTM-NA in the presence of [³⁵S]-methionine in a coupled transcription/translation reaction (Promega). A sample of the radiolabeled protein was incubated in a reaction mixture containing purified protein components of the SUMOylation system (1 µg SUMO E1 enzyme, 280 ng SUMO E2 enzyme, and 1.5 µg His-SUMO1) and 1X SUMOylation buffer (50 mM Tris-Cl pH 8.0, 5 mM MgCl₂, 5 mM ATP, and 0.5 mM DTT) for 1.5 hours at 37°C. A set of negative control reactions was

incubated without the purified SUMO protein components. Another set of control reactions containing the purified SUMO components received the purified catalytic domain of the yeast SUMO protease Ulp1 (Ulp1₄₀₃₋₆₂₁) 30 min after the reactions began. The reactions were stopped by addition of 4X sample buffer (50 mM Tris pH 6.8, 10% glycerol, 4% SDS, 0.01% bromophenol blue, 2% 2-mercaptoethanol) and boiled for 3 min. The samples were resolved by SDS-PAGE as described below. Proteins were subsequently transferred to polyvinylidene fluoride (PVDF) membranes (ImmobilonTM-P; Millipore) as described below. The membranes were dried and developed by autoradiography. A similar protocol will be used for the proposed *in vitro* MAPL assays except that MAPL will be added to the reaction (or words to that effect).

SDS-PAGE and Western blot analysis. All protein samples to be analyzed by SDS-PAGE were prepared and resolved on 6% or 10% gels, as indicated in the figure legends. Western blot analysis was performed as previously described in **Chapter 2** (84) with the following modifications. Membranes were washed in Tris-buffered saline (TBS) containing 0.25% Tween-20 (TBS-T) and blocked with TBS-T containing 1% BSA. Primary antibodies were diluted to their indicated dilutions in blocking buffer and incubated on blots either at room temperature for 1 hour or at 4°C overnight. Blots were subsequently incubated with the corresponding secondary antibody for 30 min at room temperature. Blots were developed using AmershamTM ECLTM Prime Western blot Detection Reagent (GE Healthcare Life Sciences). Developed films were photographed with a Gel Doc XR Molecular Imager running Quantity One 1-D Analysis Software (Bio-Rad) to generate the digital images shown.

The following primary and secondary antibodies were used in this study at the indicated dilutions: mouse anti-HA monoclonal antibody (Santa Cruz Biotechnology) at 1:1000; rabbit anti-HA polyclonal antibody (Santa Cruz Biotechnology) at 1:500; rabbit anti-Drp1 polyclonal antibody (Santa Cruz Biotechnology) at 1:500; mouse anti-SUMO1 monoclonal antibody (Santa Cruz Biotechnology) at 1:1000; goat anti-mouse and goat anti-rabbit polyclonal HRP-conjugated antibodies (Santa Cruz Biotechnology) at 1:5000.

3.3 Results

The NoV RdRp is a target for SUMOylation *in vitro*. Based on our previous results, we hypothesize that the mitochondrial morphology induced by infecting cells with NoV (**Figure 2**), or by simply expressing N1 and RdRp in cells (**Figure 16**) represent a shift in mitochondrial dynamics toward the clustered form (84). Mitochondrial dynamics are also altered by Drp1 SUMOylation, which induces fission as noted above. The presence of consensus SUMOylation motifs within the NoV RdRp led us to hypothesize that the NoV RdRp induces mitochondrial clustering by altering Drp1 SUMOylation, perhaps by outcompeting Drp1 for access to the SUMOylation machinery, leading to inhibition of Drp1-induced mitochondrial fission.

Software prediction programs SUMOplot (abgent.com/doc/sumoplot) and SUMOsp (287) were used to predict the location of several consensus SUMOylation motifs within the NA sequence and multiple sequence alignment was used to determine whether the motifs were conserved in the protein A sequences for other alpha- and betanodaviruses. The prediction software confirmed the presence of the consensus SUMOylation motif at residues 722-725 (**LKIE**) and this motif is conserved among all

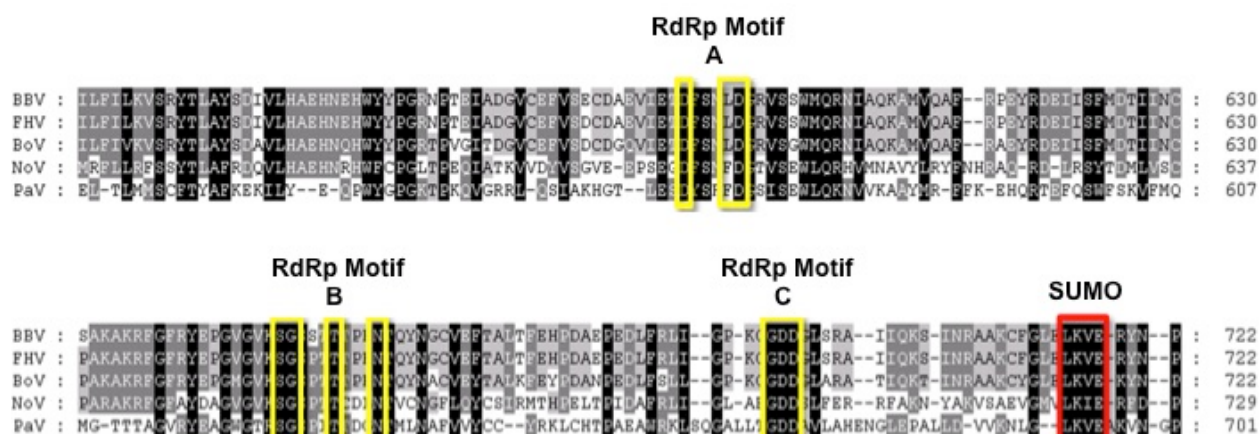


Figure 26: Predicted SUMO site conserved among alphanodaviruses. Sequence alignment of the five alphanodavirus protein A sequences (*Black beetle virus*, BBV; *Flock House virus*, FHV; *Boolarra virus*, BoV; *Nodamura virus*, NoV; *Pariacoto virus*, PaV). Boxed in yellow are the RdRp motifs and boxed in red is the consensus SUMOylation site (LKIE for NoV) conserved in all five alphanodaviruses. Protein A sequence alignment was performed by Ana Betancourt and predictions performed by Dr. K. L. Johnson.

alphanodaviruses (**Figure 26**, red box). Additional consensus SUMOylation motifs were predicted on NA with the acceptor lysine residues at positions K523 and K655. These results suggest there is potential for the NoV RdRp to be a target for SUMO modification. The sites must be accessible to the SUMO cascade enzymes for modification to occur. In **Chapter 2**, we showed the NoV RdRp is associated with the OMM yet exposed to the cytoplasm, which increases the likelihood for NA to be SUMOylated on exposed lysine residues.

To determine whether the NoV RdRp can be covalently SUMOylated, NA protein was synthesized in a coupled *in vitro* transcription-translation reaction in the presence of [³⁵S]-methionine and used as a substrate in an *in vitro* SUMOylation assay, as previously described (189). The labeled protein was incubated in reactions containing purified proteins of the SUMO1 pathway, specifically SUMO1, E1 activating enzyme (Sae1/2) and a SUMO-specific protease (Ulp1). A parallel set of positive control reactions was incubated using radiolabeled, *in vitro* synthesized C/EBP β , which is a transcription factor and documented SUMO target. The reactions were resolved by SDS-PAGE and the proteins were imaged by autoradiography (**Figure 27**).

Proteins incubated in reactions that include Ulp1 and lack the E1 enzyme were unable to undergo SUMO-specific modification and serve as a negative control (**Figure 27A and B**, lane 1). When NA was reacted with the E1 enzyme, a new protein species was detected whose migration is consistent with SUMOylated NA (**Figure 27A**, lane 2, arrow). The new protein species was not detected when the reaction was incubated with Ulp1 (**Figure 27A**, lane 3), suggesting the indicated protein species in lane 2 is SUMOylated NA. These results corroborate the SUMO predictions and indicate that the

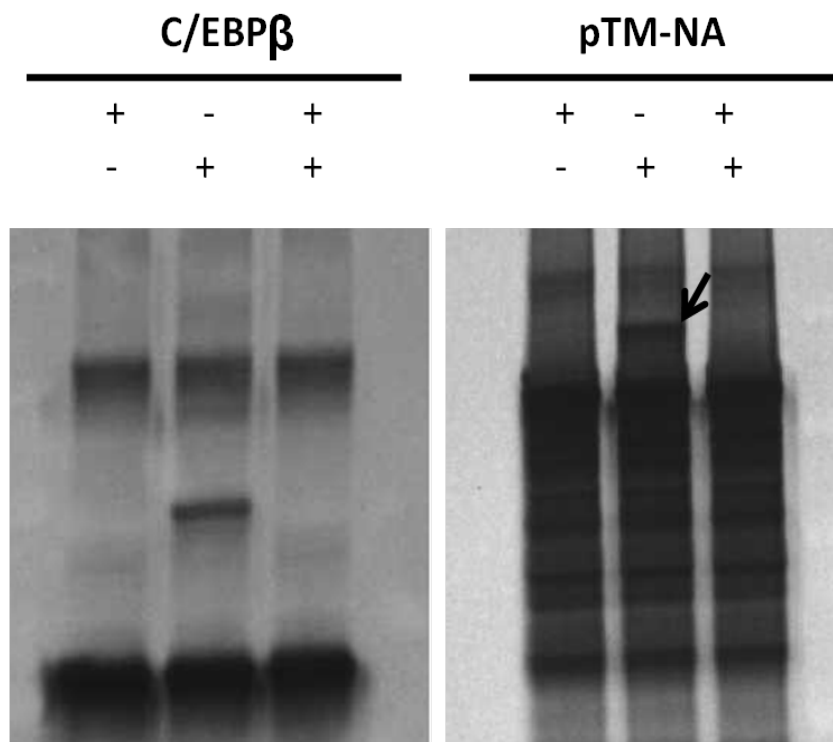


Figure 27: NoV protein A is SUMOylated *in vitro*. NA was synthesized in a coupled *in vitro* transcription/translation assay using [35 S]-methionine in the presence or absence of SUMO conjugating enzyme or the deSUMOylating enzyme, **Ulp1**. Proteins were resolved by SDS-PAGE and imaged by autoradiography. The cellular protein C/EBP β serves as a positive control for SUMOylation. Synthesis in the presence the conjugating enzyme (**Sae1/Sae2**) results in SUMOylation of a potential target. As a control, samples were synthesized in the presence of Ulp1 (third lane) to show any new protein species detected in SUMO reactions (second lane) are products of SUMOylation. Arrow, SUMOylated NA. This experiment was performed as previously described (188).

NoV RdRp serves as a target for *in vitro* SUMOylation. However it remained to be determined whether the NoV RdRp can be SUMOylated in cultured mammalian cells.

The NoV RdRp interacts with SUMO1 in mammalian cells. As a next step in testing our hypothesis, we asked whether NA could serve as a substrate for SUMOylation in cultured mammalian cells. In order to do that, we overexpressed the SUMO machinery in BSR-T7/5 cells from dicistronic plasmids, as previously described (188), to increase levels of cellular SUMOylation and thereby increase the detectability of SUMO-conjugated NA. Typically, the SUMOylated species of a protein represents a fraction (often less than 5%) of that protein's total population in the cell with exceptions such as RanGap1, for which the SUMOylated 90 kDa form is the most prominent species (163, 288). The presence of active de-SUMOylating proteases in cells poses an additional barrier to detect SUMOylated forms of target proteins (288). Therefore, the use of expression plasmids may help compensate for difficulties detecting sparse populations of a target protein SUMOylated by the endogenous SUMO machinery (188).

The original form of the dual S1/I/U plasmid expresses N-terminally His-tagged and S-peptide-tagged SUMO1 and N-terminally HA-tagged Ubc9 with an EMCV IRES separating the cistrons, all under the transcriptional control of an RNA polymerase II promoter. Dual S1(Q94P-T95R)/I/U expresses a SUMO1 and Ubc9 dicistronically like Dual S1/I/U, but instead expresses a SUMO1 mutant with the following mutations: Q94P to confer resistance to deconjugation by cellular SENPs; and T95R adds a trypsin cleavage on the C-terminus of SUMO1 before the diglycine motif. This mutation was originally designed to allow detection of small exogenous SUMO1 isopeptide bond

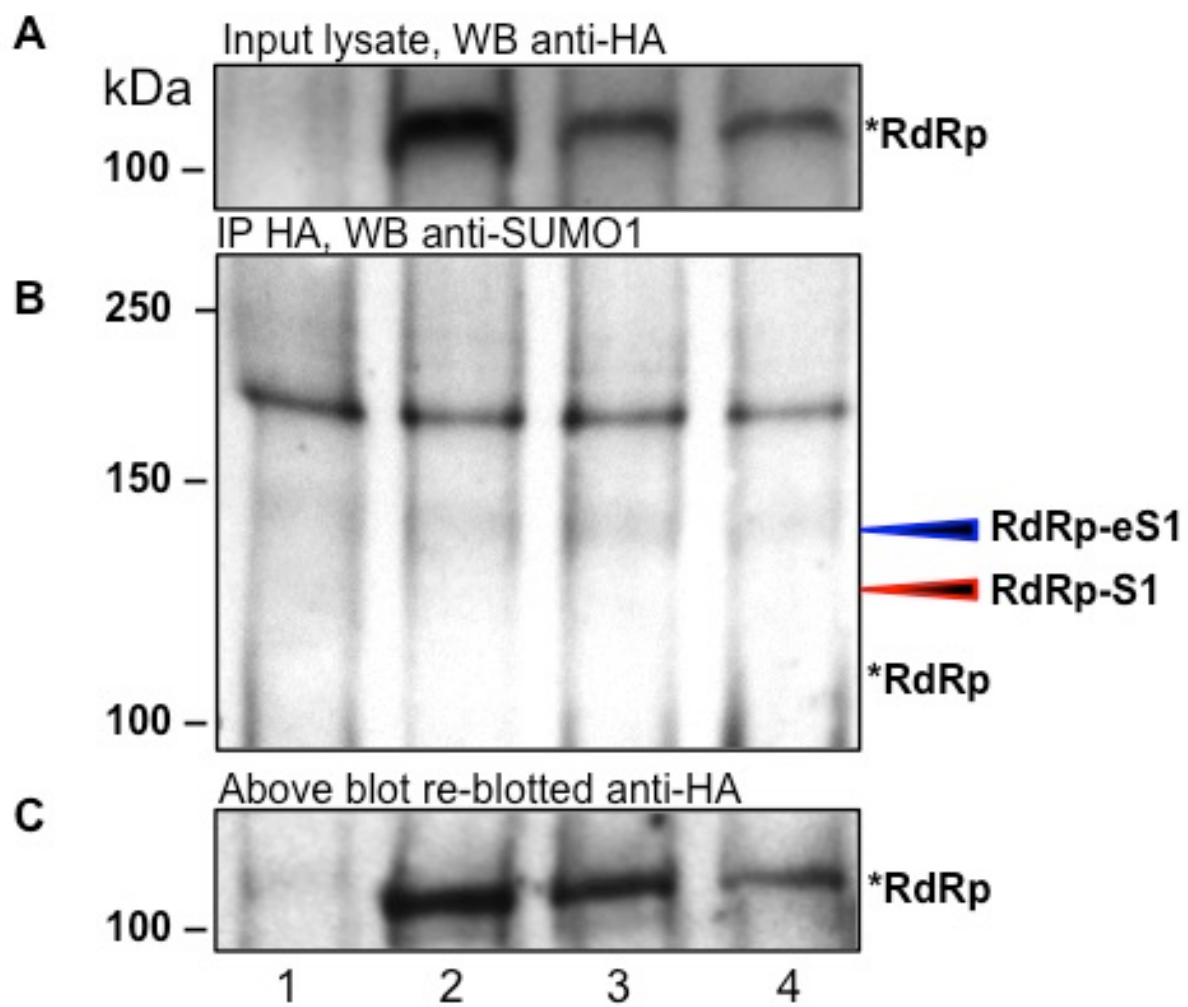
signatures on SUMOylated proteins using tandem tag affinity purification followed by mass spectrometry. The parental plasmid directs transcription in the nucleus, where the expressed proteins catalyze SUMOylation of target proteins.

NoV replicates in the cytoplasm so we found it preferable to also express the Dual S1/IU and Dual S1(Q94P-T95R)/IU cassettes in the cytoplasm. We cloned the cassettes from the Dual plasmids into the pT7Ri mammalian expression vector, which is the T7 transcription plasmid TVT7R(0,0) (126) with a small fragment of PhiX174 DNA introduced into the MCS to facilitate ease of cloning (Johnson and Ball, unpublished data). The resulting plasmids, pT7R-S/IU and pT7R-S1(Q94P-T95R)/IU, were confirmed by DNA sequencing for the presence of an intact T7 promoter and the insertion of the cassette. Using these vectors, we can overexpress NA and the SUMO1 components in the cytoplasm under T7 transcriptional control, thereby avoiding potential pitfalls from nuclear synthesis and retention as well as kinetics and timing of expression.

Having established the system for SUMO overexpression in BSR-T7/5 cells, we combined it with a co-immunoprecipitation (**co-IP**) assay to determine whether NA could be SUMOylated in cultured mammalian cells. BSR-T7/5 cells were co-transfected with pT7-N1-HA and the dicistronic T7 plasmids. After 24 hours at 37°C, the cells were lysed and processed for immunoprecipitation using mouse anti-HA monoclonal antibodies as described in this chapter's Materials and Methods section (**3.2**). Immunoprecipitates were resolved by SDS-PAGE and analyzed by Western blot to detect SUMO1-conjugated NA, using mouse anti-SUMO1 monoclonal primary antibodies (**Figure 28**).

NA was detected in the starting (input) lysate before co-IP was performed (**Figure 28A**, lanes 2-4). However, SUMO1-conjugated NA species were not detected in

Figure 28: SUMOylated NA species were not detected after immunoprecipitation from cultured mammalian cells. Cells were transfected with plasmids expressing the NoV RdRp, SUMO1 and Ubc9. After 24 hrs, cells were lysed and processed for NA-HA immunoprecipitation as described in this chapter's Materials and Methods section (3.2). (A) Equal protein amounts of input lysate from each sample and (B) immunoprecipitates were resolved on 7.5% SDS-PAGE gels, transferred to PVDF membranes, and analyzed by Western blot for the presence of HA-tagged NA. Lanes: **1)** mock, **2)** pT7R-S1/I/U, **3)** pT7R-S1(Q94P-T95R)/I/U, **4)** pT7R-NoV1-HA, **5)** pT7R-NoV1-HA + pT7R-S1/I/U, **6)** pT7R-NoV1-HA + pT7R-S1(Q94P-T95R)/I/U. The expected molecular weights of NA are indicated on the right: unmodified NA, ***RdRp**; NA modified by endogenous SUMO1, **RdRp-S1**; NA modified by exogenously expressed SUMO1, **RdRp-eS1**. (C) The blot from (B) was stripped and re-blotted against HA-tagged NA.

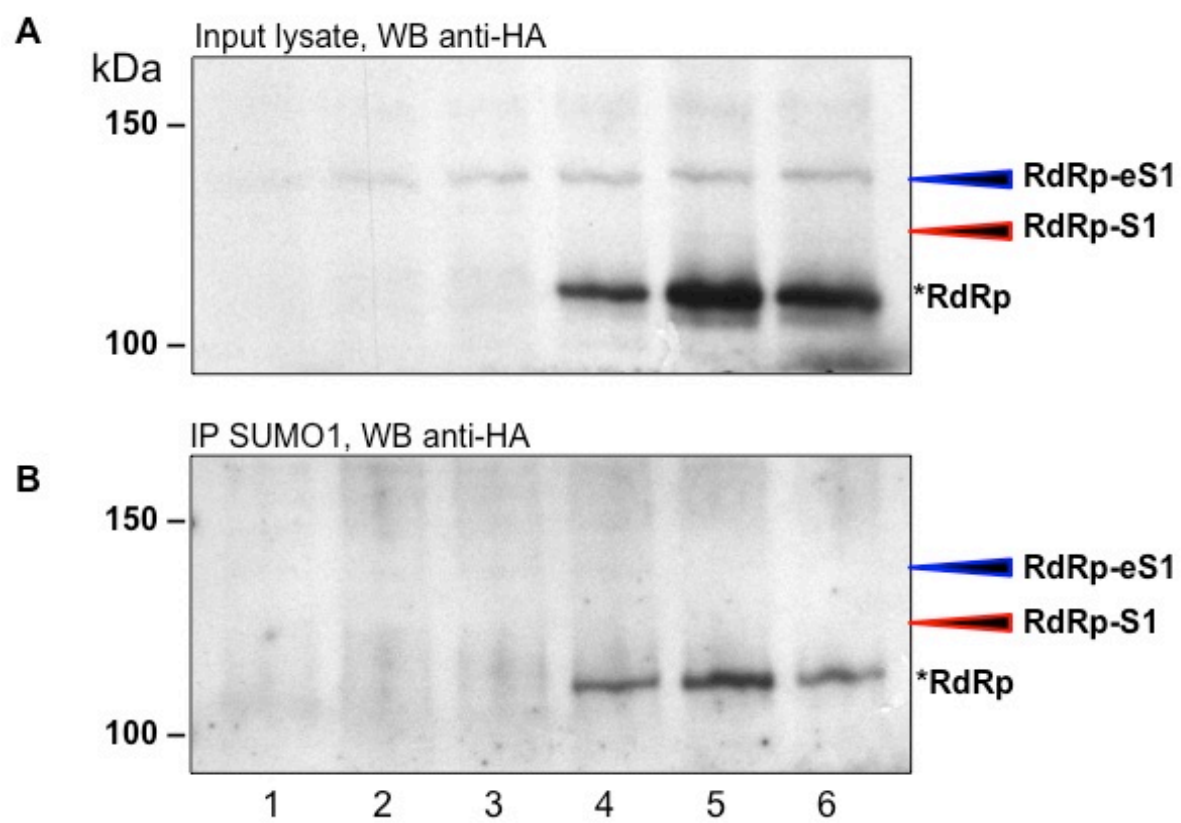


the co-IP samples at the molecular masses predicted for covalent modification with endogenous or exogenous SUMO1 (**Figure 28B**, arrows). To ensure NA that was pulled down during the co-IP protocol, the blot in **figure 28B** was stripped and reblotted to detect NA (**Figure 28C**). NA that migrates as predicted for the unmodified protein was detected in the re-probed exposure, suggesting that the immunoprecipitation of the NoV RdRp was successful (**Figure 28C**, lanes 2-4). Although we were unable to detect SUMO1 conjugated NA, our *in vitro* SUMOylation assay suggests NA can be SUMOylated. Detection of SUMOylated species of a protein can often be difficult due to the low abundance of the conjugated species, as experienced by our colleagues studying SUMOylation of lens epithelium-derived growth factor/p75 (**LEDGF/p75**) (40). From their experience and personal communications with our collaborator, we noted that there are a number of technical factors that can affect detection of a SUMO-conjugated protein, including sample size and the detection limits of the methods used.

To confirm our interpretation of the previous co-IP results, we performed the co-IP experiment from **figure 28** in the reverse order (IP: SUMO1 and WB: NA). BSR-T7/5 cells were co-transfected with pT7-N1-HA and the dicistronic T7 plasmids as in **figure 28**. After 24 hours at 37°C, the cells were lysed and processed for co-IP using mouse anti-SUMO1 monoclonal antibodies as described in this chapter's Materials and Methods section (**3.2**). Immunoprecipitates were resolved by SDS-PAGE and analyzed by Western blot to detect SUMO1-conjugated NA using mouse anti-HA monoclonal primary antibodies (**Figure 29**).

In the samples where the NoV RdRp is expressed, NA is observed to co-IP with SUMO1 and is readily detectable by Western blot (**Figure 29B**, lanes 4-6). Interestingly,

Figure 29: The NoV RdRp co-immunoprecipitates with SUMO1. Cells were transfected as described in the legend to **Figure 28**. After 24 hrs, cells were lysed and processed for SUMO1 immunoprecipitation as described in this chapter's Materials and Methods section (**3.2**). **(A)** Equal protein amounts of input lysate from each sample and **(B)** immunoprecipitates were resolved on 7.5% SDS-PAGE gels, transferred to PVDF membranes, and analyzed by Western blot for the presence of HA-tagged NA. Lanes: **1)** mock, **2)** pT7R-S1/I/U, **3)** pT7R-S1(Q94P-T95R)/I/U, **4)** pT7R-NoV1-HA, **5)** pT7R-NoV1-HA + pT7R-S1/I/U, **6)** pT7R-NoV1-HA + pT7R-S1(Q94P-T95R)/I/U. The expected molecular weights of NA are indicated on the right: unmodified NA, ***RdRp**; NA modified by endogenous SUMO1, **RdRp-S1**; NA modified by exogenously expressed SUMO1, **RdRp-eS1**.



there were no apparent differences in the amount of NA that co-immunoprecipitated with SUMO1 when the SUMO machinery was overexpressed or when SUMO1-Q94P-T95R was expressed (**Figure 29B**, compare lanes 5 & 6 with lane 4). This suggests that NA interacts abundantly with endogenous levels of SUMO1 under normal SUMOylation cascade kinetics. This was a useful finding because the effects of overexpressing the SUMO machinery are unpredictable in our model system and we may now choose to leave these samples out in the future. Additionally, there were no observable higher MW species of NA that would be consistent with covalently SUMOylated forms of NA; instead the MW of NA that co-immunoprecipitated with the anti-SUMO1 antibody was consistent with the unmodified form of NA. Nevertheless, despite the lack of observable higher MW NA species, these results suggest that the NoV RdRp stably interacts with endogenous SUMO1 in some way. If NA is covalently SUMOylated, we hypothesize that one or more of the predicted consensus SUMO sites may be involved in this process.

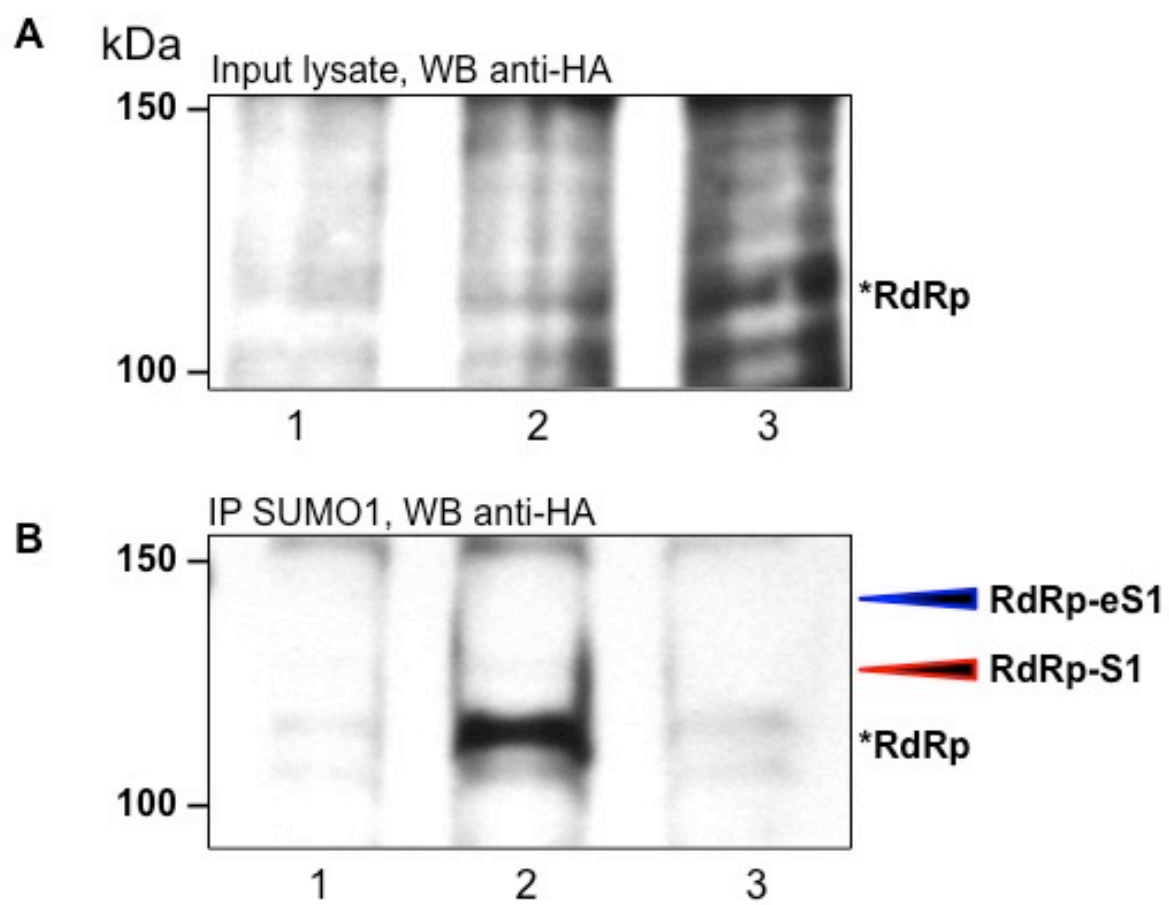
Mutating the lysine residues in the predicted SUMO consensus sites on the NoV RdRp disrupts its interaction with SUMO1 in transfected mammalian cells. To further investigate whether NA is covalently SUMOylated and to characterize the potential role of SUMO1 in NoV RC formation, we mutated the predicted SUMO consensus sites in the NA ORF to exchange the most likely acceptor lysine residues to alanine. As mentioned above, three lysine residues were found to occur in consensus SUMO sites, although only one (K723) was conserved among all the alphanodaviruses. We used circular PCR-based site directed mutagenesis followed by Dpn1 selection to introduce all three of the K-to-A mutations, K523A, K655A, and K723A, into NA to

prevent its SUMOylation at these sites. The parental vector used for this mutagenesis was pT7-N1-HA, and the resulting reconstructed clone pT7-N1_{K-A}-HA was confirmed by DNA sequencing.

BSR-T7/5 cells were transfected either with WT pT7-N1-HA or the mutated form pT7-N1_{K-A}-HA. Following 24 h incubation at 37°C, cells were lysed and SUMO1 conjugates were immunoprecipitated using mouse anti-SUMO1 antibodies as before. The immunoprecipitates were examined by Western blot as described above, using mouse anti-HA antibodies to detect NA. As shown in our previous co-IP experiment, WT NA co-IPs with SUMO1 (**Figure 30B**, lane 2), but when all three of the predicted SUMO acceptor lysine residues are mutated to alanine, the interaction between SUMO1 and NA is lost (**Figure 30B**, lane 3). These results suggest that the predicted SUMO consensus sites on NA are involved in this interaction, potentially serving as sites for SUMOylation, albeit below the detection limits of our current assay. The NA_{K-A} mutant phenotype shows a significant difference from the WT and we will therefore test the individual and double K-to-A NA mutant variants to determine which lysine residues are involved this interaction. The significance of these results will be considered further in the Conclusions section (3.5) of this chapter.

Our results so far do not reveal whether or not NA is covalently SUMOylated in mammalian cells, particularly since the molecular mass of NA in these three experiments (**Figures 28C, 29B, and 30B**) corresponds to that of unmodified HA-tagged NA (115 kDa). While these results do not rule out the possibility that NA is covalently SUMOylated, such modification might occur at levels below the detection limits of our co-IP and Western blot assay. We propose to use a more sensitive

Figure 30: Mutating the three predicted SUMO consensus motifs abolishes the interaction between NA and SUMO1 in mammalian cells. Cells were transfected and processed for SUMO1 immunoprecipitation as described in the legends to **Figures 28 and 29**. **A)** Equal protein amounts of input lysate from each sample and **B)** immunoprecipitates were resolved on 7.5% SDS-PAGE gels, transferred to PVDF membranes, and analyzed by Western blot for the presence of HA-tagged NA. Lanes: **1)** mock, **2)** pT7R-NoV1-HA, and **3)** pT7-N1_{K-A}-HA. The expected molecular weights of NA are indicated on the right: unmodified NA, ***RdRp**; NA modified by endogenous SUMO1, **RdRp-S1**; NA modified by exogenously expressed SUMO1, **RdRp-eS1**.



approach to determine definitively whether NA is SUMO1-conjugated in mammalian cells. This will involve expression of triple-epitope-tagged NA in cells co-expressing the SUMO1 Q94P-T95R mutant, purifying NA from cells, and analyzing the resulting protein for SUMO conjugation using mass spectrometry. This method will also allow unambiguous determination of which specific lysine residues might be SUMOylated. However, these future experiments are beyond the scope of this doctoral dissertation and will not be considered further here.

However, the data are nevertheless clear that NA and SUMO1 are interacting in mammalian cells, which is unlikely to have been genetically conserved in the absence of some role for this interaction in the NoV life cycle. The results of our co-IP experiments that pull down SUMO1 in the presence of WT or NA_{K-A} support the possibility of NA SUMOylation (**Figures 29 and 30**). The lack of observable higher MW NA-SUMO1 conjugates might be explained by the apparent ability of the NoV RdRp to undergo homo-oligomerization during RC formation, as evidenced in preliminary non-denaturing PAGE experiments (Gant and Johnson, **data not shown**). The RdRps of other positive-strand RNA viruses (poliovirus and hepatitis C virus) RdRps (3D^{pol} and NSP4, respectively) oligomerize into super molecular weight complexes that may also contain host proteins (108, 193, 279). SUMOylation affects various aspects of many viral processes in the cell (71) and may possibly play a role in oligomerization of NA. If NA indeed forms similar membrane-bound super molecular weight complexes, it is possible that only a small portion of NA may be covalently SUMOylated (perhaps due to lack of accessibility to the SUMOylation cascade machinery). When these super molecular weight complexes are pulled down by the small proportion of SUMO1-

conjugated NA, the majority of NA detected by Western blot after boiling in SDS-containing sample buffer would be the unmodified species (115 kDa) such as we detect in our co-IP experiments.

The NoV RdRp contains a predicted SUMO interacting motif (SIM). More importantly, these results suggest the intriguing possibility that, whether or not it is covalently SUMOylated, our co-IP results suggest NA may (also) interact non-covalently with either SUMO1 or a SUMOylated protein in transfected mammalian cells. In addition to SUMO1 conjugation, many cellular proteins have been described to also interact non-covalently with SUMO1, or with SUMO1 conjugated to SUMOylated proteins, via a SUMO-interacting motif (**SIM**) (140, 157, 161, 191). Mammalian SIMs are involved in restricting herpesvirus replication (54) and in cellular processes including transcriptional regulation and signal transduction (85). Predicting the presence of SIMs in protein sequences is relatively straightforward using bioinformatic tools (276).

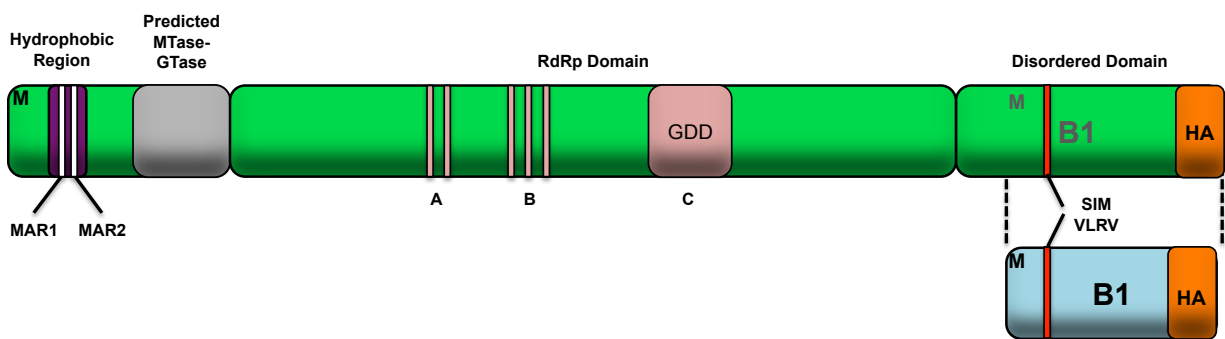
In order to test our hypothesis that NA is involved in non-covalent interactions with SUMO1, we used bioinformatics software to predict whether NA contains a SIM that might mediate such interactions. A recent survey of 148 yeast proteins shows the SUMO-binding core of a SIM is typically comprised of 3-4 aliphatic residues (V, I, or L), typically arranged with the basic pattern Φ - Φ - Φ - Φ (where Φ represents V, I, or L) (122). The following variants have also been identified: Φ -X- Φ - Φ , Φ - Φ -X- Φ , Φ - Φ - Φ -X (where X represents any residue, but is preferentially D or E). We searched the NA primary structure for these yeast SIMs using PATTINPROT server (52) to analyze the NA ORF for the following SIM core binding site patterns: [IVL]-[IVL]-[IVL]-IVL, [IVL]-[IVL]-X-[IVL], [IVL]-X-[IVL]-[IVL], and [IVL]-[IVL]-[IVL]-X. We also analyzed NA for the presence of the

following previously reported SIM consensus motifs (170): [PILVM]-[ILVM]-X-[ILVM]-[DSE>](3); [PILVM]-[ILVM]-D-L-T; and [DSE](3)-[ILVM]-X-[ILVMF](2), but this set of patterns did not yield any hits. This is possibly due to the specificity of the reported consensus sequences, specifically the inclusion of defined flanking sequences. The sequences flanking a SIM core SUMO-binding site are widely variable and to date there is a lack of available information sufficient to formulate suitable sequence predictors (122, 276). To overcome this limitation we removed extraneous predictor elements from flanking residues and searched NA again using the edited pattern sequences: [PILVM]-[ILVM]-X-[ILVM]-[DSE]; [PILVM]-[ILVM]-[DE]-[IVLAM]; and [DSE]-[ILVM]-X-[ILVMF](2). The searches using the above pattern sequences revealed 21 SIM core SUMO-binding sites on the NoV RdRp.

To determine whether any of these predicted SIM core binding sites might serve as functional SIM candidates, NA was analyzed using a previously published bioinformatical pipeline protocol (276) as described in this chapter's Materials and Methods section (3.2). The protocol was designed to trim down the number of SIM candidates by predicting whether a SIM might be accessible to SUMO1 for non-covalent interaction without interfering with functional domains. The PFAM server was used to locate functional domains on NA and the positive-strand virus RdRp domain was predicted from residues 532-738 (74). The canonical RdRp motifs involved in catalytic activity (**Figure 26**, yellow boxes; and **Figure 31A**, RdRp motifs) fall within residues 594-700, which we deemed a critical RdRp region in accordance with previous structure-function studies of viral RdRps (95). Predicted SIMs that fell within this critical RdRp region were eliminated from further analysis because this catalytic active site

Figure 31: The predicted domains and motifs on the NoV RdRp. (A) Linear depiction of NA showing the various domains, motifs and regions described in this dissertation as well as in the literature (127). The N-terminal hydrophobic region contains MARs 1 and 2, as described in **Chapter 2**. The bounds of the RdRp domain were predicted using the PFAM server (74). Within the RdRp domain there are 3 predicted SUMO consensus motifs, with the conserved motif (LKIE 722-725) highlighted by the red line. The GlobPlot 2 and IUPRED servers were used to predict the bounds of the C-terminal disordered domain, which contains the predicted candidate SUMO-interacting motif (**SIM**) VLRV. (B) IUPRED server (65, 66) prediction of the ordered/disordered status of NA. The disorder tendency of the protein (y-axis) represents the likelihood of NA to be either globular or disordered with a cutoff of 0.5 (blue line). NA is predicted to be mostly globular up to approximately aa 850 (blue bar) with the C-terminus being highly disordered.

A



B



region is unlikely to participate in protein-protein interactions other than those required for catalysis. Predicted SIM core binding sites found outside of the critical RdRp region from residues 532-594 and 700-738 were flagged for further cautious analysis, since mutating these areas in an attempt to determine their potential role as SIMs is likely to pose a danger to RdRp catalytic activity.

The GlobPlot 2 (151) and IUPRED (65, 66) programs were used to predict the globularity/disorder status of NA (**Figure 31B**). Predicted SIMs located in globular domains are weak candidates because SUMO1 typically interacts with a SIM in a disordered domain, where the interaction with SUMO stabilizes the disordered domain into a more ordered structural arrangement (132, 133, 276). GlobPlot 2 predicts residues 1-96 and 114-804 as globular (**Figure 31A**) and IUPRED predicts residues 1-865 as globular (**Figure 31B**). Residues 1-804 of NA were predicted to be globular by both programs, rendering the predicted SIMs in this region to be poor candidate choices. All predicted SIM core binding sites fell within the predicted globular domains of 1-804 on NA with the exception of sites 840-844 (DVDLM) and 953-956 (**VLRV**). GlobPlot 2 and IUPRED disorder predictions show the SIM core binding site **VLRV** at 953-956 falls within a region of NA with significantly high disorder tendency (>0.5) making it much more likely to be a functional SIM. The presence of the predicted SIM core binding site may confirm the hypothesis that NA and SUMO1 interact non-covalently via a SIM and future experiments will be aimed to determine whether this SIM plays a role in NoV RNA replication or some other aspect of the viral life cycle.

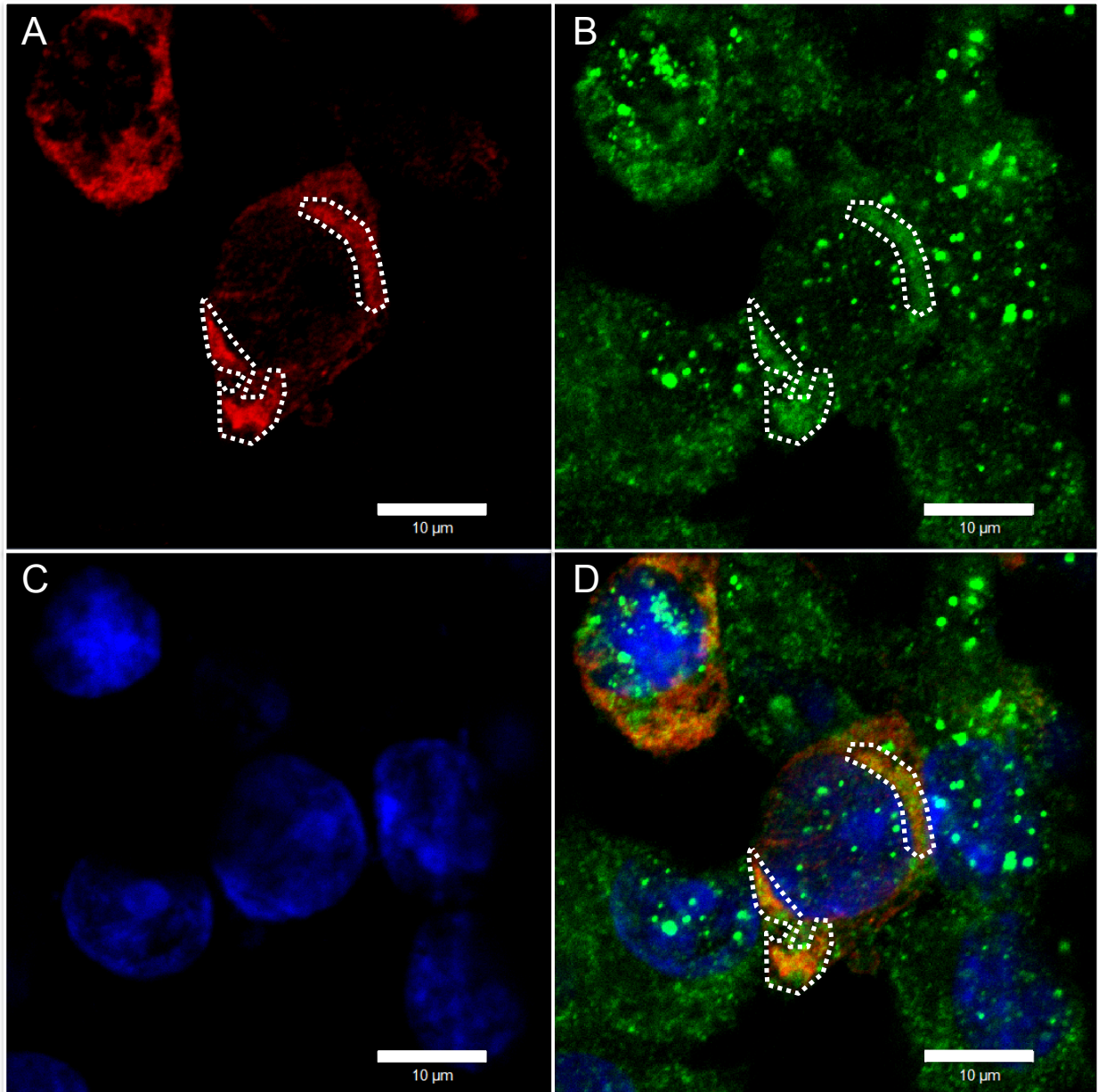
SUMO1 and the NoV RdRp co-localize in transfected mammalian cells.

Accumulating evidence continues to highlight the importance of the interaction between

SUMO1 and the RdRp. To further characterize this interaction and to begin to address its function, we used immunofluorescence confocal microscopy to examine the subcellular localization of NA and SUMO1. BSR-T7/5 cells were grown in 6-well plates with glass coverslips and transfected with pT7-N1-HA. After 24 hours, the cells were fixed in 4% PFA overnight at 4°C and permeabilized with 0.1% Triton X-100. These cells were processed for immunofluorescence of NA (**TR**, Red) and SUMO1 (**FITC**, green) as described in this chapter's Materials and Methods section (**3.2**).

The fluorescence signal of NA is typical of that shown in **Chapter 2**, with the characteristic mitochondrial clusters (**Figure 32A**, regions of interest [**ROI**] delineated by dashed line) (Reference (84) and **Chapter 2**) SUMO1 immunofluorescence was seen as bright puncta localized to the nucleus and also in the cytoplasm (**Figure 32B**). The majority of SUMO1 staining in the cytoplasm co-localized to the discrete sites of NoV RCs (**Figure 32A and B**). When the degree of co-localization between SUMO1 and NA was measured in the selected ROIs as previously described (**Chapter 2** and reference (84)), we found that the majority of SUMO1 staining (72% and 79% for lower ROI and upper ROI, respectively) co-localized to virtually all NA staining (99% for both lower and upper ROI) (**Table 5 and Figure 32D**, delineated by dashed line). The significant difference in SUMO1 subcellular localization between untransfected cells (**Figure 32D**, cells on right side) and cells expressing NA (**Figure 32D**, cells marked with ROIs) was that the SUMO1 staining took on a discrete shape in the cytoplasm that co-localized to NoV RCs that are associated with mitochondria. Although further work is required to determine the nature and functional significance of this interaction, the co-localization of SUMO1 and/or SUMOylated proteins with the RdRp and with RCs continues to suggest

Figure 32: The NoV RdRp and SUMO1 co-localize in the cytoplasm of transfected BSR-T7/5 cells. BSR T7/5 cells were transfected with pT7-N1-HA and at 24 hpt cells were fixed and permeabilized as described in the legend to **Figure 14**. The HA-tagged RdRp was detected by immunostaining using TR-labeled antibodies (**A**, red). SUMO1 was detected using FITC-labeled antibodies (**B**, green). Cell nuclei were stained with DAPI (**C**, blue). Merged signals are shown (**D**); the delineated orange signal on merge panel indicates co-localization between TR and FITC signals. Scale bar = 10 μ M.

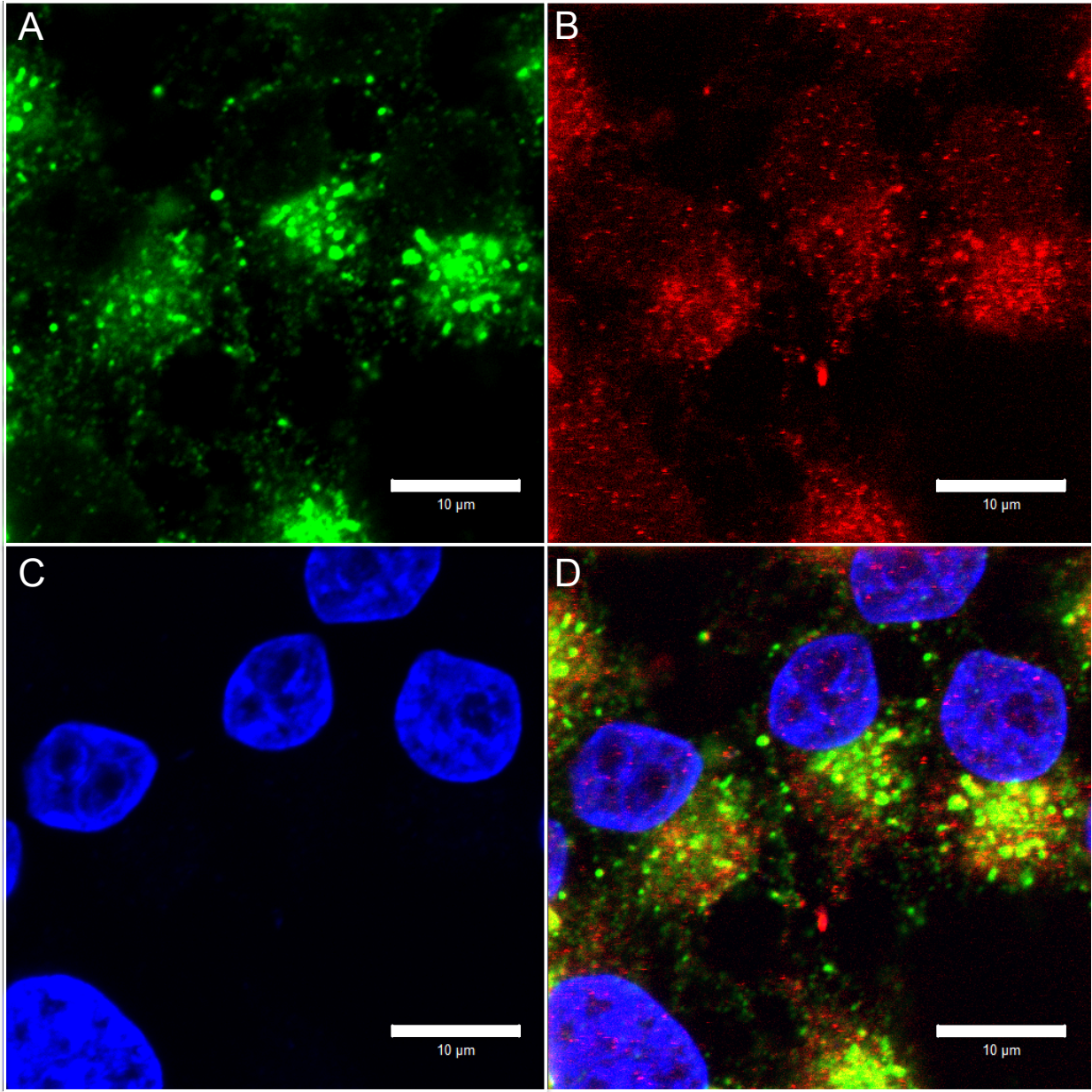


the intriguing possibility that this interaction is relevant for RC formation or maintenance, particularly in light of the role played by SUMO1-conjugated proteins (e.g., Drp1) in regulation of mitochondrial dynamics.

Expression of NA disrupts Drp1 localization to the mitochondria in mammalian cells. Drp1 trafficking events are crucial processes of mitochondrial fission and, if inhibited, the cellular mitochondria begin to aggregate and cluster (190). Upon SUMOylation, Drp1 is translocated to the mitochondria, where it associates with its OMM-bound receptors MFF and MiD49/51 to induce mitochondrial fission (156, 240). As described in the introduction section of this chapter (3.1), we hypothesize that NoV RC formation involves disrupting the equilibrium of mitochondrial dynamics by interfering with Drp1 function, thereby preventing fission and ultimately resulting in mitochondrial clustering (i.e., fusion). Since translocation of Drp1 is essential to its function, we wished to determine the effect of NA expression on its cellular localization, which we examined using immunofluorescence confocal microscopy (**Figures 33 and 34**).

As a control and to confirm the localization of Drp1 in the absence of the viral RdRp, untransfected BSR-T7/5 cells were fixed and processed for immunostaining and imaged as described in this chapter's Materials and Methods section (3.2) and in Chapter 2 (2.2). Mitochondria were stained with MTR for 1 hour prior to fixation and Drp1 was immunostained using rabbit anti-Drp1 primary and FITC-labeled goat anti-rabbit secondary antibodies. In these untransfected cells, Drp1 was detected mostly clustered in the cytoplasm (**Figure 33A**) with puncta in close proximity to MTR staining puncta (**Figure 33B and D**), which is consistent with the localization described for Drp1

Figure 33: The subcellular localization of Drp1 in BSR-T7/5 cells. Untransfected BSR T7/5 cells were stained with MTR (red) then fixed and permeabilized as described in this chapter's Materials and Methods section (3.2). Drp1 was detected by immunostaining using FITC-labeled antibodies (**A**, green). MTR staining is shown in panel **B**, red. Cell nuclei were stained with DAPI (**C**, blue). Merged signals are shown (**D**); orange signal on merge panel indicates co-localization between FITC and MTR signals. Scale bar = 10 μ M.

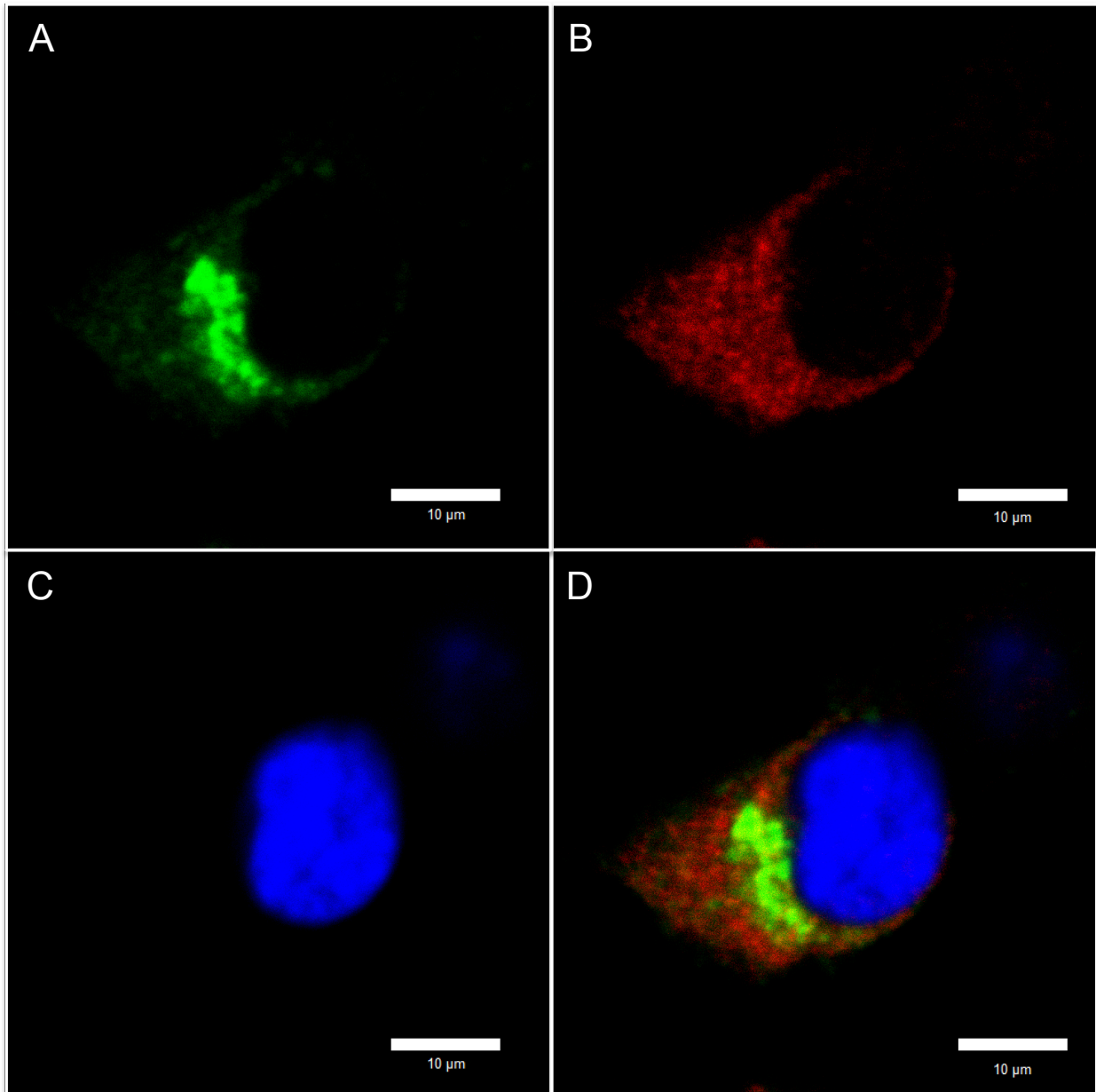


in the literature (239, 240, 281). In these cells, the total staining of both Drp1 and MTR was measured as described above (**Chapter 2** and reference (84)) and approximately half of the Drp1 staining co-localized to MTR (**Table 5**, 48%, 50% and 58% for the cells on the left, center and right sides, respectively).

For Drp1 localization in the presence of the RdRp, we performed the following preliminary experiment. BSR-T7/5 cells were grown on coverslips and transfected with pT7-N1-HA. The cells were fixed in 4% PFA and permeabilized in 0.1% TX-100 24 hours after transfection. Fixed cells were immunostained to detect the NoV RdRp using mouse anti-HA primary and goat anti-mouse FITC-labeled secondary antibodies. Drp1 was detected using rabbit anti-Drp1 primary and goat anti-rabbit TR-labeled secondary antibodies.

In cells expressing the NoV RdRp, NA fluorescence was detected as a clustered mass (**Figure 34A**) previously shown to co-localize with the OMM and with viral RCs (**Chapter 2** and reference (84)). Although in **Figure 33**, where an average of 52% of Drp1 staining co-localized to MTR staining and 48% of Drp1 was not associated with MTR (**Table 5**), Drp1 exhibited a diffuse cytoplasmic fluorescence pattern. This staining pattern overlapped to a degree with NA staining (63% Drp1 with NA; **Figures 34D and Table 5**). The moderate level of signal overlap does not represent true co-localization in this figure, since Drp1 staining was diffuse throughout the cytoplasm and NA staining maintained a defined shaped throughout the cytoplasmic Z-axis (**data not shown**). This Drp1 staining pattern is unlike that in untransfected cells (**Figure 33A**) where Drp1 localization in the presence of NA is altered. While they are preliminary and need to be repeated, these results suggest that the presence of the NoV RdRp does alter the

Figure 34: The NoV RdRp alters the subcellular localization of Drp1 in transfected BSR-T/5 cells. BSR T7/5 cells were transfected with pT7-N1-HA and at 24 hpt cells were fixed and permeabilized as described in the legend to **Figure 33** and in this chapter's Materials and Methods section (**3.2**). The HA-tagged RdRp was detected by immunostaining using FITC-labeled antibodies (**A**, green). Drp1 was detected using TR-labeled antibodies (**B**, red). Cell nuclei were stained with DAPI (**C**, blue). Merged signals are shown (**D**). Scale bar = 10 μ M.



subcellular localization of Drp1 in transfected mammalian cells, perhaps by affecting its translocation.

In order to get a clearer picture of the altered mitochondrial morphology phenotype during expression of N1, we need to analyze the 3 pertinent factors (NA, Drp1 and MTR staining of mitochondria) simultaneously in the same cell(s). Our current experimental setup for imaging Drp1 translocation is limited in that we cannot yet image mitochondria and Drp1 simultaneously. Co-fluorescence imaging of MTR and TR would produce MTR-emitted photons (599 nm) able to excite TR dye molecules (TR excitation 595 nm), resulting in signal emission bleed over. We propose to overcome this pitfall through the use of a third fluorescently labeled secondary antibody with an excitation/emission spectrum able to be cleanly differentiated from FITC or MTR/TR. Experiments using this secondary antibody are addressed in the Future Experiments section (3.4.1).

Summary of Chapter 3 experimental approaches and results. This concludes the completed experimental approaches for this chapter. We have shown that the NoV RdRp is a target for SUMOylation *in vitro* where a SUMOylated NA species is readily detectable. The NoV RdRp interacted with SUMO1 in cultured mammalian cells and this interaction was detectable using co-IP and immunofluorescence confocal microscopy methods. The interaction with SUMO1 as detected by co-IP was lost in the presence of a mutant version of NA in which three SUMO consensus acceptor lysine residues (K523, K655 and K723) in NA were changed to alanine. However, whether NA is covalently SUMOylated remains to be determined and mass spectrometry will be

employed in the future. To further define the interaction between SUMO1 and NA we used bioinformatic analysis to predict the presence of a strong SIM candidate on NA. The significance of this predicted SIM in the NA replicative cycle or NoV RC formation will be addressed in future experiments using site-directed mutagenesis to neutralize or delete the SIM. Continuing with our hypothesis that NA disrupts mitochondrial fission, we tested whether NA altered the activity of Drp1. The mitochondrial localization of Drp1 seen in untransfected cells changed in the presence of NA to a diffuse cytoplasmic staining that fails to co-localize with the mitochondria, suggesting that NA expression affects normal Drp1 trafficking.

Our current working model hypothesizes that NoV RC formation disrupts mitochondrial dynamics by inhibiting or down-regulating mitochondrial fission. To accomplish this, we predict NA interferes with SUMOylation of Drp1, altering its translocation and its subsequent activity in mitochondrial fission. In order to prepare this work for publication, we propose the following future experiments, which are described with more detail in the Future Experiments section (**3.4**).

In Section **3.4.1** we propose using immunofluorescence confocal microscopy to analyze Drp1 translocation inhibition in multi-labeled cells. This experiment will overcome our current technical limitation of overlapping excitation/emission spectra of our fluorescent dyes and secondary antibodies and allow us to visualize NA, Drp1, and mitochondria simultaneously. Our proposed experiment in Section **3.4.2** is a time course analysis of Drp1 localization by immunofluorescence confocal microscopy and Drp1 membrane association by subcellular fractionation to determine whether Drp1 translocation is inhibited by NA. We hypothesize that NA is inhibiting Drp1 translocation

Table 5: Overlap coefficients calculated for confocal microscopy experiments shown in Figures 32, 33, and 34.

CONFOCAL MICROGRAPH BY EXPERIMENT	OVERLAP COEFFICIENT (OC)*
SUMO1 and NA Localization (Figure 32)	
SUMO1 with NA	
Upper ROI	79.0
Lower ROI	72.0
NA with SUMO1	
Upper ROI	99.0
Lower ROI	99.0
Drp1 Localization (Figure 33)	
Drp1 with MTR	
Left Cell	48.0
Central Cell	50.0
Right Cell	58.0
Drp1 Localization during NA Expression (Figure 34)	
Drp1 with NA	63.0

*OC is defined as the percentage overlap between red (MTR or TR) and green (FITC) pixels, as described in Chapter 2 Materials and Methods section (2.2) and in reference (160).

to the OMM where Drp1 assembles at fission locations and this inhibition correlates to the timeframe of NoV RC formation (**Chapter 2**). Finally, in section **3.4.3** we propose to determine whether the NoV RdRp serves as an antagonist of SUMOylation-dependent mitochondrial fission by analyzing Drp1 SUMOylation during NA expression. We hypothesize that NA outcompetes Drp1 for SUMO1 interaction disrupting Drp1 mitochondrial fission, which we expect can be reversed by mutating the SUMO consensus motifs, SIM or MARs on NA.

3.4 Future Experiments

3.4.1 Immunofluorescence confocal microscopic analysis of Drp1 translocation inhibition in multi-labeled cells. In **section 3.3**, we analyzed the subcellular localization of the NoV RdRp and Drp1, but for technical reasons were unable to simultaneously localize these proteins to the mitochondria. Therefore, we propose to analyze NA- and Drp1-immunostaining along with MTR staining in the same sample, using a different fluorophore to detect Drp1. The excitation/emission (nm) spectra for our current fluorescent reagents are approximately 358/461, 490/520, and 579/599 for DAPI, FITC and MTR, respectively. We propose to detect Drp1 using the BD Horizon Brilliant™ Violet 711 tandem fluorochrome conjugated secondary antibody, which has an excitation/emission spectrum of 407/711 and will not interfere with the other fluorescent signals. This will provide a more inclusive perspective of the interactions between the mitochondrial dynamics system and NoV RCs than would be obtained from the pairwise comparisons described for **Figures 33 and 34**.

Expected results. We predict that this triple-labeling protocol will allow us to simultaneously localize the NoV RdRp to mitochondria by immunofluorescence and MTR staining as previously described in **Chapter 2** (84) while analyzing Drp1 localization in the presence of the RdRp (and its absence in control transfections). We anticipate that this protocol will confirm our finding that Drp1 immunofluorescence localizes to the mitochondria in the absence of the RdRp (**Figure 33**) but exhibits diffuse cytoplasmic staining no longer co-localized to mitochondria in its presence of NA (**Figure 34**). If these results prove to be reproducible, we would conclude that expression of NA inhibits Drp1 localization to clustered mitochondria, perhaps by interfering with its translocation from the cytoplasm to mitochondria.

3.4.2 Kinetics of Drp1 translocation inhibition by the NoV RdRp. To determine whether NA alters the active process of Drp1 translocation, we propose to examine the kinetics by which Drp1 localization to mitochondrial membranes occurs in the presence and absence of NA. This will involve time course experiments using two different analytical approaches: immunofluorescence confocal microscopy following the triple labeling protocol described in **Section 3.4.1** and cellular fractionation studies using differential density gradient centrifugation.

These experiments will allow us to determine the approximate time frame in which Drp1 localization to mitochondrial is inhibited and to determine whether this represents alteration of its translocation, the first step in the fission process. In each case, we will transfect BSR-T7/5 cells with pT7-N1-HA and incubate at 37°C. At four-hour intervals from 0-24 hpt, samples will be prepared and analyzed as follows. For the confocal microscopy, transfected cells will be processed for immunofluorescence to

detect NA, Drp1 and MTR using the triple labeling protocol described above section (3.4.1).

Expected results for the immunofluorescence confocal microscopic analysis. If Drp1 localization is disrupted over time according to the kinetics of NA membrane association then we expect Drp1's mitochondrial translocation to cease at a time point at least 8 hours after NA expression begins i.e. when the mitochondria begin to cluster in the presence of NA (**Chapter 2, Figure 16B**).

After translocation to the mitochondria, SUMOylated Drp1 stably associates with the OMM where it assembles into ring structures around the sites of fission (119). Therefore, subcellular fractionation experiments will be used to analyze Drp1 association with mitochondrial membranes in cells expressing NA. Cells will be harvested at each time point and subcellular fractions prepared as previously described (84). Briefly, cells will be lysed by Dounce homogenization in iso-osmotic buffer (10 mM HEPES-NaOH, pH 7.4, 250 mM sucrose, 1 mM EDTA and 0.5 mM magnesium acetate) supplemented with protease inhibitors as described in Materials and Methods section (3.2). Cell debris will be removed by centrifugation at 1,200 x g. The lysates will be centrifuged at 20,000 x g and both supernatant and pellet fractions will be collected. The supernatant represents the cytoplasmic fraction while the pellet contains the total mitochondrial fraction. For analysis, the pellet fraction will be resuspended in lysis buffer (50 mM Tris-Cl, pH 7.4, 1% NP-40 and 150 mM NaCl) containing the same protease inhibitors. The fractions from each time point will be analyzed by Western blot to detect Drp1, NA, and cellular proteins monoamine oxidase (**MAO**) and tubulin as markers for proper subcellular fractionation.

Expected results for subcellular fractionation. Drp1 is mostly cytosolic prior to fission (not associated with OMM yet occupying the same cytoplasmic space) until it is SUMOylated. Therefore, in mock- or un-transfected samples we expect to find Drp1 in both cytoplasmic and mitochondrial fractions. We predict that NA inhibits Drp1 translocation to the mitochondria where it stably associates with the OMM and therefore we expect Drp1 to be detected almost exclusively in the cytosolic fraction in these samples.

3.4.3 Effect of NoV RdRp on Drp1 SUMOylation in transfected cells.

Partitioning of Drp1 between the cytoplasm and the mitochondrial membrane is dependent on post-translational modifications, particularly phosphorylation and SUMOylation. Our model predicts that NA inhibits mitochondrial fission by interfering with Drp1 SUMOylation by MAPL and preventing Drp1 translocation. Our preliminary results suggest NA may disrupt Drp1 translocation because Drp1 localization is altered when NA is expressed (**Figure 34**). The following experiments will examine whether NA prevents Drp1 translocation at the level of Drp1 SUMOylation in transfected cells. We will simultaneously test whether the predicted SUMO consensus motifs, the predicted C-terminal SIM, or membrane association of NA is required for interference of Drp1 SUMOylation in BSR-T7/5 cells.

We will first need to generate our NA SIM mutants using site directed mutagenesis. We propose to make two mutant variants of the NA to remove the VLRV core binding site at position 953-956. The first mutant will have the VLRV residues changed to amino acids of similar structure with approximately biochemical properties in order to not avoid drastic changes to protein structure, specifically V953T-L954N-

R955E-V956T; this mutant will be designated NA_{TNET}. The second mutant will have the core binding site deleted entirely and be designated NA_{ΔVLRV}.

Cells will be transfected to express WT NA, NA_{K-A}, NA_{TNET}, NA_{ΔVLRV}, or NA_{Δ12-64}. Cells will be lysed after 24 hours as described in the above section (3.2), and Drp1 will be immunoprecipitated using a rabbit anti-Drp1 polyclonal antibody and goat anti-rabbit magnetic secondary antibodies. The Drp1 immunoprecipitates will be analyzed by Western blot using anti-Drp1 and anti-SUMO1 antibodies to detect SUMO-conjugated species of Drp1.

Expected results. Our model predicts that NA interferes with SUMOylation-dependent Drp1 translocation by competing for limited amounts of SUMO1 or SUMOylating enzymes like the E3 ligase, MAPL. Therefore, we expect that NA occupies the available SUMO1 moieties via SUMOylation or by interacting non-covalently with SUMO1 via its predicted C-terminal SIM. In cells expressing WT NA, we expect to detect a reduction in Drp1-SUMO1 conjugates compared to mock-transfected cells. This result would be in accordance with our current data (**Figure 34B**) where NA expression alters the subcellular localization of Drp1, since Drp1 SUMOylation is required for mitochondrial translocation and subsequent OMM association. Conversely, we expect to see levels of Drp1-SUMO1 conjugates that are unaffected in samples expressing the mutant forms of NA that unable to interact with SUMO1 (NA_{K-A}, NA_{TNET}, and NA_{ΔVLRV}), or attach to the OMM (NA_{Δ12-64}). These results as a whole would suggest that NA interferes with mitochondrial fission by binding SUMO1 (covalently or non-covalently) at the OMM and preventing Drp1 translocation.

Additionally we would examine whether mutating the predicted SIM on NA prevents NA and SUMO1 interaction by co-IP. If either of these mutants results in a loss of SUMO1 interaction by Western blot analysis that would suggest the sequence VLRV is serving as a SIM on NA, which would open more opportunity to determine whether SUMOylated proteins are forming a complex with NA or interacting transiently with NA, in studies beyond the scope of this dissertation project.

It is also possible that some other mechanism of inhibiting Drp1 is occurring during NoV RC formation. Drp1 is also regulated to induce fission by phosphorylation at serine 616 (**S616**) (42). Therefore, we propose to determine whether the NoV RdRp inhibits Drp1 phosphorylation at S616 by using immunoprecipitation and Western blot analysis using a commercial phospho-Drp1 antibody (Cell Signaling Technology) already in our possession. We will also analyze Drp1 phosphorylation during NA expression using immunofluorescence and subcellular fractionation.

Presumably, NA is expressed in high enough amounts during infection to outcompete Drp1 for SUMOylation, resulting in decreased levels of SUMO1-Drp1 conjugates and the reduced level of mitochondrial fission. Alternatively, NA may not be SUMOylated to levels high enough to outcompete Drp1 for SUMO1 modification, since we have not been able to observe SUMOylated NA species, or NA may not be SUMOylated at all. These two scenarios need definitive confirmation using mass spectrometry. Nevertheless, when the NoV RdRp is expressed in cultured mammalian cells, mitochondrial fission and Drp1 appear to be stalled with nearly all of the mitochondria clustered into discrete complexes.

3.5 Conclusions

The focus of this chapter was to determine the role the clustered mitochondria described in **Chapter 2** may play in formation of NoV RNA replication complexes (**RCs**). We were intrigued by the similarity between this mitochondrial phenotype and that seen in metabolic and neurological disorders in which mitochondrial dynamics are altered. This led us to investigate how NoV might engineer a collapse of the vital mitochondrial dynamics system.

Mitochondrial dynamics are controlled by a balance between specific fusion and fission pathways, the latter being regulated in part by SUMOylation (231). SUMOylation is a major post-translational modification of mitochondrial proteins, as evidenced by the discovery of a mitochondrial-anchored protein ligase (**MAPL**), which functions as a SUMO E3 ligase able to conjugate SUMO1 to proteins, and a cytoplasmic pool of SENPs that specifically deSUMOylate mitochondrial SUMO substrates (34, 109, 298).

It was this link to SUMOylation that led us to hypothesize a possible mechanism by which NA might be affecting mitochondrial dynamics. When we initiated these studies, we had already determined that NA was predicted to have three consensus SUMOylation motifs (one conserved amongst all of the alphanodavirus RdRps), along with several non-consensus motifs. The results of our *in vitro* SUMOylation assay confirmed that NA could be SUMOylated (Pal, Johnson, and Rosas-Acosta, unpublished, **Figure 27**), but the implications of this modification for the NoV life cycle were unclear. Taken together, these observations and the role of Drp1 SUMOylation in controlling mitochondrial fission led us to hypothesize that NoV RC formation disrupts

mitochondrial fission, perhaps by NA outcompeting Drp1 for SUMOylation, resulting in clustered mitochondria.

We initially analyzed whether the NoV RdRp was SUMOylated in mammalian cells by performing co-IP experiments from cells expressing NA-HA. In the first experiment, we were unable to detect any NA-SUMO1 conjugates when we performed the IP using antibodies against NA followed by Western blot analysis using SUMO1 antibodies (**Figure 28**). Nevertheless, we anticipated difficulty detecting SUMOylated forms of NA from past discussions with colleagues analyzing SUMOylation of *Influenza virus* proteins (188, 189) and LEDGF/p75 (40). Therefore, we attempted to use an alternative approach to further investigate whether NA SUMOylation might play a role in the viral life cycle.

We performed a reverse co-IP in which we pulled down SUMO1-conjugates using our SUMO1 antibody and followed this with Western blot analysis using our mouse anti-HA antibodies. In this experiment we were able to readily detect NA co-precipitating with SUMO1 even in the absence of exogenously added SUMO1 (**Figure 29**). This result suggested that NA is interacting with endogenous SUMO1 in mammalian cells, but we were unable to detect any higher molecular weight species corresponding to covalently modified NA. However, this pivotal result embarked us on a path to characterizing a novel protein-protein interaction between *Nodamura virus* protein A and SUMO1 that has far reaching implications into vital cellular mechanisms involving mitochondria.

To further characterize the interaction between the NoV RdRp and SUMO1, we performed site-directed mutagenesis to alter the three predicted SUMO consensus

motifs on NA. Specifically, we changed each motif's SUMO acceptor lysine residue to alanine, thereby preventing SUMOylation at that site. The RdRp mutant NA_{K-A} did not co-IP with SUMO1 (**Figure 30**) suggesting that NA may be SUMOylated in mammalian cells at one of these lysine residues (K523, K655 or K723). Additional studies will be needed to determine which of these lysine residues is affected, and single and pairwise combinations of the K-A changes will be tested using the same assay. Since one such motif is conserved amongst all of the alphadaviruses, this may have implications for a common mechanism of RC formation throughout this virus genus.

Since NA readily co-immunoprecipitated with SUMO1, suggesting these two proteins were interacting, we used bioinformatical analysis to determine whether NA contained any motifs such as a SUMO-interacting motif (SIM) that might be predicted to facilitate a non-covalent NA-SUMO1 interaction. Using a published bioinformatical pipeline designed to predict ubiquitination sites and SIMs (276), we were able to determine that NA has a candidate SIM at its C-terminus at residues 953-956 (VLRV). This sequence falls outside any of the RdRp motifs within a predicted disordered region (**Figure 31**), such as those shown previously for other SIM-containing proteins (122). We proposed a future experiment in which we use site-directed mutagenesis to alter the predicted SIM within NA and examine the resulting mutants, NA_{TNET} and NA Δ _{VLRV}, for their ability to interact with SUMO1 by co-IP and immunofluorescence microscopy (**Section 3.4.3**).

Accumulating evidence continues to highlight the importance of the interaction between SUMO1 and the RdRp. To further characterize this interaction and to begin to address its function, we used immunofluorescence confocal microscopy to determine

the subcellular location of NA-SUMO1 interactions (**Figure 32**). In cells expressing NA there is a clear co-localization between NA and SUMO1 in the cytoplasm where interaction appears to occur in discrete sites, which we have previously shown to be NoV RCs on the OMM (**Table 5 and Figure 32D**). This result suggests the NoV RdRp and SUMO1 interact in cultured mammalian cells and further implicates SUMO1 in NoV RC formation and mitochondrial clustering.

We continued testing our hypothesis that NA outcompetes Drp1 for SUMOylation resulting in inhibition of mitochondrial fission and clustering of mitochondria. We focused our efforts on determining how mitochondrial clustering occurs during NoV RC formation and began examining NA's effects on mitochondrial dynamics, specifically inhibition of mitochondrial fission. To determine whether NA disrupts Drp1-mediated mitochondrial fission, we first analyzed Drp1 localization to the mitochondria in untransfected cells by immunofluorescence confocal microscopy (**Figure 33**). Drp1 in untransfected BSR-T7/5 cells was observed to be cytoplasmic, with the majority of Drp1 staining co-localizing to mitochondria through out the cytoplasm (**Table 5 and Figure 33D**). This is the normal localization of Drp1, which is cytoplasmic and not associated with mitochondrial membranes. The appearance of co-localization between cytoplasmic Drp1 and mitochondria is indicative of the two sharing the same space in the cytoplasm and the dynamic nature of fission where a portion of mitochondria and Drp1 are involved in fission and physically associated (42, 236, 281). Drp1 requires post-translational modification (SUMOylation) to translocate to and physically interact with the OMM. We shall address this aspect of Drp1 regulation in our system and how NoV RC formation affects it in the future.

In cells expressing NA, Drp1 was seen to be diffuse throughout the cytoplasm and did not appear to co-localize with NA clusters associated with mitochondria (**Figure 34D**) despite the measured OC of the imaged staining pixels, for the reasons outlined in section **3.3 (Table 5)**. This result suggested that Drp1 localization was somehow altered by the presence of NA. This may lead to clustered mitochondrial morphology since disrupted Drp1 activity is well documented to result in mitochondrial aggregation (70, 240). More testing is required in order to determine the exact mechanism NA is utilizing to prevent fission. Nevertheless, the implications of this work and our future plans in this area are described in the Discussion (Chapter 4).

Chapter 4: Discussion

4.1 NoV RC localization and NA membrane association. The hub of this dissertation is analyzing the localization and function of the NoV replication complex (RC), the site of RNA replication in the cell. To that end, our first goal was to determine the subcellular location of NoV RdRp and RCs in mammalian cells using immunofluorescence confocal microscopy and biochemical methods. Our major finding in this study is that NA associates with clustered mitochondria as an integral membrane protein and synthesizes RNA at these sites (84). Although the NoV RdRp is shown here to be an integral membrane protein with two N-terminal MARs that play a critical role in RC formation, the exact nature of the interaction between the RdRp and the membrane is not yet clear. The RdRps of the related nodaviruses FHV and GGNNV are integral membrane proteins that interact with mitochondrial membranes via transmembrane alpha helices (106, 168). However, these RdRps are markedly different from that of NoV, with the NoV and FHV RdRps sharing 44% amino acid sequence identity (128) and those of NoV and GGNNV sharing only 26% amino acid sequence identity as we calculated using ClustalW2 software. We therefore hypothesize that the mechanism of interaction between the NoV RdRp and mitochondrial membranes differs from those shared by the FHV and GGNNV RdRps (**Figure 35**). The presence of proline and charged residues within both NoV MARs make it unlikely that the NoV RdRp actually spans the OMM via transmembrane alpha helices within this region. Instead it may remain on the outer membrane as a monotopic integral membrane protein, nesting in the outer leaflet with parallel hydrophobic helices as has been described for other

membrane-associated proteins (196, 277), including the ER-localized ATPase, torsinA (268).

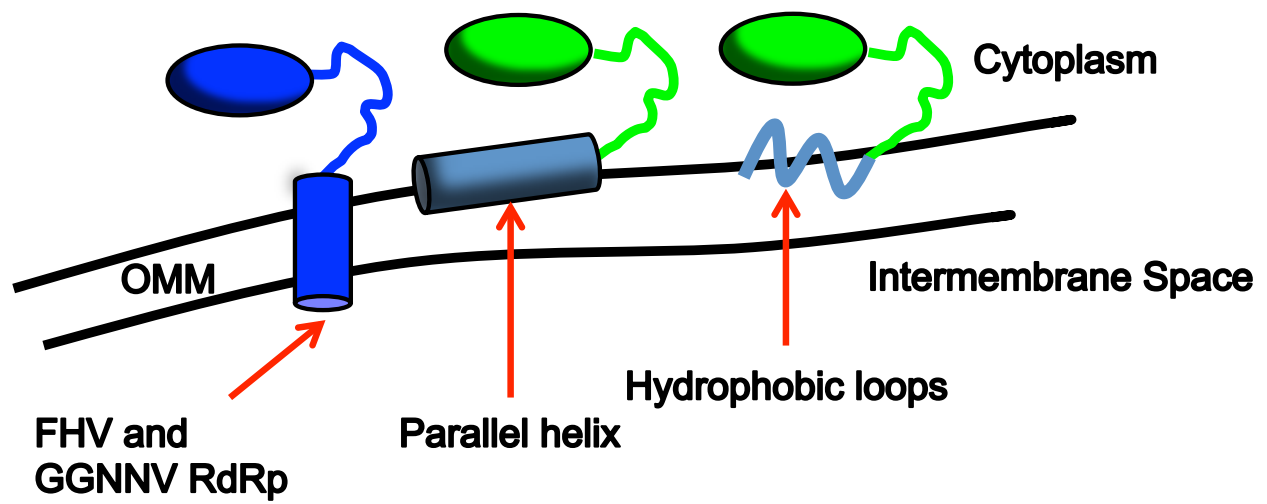
4.2 The NoV RdRp may perturb mitochondrial apoptosis during infection.

Virus replication can induce mitochondrial damage and mitochondrial dysfunction, leading to the buildup of reactive oxygen species (**ROS**) in the cytoplasm, which damages the cell and initiates a cycle of further mitochondrial damage and ROS production (150). If not brought under control, this mitochondrial stress will ultimately lead to OMM breakdown and the release of pro-apoptotic factors such as cytochrome *c* and Smac/DIABLO (280). Some viruses enhance apoptosis in infected cells to expedite progeny release and infection of other cells, using various tactics including increasing ROS production (93, 211).

Likely as a direct consequence of disrupting mitochondrial integrity (278), FHV and GGNNV induce apoptosis in infected cells (46-48, 234). FHV infection induces apoptosis in cultured *Drosophila* DL-1 cells by inhibiting cellular translation, thereby resulting in depletion of *Drosophila* inhibitor-of-apoptosis protein (**DIAP1**) (234), while GGNNV-infected cultured sea bass (**SB**) and COS-7 cells undergo apoptosis through activation of a caspase-dependent pathway (46-48). For GGNNV, this process is mediated by proteins B1 and B2 (45, 249).

In contrast, some viruses either fail to induce apoptosis or inhibit this cellular defense mechanism (136). NoV infection in cultured mammalian cells does not appear to result in apoptosis or, in fact, exhibit any apparent cytopathic effects (**CPE**). For example, no cellular morphological changes associated with apoptosis are observed in BHK21 cells transfected with purified NoV genomic RNA1 and RNA2 even at 24 hpt,

Figure 35: Potential topologies adopted by the NoV RdRp in its interaction with the OMM. The FHV and GGNNV RdRps interact with the OMM via transmembrane alpha helices (blue). The presence of charged and proline residues in the NoV RdRp predicted MARs prevents the MARs from traversing the OMM as transmembrane alpha helices. Therefore, we hypothesize that the NoV RdRp is a monotopic integral membrane protein that interacts with the outer leaflet of the OMM. We hypothesize the MARs mediated membrane anchoring either via parallel helices embedded into the outer leaflet, or by hydrophobic loops that weave in and out of the outer leaflet.



when abundant RNA replication and progeny virus particles were detected (14). Furthermore, during the time course of this study (**Figure 16**) and our previous studies (124, 125), cells expressing the NoV RdRp did not exhibit any of the morphological hallmarks of apoptosis, including cytoplasmic vacuolization, membrane blebbing, rounding, nuclear fragmentation, or detachment from the growth surface. Instead, in this study the cells appeared healthy for up to 24 hpt and in a previous study, the cells did not appear apoptotic even 12 days post-infection (124). Finally, since caspase-3 will cleave HA tags from expressed proteins (37), our ability to detect the HA-tagged NoV RdRp in transfected mammalian cells suggests that activation of an intrinsic, caspase-mediated apoptotic pathway (278) in these cells is unlikely. Therefore, while it is clear that NoV establishes RCs in conjunction with mitochondrial membranes via direct interaction with its RdRp, the mitochondria do not appear to initiate an apoptotic cascade. The lack of CPE and apoptosis from NoV is unique among the nodaviruses studied to date, and may represent a unique adaptation in a virus whose natural host range has expanded to include mammals.

It is possible that either NoV fails to induce or actively prevents apoptosis. Since the initiation factors for the intrinsic apoptotic pathway lie within the mitochondria, these organelles are a prime target for a virus to manipulate to delay apoptosis (278, 280). For example, NoV could inhibit hyper-fragmentation of mitochondria and subsequent release of cytochrome *c* (281), thereby preventing apoptosis. Alternatively, NoV might do so by inducing mitophagy, the cellular process whereby damaged mitochondria are destroyed and their components recycled, thereby delaying apoptosis. The literature describes several viruses that avoid apoptosis by perturbing different cellular functions

to increase mitophagy (135, 292). In cells infected with Hepatitis B virus (**HBV**), expression of HBV X protein (**HBx**) initiates a cascade that increases mitochondrial fission and promotes mitophagosome formation to clear out damaged mitochondria with the ultimate goal of preventing apoptosis (136). Hepatitis C virus (**HCV**) curtails apoptosis by inducing cellular expression of Parkin and PINK1, which are key mediators of mitophagy, resulting in perinuclear mitochondrial clustering (137).

We hypothesize that NoV may also utilize mitophagy to prevent apoptosis. In the mitophagy-induced pathway of apoptotic inhibition, clustered mitochondria (along with NA, RCs, and perhaps virus particles in the presence of the RNA2 genome segment) would be packaged into mitophagosomes that are somehow prevented from fusing with lysosomes to form mature autolysosomes so that NoV RCs are not cleared from the cell. In future work that is beyond the scope of this dissertation project, we will use biochemical and immunofluorescence assays to determine whether expression of NA induces mitophagy and desensitizes mammalian cells to apoptotic stimuli. We predict that the clustered mitochondria (and NA) will co-localize with mitophagosomal markers in cells that are expressing NA. We also predict these cells will be resistant to apoptotic stimuli like UV irradiation. This result would suggest that the NoV RdRp is inhibiting apoptosis by inducing mitophagy or the related process of autophagy.

NoV would also benefit from autophagy or mitophagy as a mechanism to exit infected cells without cell lysis, as shown for picornaviruses (258). Evidence that we now interpret as suggesting a role for autophagy in NoV particle release was provided by Murphy *et al.* (1970), who showed the presence of NoV particles inside of double-membrane vesicles in the cytoplasm of Kupffer cells in the livers of NoV-infected mice

(174); these structures exhibit morphology reminiscent of autophagosomes. We propose to examine this in the future by selectively isolating autophagosomes using differential centrifugation and analyzing the contents for NA and RNA replication products. These experiments will help us determine whether autophagy or mitophagy assists in the avoidance of apoptosis by NoV or in release of NoV particles from infected cells.

Drp1 plays a role in apoptosis by hyper-fragmenting mitochondria. In light of our results from Chapter 1, we hypothesize that NoV also prevents apoptosis by blocking Drp1's pro-apoptotic mitochondrial fission activity. Drp1 mediated mitochondrial hyper-fragmentation promotes cell death by expediting the release of proapoptotic factors from the mitochondria (21). This process also relies on Drp1 SUMOylation, Drp1 translocation to the OMM and Drp1-induced mitochondrial fission (70, 254, 281). Therefore, inhibiting Drp1 may be a bimodal mechanism by NoV to ensure progeny production.

4.3 The NoV RdRp interferes with mitochondrial dynamics, possibly by disrupting Drp1 and mitochondrial fission. The clustered mitochondrial morphology in cells expressing NA also resembles that seen in viral systems where mitochondrial dynamics are disrupted (136) or in cells with inhibited Drp1 function (240). Interestingly, Drp1 is also involved in apoptosis, where it has enhanced activity that results in rapid fragmentation of mitochondria. When Drp1 activity is inhibited, cytochrome c release from the mitochondria is blocked, which delays apoptosis (70, 237, 239). The advantages of inhibiting mitochondrial fission may be manifold for NoV. Our current data establish the clustered mitochondria as the sites of RC formation and RNA synthesis

(Reference (84) and **Chapter 2**), and we hypothesize that mitochondrial clustering may also serve as a mechanism for NoV to inhibit apoptosis, thereby increasing the successful completion of its replicative cycle and production of progeny virions.

Drp1 activity is regulated by SUMO1 modification in the cytoplasm, which induces Drp1 to translocate to the OMM. If the SUMO1 moiety on Drp1 is removed, Drp1 will dissociate from the OMM. Our preliminary observation that NA contained several consensus SUMOylation sites was intriguing because SUMOylation is an important PTM of mitochondrial proteins and also controls mitochondrial morphology. We initially hypothesized that NA is SUMOylated may outcompetes Drp1 for SUMO1 interaction, thereby inhibiting mitochondrial fission by preventing Drp1 from being SUMOylated. Our results thus far have not yet allowed us to determine definitively whether or not NA is covalently SUMOylated in cultured mammalian cells. The immunoprecipitation (**IP**) experiments in which we precipitate protein complexes with anti-SUMO1 antibodies and Western blot with anti-HA and detect WT NA (**Figures 29 and 30**) support the hypothesis that NA is SUMOylated. Similarly, our preliminary data further supports this interpretation: the amount of NA detected by this procedure is reduced when we use a triple K-to-A NA mutant that alters the acceptor lysine residue in all three predicted consensus SUMOylation sites in NA (**Figure 30**).

In contrast, the IP experiments where we precipitate protein complexes with anti-HA and Western blot with anti-SUMO1 antibodies, suggest that no detectable SUMOylated species of NA were present in these samples (**Figure 28**). Additionally, NA detected in both of these experimental procedures was found to migrate in SDS-PAGE at the approximate molecular mass of unmodified NA, further complicating our

interpretation of these results. It is possible that a small proportion of NA is SUMOylated but it is below the detection limits of our assay. Indeed, the SUMOylated forms of many cellular proteins represents a small fraction (often 5%) of the total population of these proteins due to the abundance of SUMO-specific proteases, which can make detecting SUMOylated substrates difficult using these methods (40, 62, 188, 288).

A number of other viral proteins are known to interact with the SUMO pathway (71) and a possible alternative interpretation of these results would be that a small population of SUMOylated NA interacts or forms complexes with a larger population of unmodified NA. We observe high-molecular weight complexes containing substantial amounts of NA by non-denaturing PAGE followed by Western blotting (Gant and Johnson, unpublished observation), which suggests that the NoV RdRp is likely to form oligomers such as those seen for the RdRps of poliovirus and HCV (108, 193, 242, 279). Perhaps our IP's are detecting large networks of unmodified NA in complexes with SUMOylated NA that could be co-immunoprecipitated with our anti-SUMO1 antibody. This would explain our observation that the form of NA that co-immunoprecipitated was detected at the unmodified NA molecular mass (115 kDa). It remains to be determined whether NA oligomerization is a consequence of SUMOylation and/or SUMO1-mediated protein-protein interactions stimulating RdRp oligomerization. Clearly, it will require the more sensitive method of mass spectrometry to definitively determine whether NA is covalently SUMOylated, which is beyond the scope of this doctoral dissertation.

Nevertheless, our ability to co-IP abundant amounts of NA with anti-SUMO antibodies suggested the intriguing possibility that NA may also interact non-covalently with SUMO1 or a SUMO1-containing protein. The results of a subsequent bioinformatic

analysis predicted the presence of a C-terminal SUMO-interacting motif (**SIM**) at residues 953-956 (VLRV) on NA; similar SIMs mediate non-covalent interactions between SUMO and other proteins (161, 191). Our proposed experiments to mutate the predicted SIM and test the effect on our ability to co-IP NA with anti-SUMO1 antibodies may help elucidate the potential role of such a non-covalent protein-protein interaction in the NoV life cycle.

Regardless of whether NA is covalently SUMOylated or interacts with either SUMO1 or a SUMOylated protein via the predicted SIM, we hypothesize the NoV RdRp acts as an antagonist of Drp1-mediated mitochondrial fission by outcompeting Drp1 for its interaction with SUMO1, thereby disrupting SUMOylation of Drp1 and leading to inhibition of its function in mitochondrial fission. Since SUMOylation of Drp1 results in its translocation from the cytoplasm to the mitochondrial membrane, we examined its localization in the absence and presence of NA. Our immunofluorescence confocal microscopy results suggest that NA may inhibit Drp1 translocation (**Figures 33 and 34**). The cytoplasmic subcellular appearance exhibited by Drp1 in untransfected cells (**Figure 33**) is altered when NA is expressed in mammalian cells (**Figure 34**). Specifically, Drp1's normal clustered appearance in the cytoplasm is lost when NA is expressed and fails to co-localize with NA at the mitochondria. Although our quantitation of co-localization between Drp1 and NA in this sample shows 62% of Drp1 co-localizing with NA, this does not reflect true co-localization between the two proteins. In this sample, NA has a clustered appearance at a discrete location in the cytoplasm and Drp1 has a diffuse cytoplasmic appearance. The 62% OC reflects the fact that the two proteins are sharing overlapping space in the cytoplasm rather than actually co-

localizing, as evidenced by the Drp1 staining when imaged sectionally on the Z-axis. Nevertheless, the normal clustered cytoplasmic localization of Drp1 is lost, suggesting that Drp1 localization and presumably translocation (which we define as increased interaction with mitochondrial membranes over time) has been altered (**Figure 34**).

Future experiments are designed to determine whether 1) Drp1 SUMOylation is reduced or inhibited during NA expression (a prerequisite for its translocation and an essential element to the current version of our hypothesis), 2) Drp1 localization changes over time (a hallmark of active translocation), and 3) NA disrupts Drp1 mitochondrial membrane association. All of these completed and planned experiments focus on inhibition of fission as contributing to the clustered mitochondrial morphology in the presence of NA. However, it remains possible that this morphology could also be promoted by an increase in the fusion side of mitochondrial dynamics. The question of whether NoV also affects mitochondrial fusion has loomed since the onset of this study. Future experiments will analyze whether mitochondrial fusion is also affected in cells expressing NA.

4.4 The NoV RdRp may antagonize Drp1 activity by binding SUMO1 and preventing mitochondrial fission. At this point our data suggest the following non-mutually exclusive scenarios: **i)** NA is covalently SUMOylated at one of its three predicted SUMO consensus motifs, but the levels of SUMOylated NA are too low to be detected by Western blot, **ii)** NA interacts with SUMO1 non-covalently via a SIM, and/or **iii)** NA interacts with the SUMO1 moiety from another SUMOylated protein, also via its SIM. In all three scenarios, or in any combination of the three, the NoV RdRp has the potential to compete with Drp1 for SUMO1 by interacting with SUMO1 in a complex and

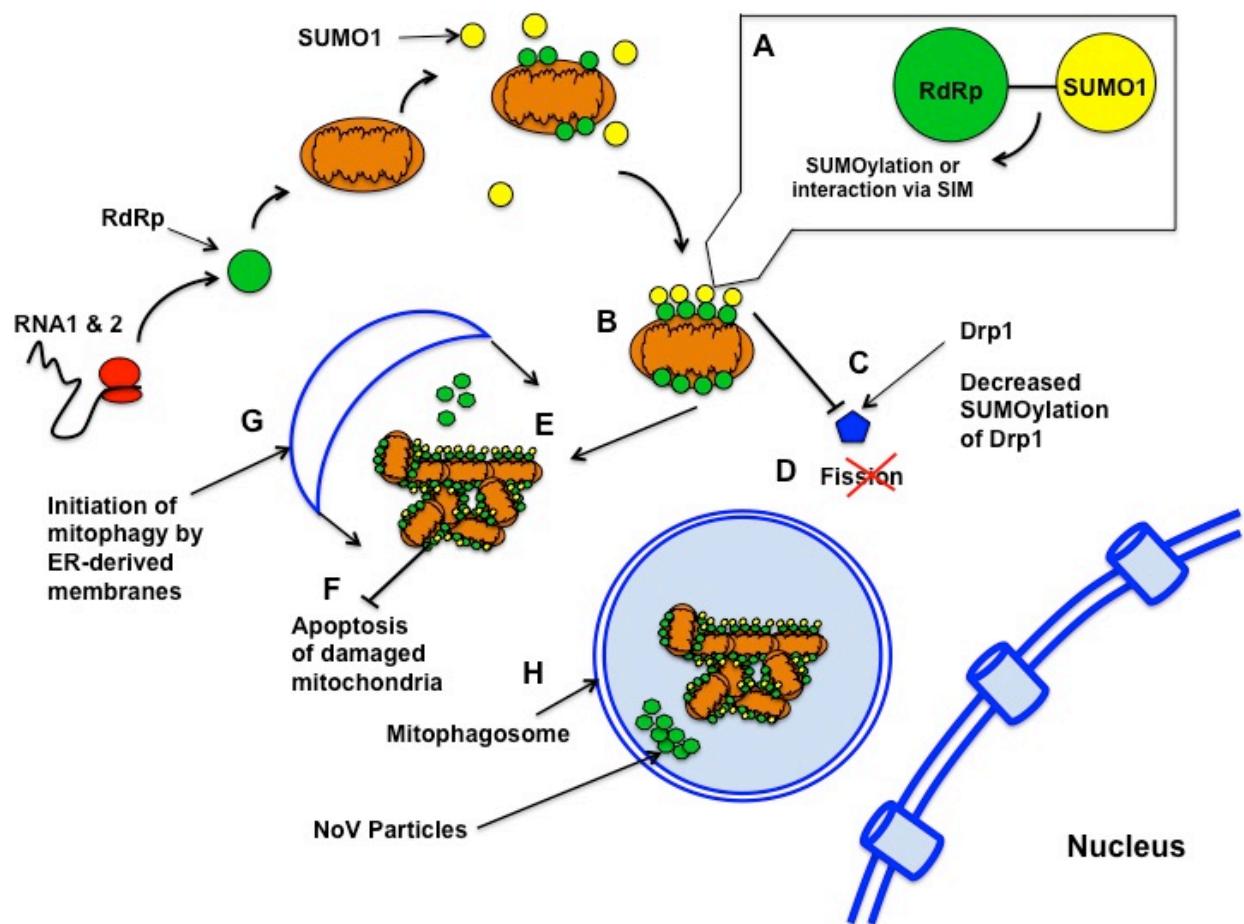
occupying the modifier, thereby preventing it from being conjugated to Drp1. Alternatively, NA may interact with the SUMO1 moiety on SUMOylated Drp1 after it translocates to the OMM, which may ensnare Drp1 stopping it from committing to mitochondrial fission – eloping with NA. NA may bind and hold SUMO1-Drp1 until SENP5 deSUMOylates Drp1 freeing it from NA to return to the cytoplasm (298, 299). Whether the residual SUMO1 moiety stays bound to NA's SIM or is released remains to be determined. The affinity NA binds SUMO1 will need to be addressed in future experiments using a SUMO binding assay or a competitive SUMO binding assay *in vitro* using purified NA, Drp1, and SUMO1. This preliminary result provides insight into a potential mechanism of how NoV might disrupt mitochondrial fission during RNA RC formation in mammalian cells.

We hypothesize that the mitochondrial clustering proceeds via the following speculative model (**Figure 36**). RNA1 is used as an mRNA for synthesis of NA protein, which anchors to the outer leaflet of the OMM via its N-terminal MARs. We have shown that synthesis of progeny RNA by NA requires this association with the OMM (**Figure 22 and 23**). To initiate RNA1 synthesis, NA recognizes and binds to its 3' end and synthesizes a negative-strand RNA1 replication intermediate. The observation that the ratio of positive-to-negative strands is approximately 100:1 for NoV might suggest that NA could have a higher affinity for negative strand RNA1 or perhaps for a structural element within this RNA strand than for the positive strand. Synthesis of positive-sense RNA1 from the negative strand intermediate will provide more NA mRNA for translation, resulting in increased NA protein levels.

As increasing concentrations of NA associate with the OMM, SUMO1 interacts with NA either by SUMOylation, SIM-mediated interactions, or both (**Figure 36A**). As NA accumulates at the OMM, the number of NA-SUMO1 interactions increase and results in reduced levels of unassociated SUMO1 proximal to the OMM. RCs containing NA, viral RNA, SUMO1 and other yet to be determined proteins begin to form on the surface of individually affected mitochondria (**Figure 36B**). Our co-IP results and the observation that the subcellular localization of cytoplasmic SUMO1 is altered when NA is expressed are indicative of an affinity between NA and SUMO1.

The model predicts that NA and SUMO1 interact to such an extent that Drp1 SUMOylation is blocked due to the lack of free SUMO available to be conjugated to Drp1 (**Figure 36C**). Without SUMO1 conjugation, translocation of Drp1 to the OMM is consequently inhibited or reduced, leading to disruption of Drp1 activity and decreased fission, evidenced by the accumulation of the clustered form. We hypothesize that by approximately 8 hpt, individual mitochondria organelles cluster as a result of normal rates of mitochondrial fusion but cannot be severed by Drp1-mediated fission (**Figure 36D**). By this time after NA expression, we predict that mitochondrial clustering increases concomitantly with progressive inhibition of Drp1 SUMOylation (and subsequent fission) to such an extent that it becomes detectable by microscopy (**Figure 36E and Figure 16, panel B**). By 24 hpt virtually all of the mitochondria have clustered, Drp1 localization is now exclusively cytoplasmic, and mitochondrial fission has stopped. At this point, NA has effectively shut down SUMO1-dependent Drp1-mediated mitochondrial fission. This speculative model brings together our preliminary results as well as those shown in detail in this dissertation. Further experimentation will

Figure 36: A hypothetical model of inhibition of mitochondrial fission by the NoV RdRp. Our predicted model for NoV RC formation and mitochondrial clustering begins with the accumulation of NA on the surface of individual mitochondria. **A)** NA and SUMO1 interact at the OMM either by SUMOylation of NA, non-covalent protein-protein interaction between SUMO1 and NA at its predicted SIM, or both. **B)** The number of NA-SUMO1 interactions increase at the OMM resulting in a substantial amount of NA-SUMO1 heterogenic complexes. **C)** The affinity between NA and SUMO1 is great enough to deprive Drp1 of SUMOylation, resulting in inhibition of Drp1 mitochondrial fission. **D)** The decrease in mitochondrial fission by Drp1 results in mitochondrial clustering over time that maximizes at 24 hpt. **E)** The clustered mitochondria serve as the sites of NoV RC formation and **F)** a mode for NoV to inhibit mitochondrial apoptosis. **G)** Mitophagy is induced either by the cell or NoV and begins to enclose the clustered mitochondria in double membrane structures (174). **H)** The mitophagosomes encapsulate clustered mitochondria (RCs) and NoV particles (when RNA2 is present). The mitophagosomes are hypothesized to inhibit mitochondrial apoptosis by preventing the release of apoptotic factors, and to serve as a release mechanism for NoV by exocytosis of the virus-packed mitophagosomes.



be required to confirm or expand upon this hypothetical model, which seeks to explain the mechanism by which NoV RC formation occurs in mammalian cells.

This two-pronged activity of Drp1 antagonism (for RC formation and inhibition of apoptosis activation) would lead to cellular and biochemical phenotypes we already observed with NoV infection or NA expression. Specifically, the lack of CPE and visual apoptotic morphology (14), persistent integrity of the HA epitope tag on NA suggesting a lack of caspase 3 activation (reference (84); **Figure 15**), and a protracted time course of NoV RNA replication in infected mammalian cells (124) suggest NoV inhibits apoptosis. Possibly, NoV induces mitophagy, which would explain the peculiar perinuclear localization of the mitochondrial clusters and contribute to averted apoptotic processes associated with dysfunctional mitochondria (**Figure 36G and H**). Whether this mitophagy occurs by viral induction or is initiated by the cell remains to be determined.

4.5 Concluding remarks. Taken together, our results may shed new light on the mechanism by which NoV causes pathogenesis in infected mammals and insects. NoV replicates in the musculature of the lower back and hind limbs of suckling mice and suckling hamsters, leading to flaccid paralysis of the hind limbs and death (87, 174, 222). Similarly, viral replication in the muscle tissues of greater wax moth (*Galleria mellonella*) larvae results in fatal paralysis of the hind segments (86-88). In infected muscle cells from mice and *G. mellonella* larvae, the mitochondria were observed to cluster around the perinuclear region and, late in infection, exhibited altered architecture. Strikingly, the tissues exhibited progressive disorganization of the muscle fibers and fibrils, as the mitochondria became altered and the cells filled with paracrystalline arrays of progeny viral particles (87). It has been previously

hypothesized that the paralysis seen in these animals is a result of this disruption of the muscle fibrils by altered mitochondria (86-88).

Our results support the hypothesis that the tissue damage caused by NoV infection is the result of interaction between the RdRp and the OMM. This interaction causes clustering of mitochondria into large networks, thereby reorganizing a vital dynamic organelle - all secondary effects of NoV RC formation. The work described in this dissertation establishes a basis for further characterization of the interaction between the NoV RdRp and cellular factors in cultured mammalian cells, leading to formation of viral RCs on the OMM. Furthermore, this dissertation contributes to elucidating the strategic genome replication mechanisms used by other positive-strand RNA viruses for localization of RdRps and other viral nonstructural proteins to membranes and establishment of RCs. We are in the process of further characterizing the mechanisms by which mitochondrial dynamics are involved in the NoV replication cycle.

Our data has potentially opened up a new realm of nodavirus protein A-host interactions and highlights the complexity of these deceptively simple viruses. The model we have developed for NoV RC formation will be addressed in future experiments and underscores the importance of a virus's ability to optimize its genome by encoding complex proteins with manifold function. To the human senses, a virus's ability to simplify biology appears complex and paradoxical – encoding its existence in entirety and anticipating its host in as minimal a message as possible.

References

1. Adkins S, Stawicki SS, Faurote G, Siegel RW, Kao CC (1998) Mechanistic analysis of RNA synthesis by RNA-dependent RNA polymerase from two promoters reveals similarities to DNA-dependent RNA polymerase. *RNA* 4:455-470
2. Ahlquist P, French R, Janda M, Loesch-Fries LS (1984) Multicomponent RNA plant virus infection derived from cloned viral cDNA. *Proc Natl Acad Sci U S A* 81:7066-7070
3. Ahlquist P, Janda M (1984) cDNA cloning and in vitro transcription of the complete brome mosaic virus genome. *Mol Cell Biol* 4:2876-2882
4. Ahlquist P, Noueiry AO, Lee W-M, Kushner DB, Dye BT (2003) Host factors in positive-strand RNA virus genome replication. *J Virol* 77:8181-8186
5. Ahola T, Karlin DG (2015) Sequence analysis reveals a conserved extension in the capping enzyme of the alphavirus supergroup, and a homologous domain in nodaviruses. *Biology direct* 10:16
6. Albarino CG, Price BD, Eckerle LD, Ball LA (2001) Characterization and template properties of RNA dimers generated during *Flock House virus* RNA replication. *Virology* 289:269-282
7. Albarino CG, Eckerle LD, Ball LA (2003) The *cis*-acting replication signal at the 3' end of *Flock House virus* RNA2 is RNA3-dependent. *Virology* 311:181-191
8. Arcier JM, Herman F, Lightner DV, Redman RM, Mari J, Bonami JR (1999) A viral disease associated with mortalities in hatchery-reared postlarvae of the giant freshwater prawn *Macrobrachium rosenbergii*. *Diseases of Aquatic Organisms* 38:177-181
9. Athanassopoulou F, Billinis C, Psychas V, Karipoglou K (2003) Viral encephalopathy and retinopathy of *Dicentrarchus labrax* (L.) farmed in fresh water in Greece. *J Fish Dis* 26:361-365
10. Ausubel FM, Brent R, Kingston RE, Moore DD, Seidman JG, Smith JA, Struhl K (1994) *Current Protocols in Molecular Biology*. John Wiley & Sons, Inc., Somerset, NJ

11. Bailey L, Scott HA (1973) The pathogenicity of *Nodamura virus* for insects. *Nature* 241:545
12. Bailey L, Newman JFE, Porterfield JS (1975) The multiplication of *Nodamura virus* in insect and mammalian cell cultures. *J Gen Virol* 26:15-20
13. Ball LA (1992) Cellular expression of a functional nodavirus RNA replicon from *vaccinia virus* vectors. *J Virol* 66:2335-2345
14. Ball LA, Amann JM, Garrett BK (1992) Replication of *Nodamura virus* after transfection of viral RNA into mammalian cells in culture. *J Virol* 66:2326-2334
15. Ball LA (1994) Nodaviruses. In: Webster RG, Granoff A (eds) *Encyclopedia of Virology*. Academic Press Ltd., London, pp 919-925
16. Ball LA (1994) Replication of the genomic RNA of a positive-strand RNA animal virus from negative-sense transcripts. *Proc Natl Acad Sci USA* 91:12443-12447
17. Ball LA (1995) Requirements for the self-directed replication of *Flock House virus* RNA 1. *J Virol* 69:720-727
18. Ball LA, Johnson KL (1998) Nodaviruses of insects. In: Miller LK, Ball LA (eds) *The Insect Viruses*. Plenum Publishing Corporation, New York, pp 225-267
19. Ball LA, Johnson KL (1999) Reverse genetics of nodaviruses. *Adv Virus Res* 53:229-244
20. Ball LA (2001) Replication strategies of RNA viruses. In: Fields BN, Knipe DM, Howley PM, Griffin DE (eds) *Fields' Virology*. Lippincott, Williams and Wilkens, Philadelphia
21. Benard G, Karbowski M (2009) Mitochondrial fusion and division: Regulation and role in cell viability. *Seminars in cell & developmental biology* 20:365-374
22. Bienz K, Bienz-Isler G, Egger D, Weiss M, Loeffler H (1970) *Coxsackie virus* infection in skeletal muscles of mice. An electron microscopic study. II. Appearance and fate of virus progeny. *Arch ges Virusforsch* 31:257-265

23. Bienz K, Egger D, Rasser Y, Bossart W (1983) Intracellular distribution of poliovirus proteins and the induction of virus-specific cytoplasmic structures. *Virology* 131:39-48
24. Bienz K, Egger D, Pasamontes L (1987) Association of polioviral proteins of the P2 genomic region with the viral replication complex and virus-induced membrane synthesis as visualized by electron microscopic immunocytochemistry and autoradiography. *Virology* 160:220-226
25. Bienz K, Egger D, Troxler M, Pasamontes L (1990) Structural organization of poliovirus RNA replication is mediated by viral proteins of the P2 genomic region. *J Virol* 64:1156-1163
26. Bienz K, Egger D, Pfister T, Troxler M (1992) Structural and functional characterization of the *poliovirus* replication complex. *J Virol* 66:2740-2747
27. Bienz K, Egger D, Pfister T (1994) Characteristics of the *poliovirus* replication complex. *Arch Virol Suppl* 9:147-157
28. Bienz-Isler G, Bienz K, Weiss M, Loeffler H (1970) *Coxsackie virus* infection in skeletal muscles of mice. An electron microscopic study. I. Cell- and nucleus alterations. *Arch ges Virusforsch* 31:247-256
29. Binesh CP, Renuka K, Malaichami N, Greeshma C (2013) First report of viral nervous necrosis-induced mass mortality in hatchery-reared larvae of clownfish, *Amphiprion sebae* Bleeker. *J Fish Dis* 36:1017-1020
30. Bloch B, Gravningen K, Larsen JL (1991) Encephalomyelitis among turbot associated with a picornavirus-like agent. *Dis Aquat Organ* 10:65-70
31. Bonami JR, Shi Z, Qian D, Sri Widada J (2005) White tail disease of the giant freshwater prawn, *Macrobrachium rosenbergii*: separation of the associated virions and characterization of MrNV as a new type of nodavirus. *J Fish Dis* 28:23-31
32. Bovo G, Nishizawa T, Maltese C, Borghesan F, Mutinelli F, Montesi F, De Mas S (1999) Viral encephalopathy and retinopathy of farmed marine fish species in Italy. *Virus Res* 63:143-146

33. Brachmann CB, Davies A, Cost GJ, Caputo E, Li J, Hieter P, Boeke JD (1998) Designer deletion strains derived from *Saccharomyces cerevisiae* S288C: a useful set of strains and plasmids for PCR-mediated gene disruption and other applications. *Yeast* 14:115-132
34. Braschi E, Zunino R, McBride HM (2009) MAPL is a new mitochondrial SUMO E3 ligase that regulates mitochondrial fission. *EMBO Rep* 10:748-754
35. Breitbart M, Rohwer F (2005) Here a virus, there a virus, everywhere the same virus? *Trends in microbiology* 13:278-284
36. Breuil G, Bonami J-R, Pepin JF, Pichot Y (1991) Viral infection (picorna-like virus) associated with mass mortalities in hatchery-reared sea-bass (*Dicentrarchus labrax*) larvae and juveniles. *Aquaculture* 97:109-116
37. Brown-Bryan TA, Leoh LS, Ganapathy V, Pacheco FJ, Mediavilla-Varela M, Filippova M, Linkhart TA, Gijssbers R, Debyser Z, Casiano CA (2008) Alternative splicing and caspase-mediated cleavage generate antagonistic variants of the stress oncoprotein LEDGF/p75. *Molecular cancer research : MCR* 6:1293-1307
38. Buchan DW, Ward SM, Lobley AE, Nugent TC, Bryson K, Jones DT (2010) Protein annotation and modelling servers at University College London. *Nucleic Acids Res* 38:W563-568
39. Buchholz UJ, Finke S, Conzelmann K-K (1999) Generation of *bovine respiratory syncytial virus* (BRSV) from cDNA: BRSV NS2 is not essential for virus replication in tissue culture, and the human RSV leader region acts as a functional BRSV genome promoter. *J Virol* 73:251-259
40. Bueno MTD, Garcia-Rivera JA, Kugelman JR, Morales E, Rosas-Acosta G, Llano M (2010) SUMOylation of the lens epithelium-derived growth factor/p75 attenuates its transcriptional activity on the heat shock protein 27 promoter. *J Mol Biol* 399:221-239
41. Burgyan J, Rubino L, Russo M (1996) The 5'-terminal region of a tombusvirus genome determines the origin of multivesicular bodies. *J Gen Virol* 77 (Pt 8):1967-1974

42. Chang CR, Blackstone C (2010) Dynamic regulation of mitochondrial fission through modification of the dynamin-related protein Drp1. *Annals of the New York Academy of Sciences* 1201:34-39
43. Chen H, Detmer SA, Ewald AJ, Griffin EE, Fraser SE, Chan DC (2003) Mitofusins Mfn1 and Mfn2 coordinately regulate mitochondrial fusion and are essential for embryonic development. *J Cell Biol* 160:189-200
44. Chen H, Chan DC (2009) Mitochondrial dynamics--fusion, fission, movement, and mitophagy--in neurodegenerative diseases. *Human molecular genetics* 18:R169-176
45. Chen L-J, Su Y-C, Hong J-R (2009) Betanodavirus non-structural protein B1: A novel anti-necrotic death factor that modulates cell death in early replication cycle in fish cells. *Virology* 385:444-454
46. Chen S-P, Yang H-L, Her GM, Lin H-Y, Jeng M-F, Wu J-L, Hong J-R (2006) Betanodavirus induces phosphatidylserine exposure and loss of mitochondrial membrane potential in secondary necrotic cells, both of which are blocked by bongkreikic acid. *Virology* 347:379-391
47. Chen S-P, Wu J-L, Su Y-C, Hong J-R (2007) Anti-Bcl-2 family members, zfBcl-x(L) and zfMcl-1a, prevent cytochrome c release from cells undergoing betanodavirus-induced secondary necrotic cell death. *Apoptosis* 12:1043-1060
48. Chen SP, Yang HL, Lin HY, Chen MC, Wu JL, Hong JR (2006) Enhanced viability of a nervous necrosis virus-infected stable cell line over-expressing a fusion product of the zfBcl-xL and green fluorescent protein genes. *J Fish Dis* 29:347-354
49. Cherif N, Thiery R, Castric J, Biacchesi S, Bremont M, Thabti F, Limem L, Hammami S (2009) Viral encephalopathy and retinopathy of *Dicentrarchus labrax* and *Sparus aurata* farmed in Tunisia. *Vet Res Commun* 33:345-353
50. Chua FHC, Loo JJ, Wee JY (1995) Mass mortality in juvenile greasy grouper, *Epinephelus tauvina*, associated with vacuolating encephelopathy and retinopathy. *Diseases in Asian aquaculture II Fish Health Section*, Asian Fisheries Society, Manila:235-241

51. Claros MG, von Heijne G (1994) TopPred II: an improved software for membrane protein structure predictions. *Comput Appl Biosci* 10:685-686
52. Combet C, Blanchet C, Geourjon C, Deleage G (2000) NPS@: network protein sequence analysis. *Trends in biochemical sciences* 25:147-150
53. Comps M, Pepin JF, Bonami J-R (1994) Purification and characterization of two fish encephalitis viruses (FEV) infecting *Lates calcarifer* and *Dicentrarchus labrax*. *Aquaculture* 123:1-10
54. Cuchet D, Sykes A, Nicolas A, Orr A, Murray J, Sirma H, Heeren J, Bartelt A, Everett RD (2011) PML isoforms I and II participate in PML-dependent restriction of HSV-1 replication. *J Cell Sci* 124:280-291
55. Cusack S (1999) RNA-protein complexes. *Curr Opin Struct Biol* 9:66-73
56. Cutrin JM, Dopazo CP, Thiery R, Leao P, Oliveira JG, Barja JL, Bandin I (2007) Emergence of pathogenic betanodaviruses belonging to the SJNNV genogroup in farmed fish species from the Iberian Peninsula. *J Fish Dis* 30:225-232
57. Dasgupta R, Selling B, Rueckert R (1994) *Flock House virus*: a simple model for studying persistent infection in cultured *Drosophila* cells. *Arch Virol Suppl* 9:121-132
58. Dasmahapatra B, Dasgupta R, Saunders K, Selling B, Gallagher T, Kaesberg P (1986) Infectious RNA derived from transcription from cloned cDNA copies of the genomic RNA of an insect virus. *Proc Natl Acad Sci USA* 83:63-66
59. Delettre C, Lenaers G, Griffoin JM, Gigarel N, Lorenzo C, Belenguer P, Pelloquin L, Grosgeorge J, Turc-Carel C, Perret E, Astarie-Dequeker C, Lasquelléc L, Arnaud B, Ducommun B, Kaplan J, Hamel CP (2000) Nuclear gene OPA1, encoding a mitochondrial dynamin-related protein, is mutated in dominant optic atrophy. *Nat Genet* 26:207-210
60. den Boon JA, Ahlquist P (2010) Organelle-like membrane compartmentalization of positive-strand RNA virus replication factories. *Annu Rev Microbiol* 64:241-256
61. Denison MR (2008) Seeking membranes: positive-strand RNA virus replication complexes. *PLoS Biol* 6:e270

62. Desterro JM, Rodriguez MS, Hay RT (1998) SUMO-1 modification of I κ B α inhibits NF- κ B activation. *Mol Cell* 2:233-239
63. Di Franco A, R. Kuzmickas, N. G. Anderson and D. J. Spiro (1984) Ultrastructure and origin of cytoplasmic multivesicular bodies induced by carnation italian ringspot virus. *J Gen Virol* 65:1233-1237
64. Djikeng A, Kuzmickas R, Anderson NG, Spiro DJ (2009) Metagenomic analysis of RNA viruses in a fresh water lake. *PloS one* 4:e7264
65. Dosztanyi Z, Csizmek V, Tompa P, Simon I (2005) IUPred: web server for the prediction of intrinsically unstructured regions of proteins based on estimated energy content. *Bioinformatics* 21:3433-3434
66. Dosztanyi Z, Csizmek V, Tompa P, Simon I (2005) The pairwise energy content estimated from amino acid composition discriminates between folded and intrinsically unstructured proteins. *J Mol Biol* 347:827-839
67. Draper DE (1999) Themes in RNA-protein recognition. *J Mol Biol* 293:255-270
68. Eckerle LD, Ball LA (2002) Replication of the RNA segments of a bipartite viral genome is coordinated by a transactivating subgenomic RNA. *Virology* 296:165-176
69. Eckerle LD, Albarino CG, Ball LA (2003) *Flock House virus* subgenomic RNA3 is replicated and its replication correlates with transactivation of RNA2. *Virology* 317:95-108
70. Estaquier J, Arnoult D (2007) Inhibiting Drp1-mediated mitochondrial fission selectively prevents the release of cytochrome c during apoptosis. *Cell Death Differ* 14:1086-1094
71. Everett RD, Boutell C, Hale BG (2013) Interplay between viruses and host sumoylation pathways. *Nature reviews Microbiology* 11:400-411
72. Figueroa-Romero C, Iniguez-Lluhi JA, Stadler J, Chang C-R, Arnoult D, Keller PJ, Hong Y, Blackstone C, Feldman EL (2009) SUMOylation of the mitochondrial fission protein Drp1 occurs at multiple nonconsensus sites within the B domain and is linked to its activity cycle. *FASEB J* 23:3917-3927

73. Finkbeiner SR, Allred AF, Tarr PI, Klein EJ, Kirkwood CD, Wang D (2008) Metagenomic analysis of human diarrhea: viral detection and discovery. PLoS Pathog 4:e1000011
74. Finn RD, Bateman A, Clements J, Coggill P, Eberhardt RY, Eddy SR, Heger A, Hetherington K, Holm L, Mistry J, Sonnhammer EL, Tate J, Punta M (2014) Pfam: the protein families database. Nucleic Acids Res 42:D222-230
75. Flanagan JB, Petterson RF, Ambros V, Hewlett NJ, Baltimore D (1977) Covalent linkage of a protein to a defined nucleotide sequence at the 5'-terminus of virion and replicative intermediate RNAs of poliovirus. Proc Natl Acad Sci U S A 74:961-965
76. Frerichs GN, Morgan D, Hart D, Skerrow C, Roberts RJ, Onions DE (1991) Spontaneously productive C-type retrovirus infection of fish cell lines. J Gen Virol 72 (Pt 10):2537-2539
77. Friesen P, Scotti P, Longworth J, Rueckert R (1980) *Black beetle virus*: propagation in *Drosophila* line 1 cells and an infection-resistant subline carrying endogenous *black beetle virus*-related particles. J Virol 35:741-747
78. Froshauer S, Kartenbeck J, Helenius A (1988) Alphavirus RNA replicase is located on the cytoplasmic surface of endosomes and lysosomes. J Cell Biol 107:2075-2086
79. Fuerst TR, Niles EG, Studier FW, Moss B (1986) Eukaryotic transient-expression system based on recombinant *vaccinia virus* that synthesizes bacteriophage T7 RNA polymerase. Proc Natl Acad Sci USA 83:8122-8126
80. Fujiki Y, Hubbard AL, Fowler S, Lazarow PB (1982) Isolation of intracellular membranes by means of sodium carbonate treatment: application to endoplasmic reticulum. J Cell Biol 93:97-102
81. Gallagher TM, Friesen PD, Rueckert RR (1983) Autonomous replication and expression of RNA1 from *black beetle virus*. J Virol 46:481-489
82. Gallagher TM (1987) Synthesis and assembly of nodaviruses. University of Wisconsin - Madison

83. Gallagher TM, Rueckert RR (1988) Assembly-dependent maturation cleavage in provirions of a small icosahedral insect ribovirus. *J Virol* 62:3399-3406
84. Gant VU, Jr., Moreno S, Varela-Ramirez A, Johnson KL (2014) Two membrane-associated regions within the Nodamura virus RNA-dependent RNA polymerase are critical for both mitochondrial localization and RNA replication. *J Virol* 88:5912-5926
85. Gareau JR, Lima CD (2010) The SUMO pathway: emerging mechanisms that shape specificity, conjugation and recognition. *Nat Rev Mol Cell Biol* 11:861-871
86. Garzon S, Charpentier G, Kurstak E (1978) Morphogenesis of the *Nodamura virus* in the larvae of the Lepidopteran *Galleria mellonella* (L.). *Arch Virol* 56:61-76
87. Garzon S, Strykowski H, Charpentier G (1990) Implication of mitochondria in the replication of *Nodamura virus* in larvae of the Lepidoptera, *Galleria mellonella* (L.) and in suckling mice. *Arch Virol* 113:165-176
88. Garzon S, Charpentier G (1991) *Nodaviridae*. In: Adams JR, Bonami JR (eds) *Atlas of Invertebrate Viruses*. CRC Press, Boca Raton (USA), pp 351-370
89. Gehrke R, Ecker M, Aberle SW, Allison SL, Heinz FX, Mandl CW (2003) Incorporation of tick-borne encephalitis virus replicons into virus-like particles by a packaging cell line. *J Virol* 77:8924-8933
90. Geiss-Friedlander R, Melchior F (2007) Concepts in sumoylation: a decade on. *Nat Rev Mol Cell Biol* 8:947-956
91. Gietz RD, Sugino A (1988) New yeast-*Escherichia coli* shuttle vectors constructed with *in vitro* mutagenized yeast genes lacking six-base pair restriction sites. *Gene* 74:527-534
92. Gitlin L, Hagai T, LaBarbera A, Solovey M, Andino R (2014) Rapid evolution of virus sequences in intrinsically disordered protein regions. *PLoS Pathog* 10:e1004529
93. Gomes R, Guerra-Sa R, Arruda E (2010) Coxsackievirus B5 induced apoptosis of HeLa cells: effects on p53 and SUMO. *Virology* 396:256-263

94. Gopal R, Venter PA, Schneemann A (2014) Differential segregation of nodaviral coat protein and RNA into progeny virions during mixed infection with FHV and NoV. *Virology* 454-455:280-290
95. Gorbalenya AE, Pringle FM, Zeddarn J-L, Luke BT, Cameron CE, Kalkmakoff J, Hanzlik TN, Gordon KHJ, Ward VK (2002) The palm subdomain-based active site is internally permuted in viral RNA-dependent RNA polymerases of an ancient lineage. *J Mol Biol* 324:47-62
96. Graham JM (2001) Isolation of mitochondria from tissues and cells by differential centrifugation. *Current protocols in cell biology* / editorial board, Juan S Bonifacino [et al] Chapter 3:Unit 3 3
97. Graham JM (2002) Preparation of crude subcellular fractions by differential centrifugation. *TheScientificWorldJournal* 2:1638-1642
98. Graham JM (2002) Homogenization of mammalian cultured cells. *TheScientificWorldJournal* 2:1630-1633
99. Grandemange S, Herzig S, Martinou JC (2009) Mitochondrial dynamics and cancer. *Seminars in cancer biology* 19:50-56
100. Greenwood LK, Moore NF (1982) The purification and partial characterization of a small RNA-virus from *Lymantria* - the identification of a *Nodamura*-like virus. *Microbiolo* 5:49-52
101. Grimley PM, Berezesky IK, Friedman RM (1968) Cytoplasmic structures associated with an arbovirus infection: loci of viral ribonucleic acid synthesis. *J Virol* 2:1326-1338
102. Grotmol S, Totland GK, Thorud K, Hjeltne BK (1997) Vacuolating encephalopathy and retinopathy associated with a nodavirus-like agent: a probable cause of mass mortality of cultured larval and juvenile Atlantic halibut *Hippoglossus hippoglossus*. *Dis Aquat Organ* 29:85-97
103. Guarino LA, Kaesberg P (1981) Isolation and characterization of an RNA-dependent RNA polymerase from *black beetle virus*-infected *Drosophila melanogaster* cells. *J Virol* 40:379-386

104. Guarino LA, Ghosh A, Dasmahapatra B, Dasgupta R, Kaesberg P (1984) Sequence of the *black beetle virus* subgenomic RNA and its location in the viral genome. *Virology* 139:199-203
105. Guo K, Lu J, Huang Y, Wu M, Zhang L, Yu H, Zhang M, Bao Y, He JC, Chen H, Jia W (2015) Protective Role of PGC-1 α in Diabetic Nephropathy Is Associated with the Inhibition of ROS through Mitochondrial Dynamic Remodeling. *PloS one* 10:e0125176
106. Guo YX, Chan S-W, Kwang J (2004) Membrane association of *greasy grouper nervous necrosis virus* protein A and characterization of its mitochondrial localization targeting signal. *J Virol* 78:6498-6508
107. Hall AR, Burke N, Dongworth RK, Hausenloy DJ (2014) Mitochondrial fusion and fission proteins: novel therapeutic targets for combating cardiovascular disease. *British journal of pharmacology* 171:1890-1906
108. Hansen JL, Long AM, Schultz SC (1997) Structure of the RNA-dependent RNA polymerase of poliovirus. *Structure* 5:1109-1122
109. Harder Z, Zunino R, McBride HM (2004) Sumo1 conjugates mitochondrial substrates and participates in mitochondrial fission. *Curr Biol* 14:340-345
110. Harper TA (1994) Characterization of the proteins encoded from the nodaviral subgenomic RNA. University of Wisconsin - Madison
111. Haukenes G, Szilvay AM, Brokstad KA, Kanestrom A, Kalland KH (1997) Labeling of RNA transcripts of eukaryotic cells in culture with BrUTP using a liposome transfection reagent (DOTAP). *Biotechniques* 22:308-312
112. Hegde A, Teh HC, Lam TJ, Sin YM (2003) Nodavirus infection in freshwater ornamental fish, guppy, *Poicelia reticulata* - comparative characterization and pathogenicity studies. *Arch Virol* 148:575-586
113. Hendry DA (1991) Nodaviridae of Invertebrates. In: Kurstak E (ed) *Viruses of Invertebrates*. Marcel Dekker, Inc., New York, pp 227-276
114. Hill JE, Myers AM, Koerner TJ, Tzagoloff A (1986) Yeast/*E. coli* shuttle vectors with multiple unique restriction sites. *Yeast* 2:163-167

115. Hirokawa T, Boon-Chieng S, Mitaku S (1998) SOSUI: classification and secondary structure prediction system for membrane proteins. *Bioinformatics* 14:378-379
116. Hofmann K, Stoffel W (1993) TMBASE - A database of membrane spanning protein segments. *Biol Chem Hoppe-Seyler*, p 166
117. Hosur MV, Schmidt T, Tucker RC, Johnson JE, Selling BH, Rueckert RR (1984) *Black beetle virus*-crystallization and particle symmetry. *Virology* 133:119-127
118. Hosur MV, Schmidt T, Tucker RC, Johnson JE, Gallagher TM, Selling BH, Rueckert RR (1987) Structure of an insect virus at 3.0 angstrom resolution. *Proteins: Struct Funct Genet* 2:167-176
119. Ingberman E, Perkins EM, Marino M, Mears JA, McCaffery JM, Hinshaw JE, Nunnari J (2005) Dnm1 forms spirals that are structurally tailored to fit mitochondria. *J Cell Biol* 170:1021-1027
120. International Committee on Taxonomy of Viruses., King AMQ (2012) *Virus taxonomy : classification and nomenclature of viruses : ninth report of the International Committee on Taxonomy of Viruses*. Academic Press, London ; Waltham, MA
121. Janda M, Ahlquist P (1993) RNA-dependent replication, transcription, and persistence of *brome mosaic virus* RNA replicons in *S. cerevisiae*. *Cell* 72:961-970
122. Jardin C, Horn AH, Sticht H (2015) Binding properties of SUMO-interacting motifs (SIMs) in yeast. *Journal of molecular modeling* 21:2597
123. Johnson KL, Ball LA (1999) Induction and maintenance of autonomous *Flock House virus* RNA1 replication. *J Virol* 73:7933-7942
124. Johnson KL, Price BD, Ball LA (2003) Recovery of infectivity from cDNA clones of *Nodamura virus* and identification of small nonstructural proteins. *Virology* 305:436-451

125. Johnson KL, Price BD, Eckerle LD, Ball LA (2004) *Nodamura virus* nonstructural protein B2 can enhance viral RNA accumulation in both mammalian and insect cells. J Virol 78:6698-6704
126. Johnson KN, Zeddam J-L, Ball LA (2000) Characterization and construction of functional cDNA clones of *Pariacoto virus*, the first *alphanodavirus* isolated outside Australasia. J Virol 74:5123-5132
127. Johnson KN, Ball LA (2001) Recovery of infectious *Pariacoto virus* from cDNA clones and identification of susceptible cell lines. J Virol 75:12220-12227
128. Johnson KN, Johnson KL, Dasgupta R, Gratsch T, Ball LA (2001) Comparisons among the larger genome segments of six nodaviruses and their encoded RNA replicases. J Gen Virol 82:1855-1866
129. Johnson KN, Ball LA (2003) Virions of *Pariacoto virus* contain a minor protein translated from the second AUG codon of the capsid protein open reading frame. J Gen Virol 84:2847-2852
130. Johnson KN, Tang L, Johnson JE, Ball LA (2004) Heterologous RNA encapsidated in *Pariacoto virus*-like particles forms a dodecahedral cage similar to genomic RNA in wild-type virions. J Virol 78:11371-11378
131. Jonczyk M, Pathak KB, Sharma M, Nagy PD (2007) Exploiting alternative subcellular location for replication: tombusvirus replication switches to the endoplasmic reticulum in the absence of peroxisomes. Virology 362:320-330
132. Jones S, Thornton JM (1995) Protein-protein interactions: a review of protein dimer structures. Progress in biophysics and molecular biology 63:31-65
133. Jones S, Thornton JM (1996) Principles of protein-protein interactions. Proc Natl Acad Sci U S A 93:13-20
134. Karbowski M, Neutzner A (2012) Neurodegeneration as a consequence of failed mitochondrial maintenance. Acta neuropathologica 123:157-171
135. Kim S, Kim HY, Lee S, Kim SW, Sohn S, Kim K, Cho H (2007) Hepatitis B virus x protein induces perinuclear mitochondrial clustering in microtubule- and Dynein-dependent manners. J Virol 81:1714-1726

136. Kim SJ, Khan M, Quan J, Till A, Subramani S, Siddiqui A (2013) Hepatitis B virus disrupts mitochondrial dynamics: induces fission and mitophagy to attenuate apoptosis. PLoS Pathog 9:e1003722
137. Kim SJ, Syed GH, Siddiqui A (2013) Hepatitis C virus induces the mitochondrial translocation of Parkin and subsequent mitophagy. PLoS Pathog 9:e1003285
138. Kirkegaard K (2009) Subversion of the cellular autophagy pathway by viruses. Current topics in microbiology and immunology 335:323-333
139. Kokawa Y, Takami I, Nishizawa T, Yoshimizu M (2008) A mixed infection in sevenband grouper *Epinephelus septemfasciatus* affected with viral nervous necrosis (VNN). Aquaculture 284:41-45
140. Kolesar P, Sarangi P, Altmannova V, Zhao X, Krejci L (2012) Dual roles of the SUMO-interacting motif in the regulation of Srs2 sumoylation. Nucleic Acids Res 40:7831-7843
141. Kopek BG, Perkins G, Miller DJ, Ellisman MH, Ahlquist P (2007) Three-dimensional analysis of a viral RNA replication complex reveals a virus-induced mini-organelle. PLoS Biol 5:e220
142. Kopek BG, Settles EW, Friesen PD, Ahlquist P (2010) Nodavirus-induced membrane rearrangement in replication complex assembly requires replicase protein a, RNA templates, and polymerase activity. J Virol 84:12492-12503
143. Koshiba T, Detmer SA, Kaiser JT, Chen H, McCaffery JM, Chan DC (2004) Structural basis of mitochondrial tethering by mitofusin complexes. Science 305:858-862
144. Kyte J, Doolittle RF (1982) A simple method for displaying the hydropathic character of a protein. J Mol Biol 157:105-132
145. Laemmli UK (1970) Cleavage of structural proteins during the assembly of the head of *bacteriophage T4*. Nature 227:680-685
146. Larkin MA, Blackshields G, Brown NP, Chenna R, McGettigan PA, McWilliam H, Valentin F, Wallace IM, Wilm A, Lopez R, Thompson JD, Gibson TJ, Higgins DG (2007) Clustal W and Clustal X version 2.0. Bioinformatics 23:2947-2948

147. Leeds P, Peltz SW, Jacobson A, Culbertson MR (1991) The product of the yeast UPF1 gene is required for rapid turnover of mRNAs containing a premature translational termination codon. *Genes Dev* 5:2303-2314
148. Li H, Li WX, Ding SW (2002) Induction and suppression of RNA silencing by an animal virus. *Science* 296:1319-1321
149. Li L, Victoria JG, Wang C, Jones M, Fellers GM, Kunz TH, Delwart E (2010) Bat guano virome: predominance of dietary viruses from insects and plants plus novel mammalian viruses. *J Virol* 84:6955-6965
150. Lin MT, Beal MF (2006) Mitochondrial dysfunction and oxidative stress in neurodegenerative diseases. *Nature* 443:787-795
151. Linding R, Russell RB, Neduva V, Gibson TJ (2003) GlobPlot: Exploring protein sequences for globularity and disorder. *Nucleic Acids Res* 31:3701-3708
152. Ling ML, Risman SS, Klement JF, McGraw N, McAllister WT (1989) Abortive initiation by bacteriophage T3 and T7 RNA polymerases under conditions of limiting substrate. *Nucleic Acids Res* 17:1605-1618
153. Liu C, Zhang J, Yi F, Wang J, Wang X, Jiang H, Xu J, Hu Y (2006) Isolation and RNA1 nucleotide sequence determination of a new insect nodavirus from *Pieris rapae* larvae in Wuhan city, China. *Virus Res* 120:28-35
154. Longworth JF, Carey GP (1976) A small RNA virus with a divided genome from *Heteronychus arator* (F.) [Coleoptera: Scarabaeidae]. *J Gen Virol* 33:31-40
155. Losomicronnn OC, Meng S, Ngo H, Liu R, Kaiser JT, Chan DC (2015) Crystal structure and functional analysis of MiD49, a receptor for the mitochondrial fission protein Drp1. *Protein science : a publication of the Protein Society*
156. Loson OC, Song Z, Chen H, Chan DC (2013) Fis1, Mff, MiD49, and MiD51 mediate Drp1 recruitment in mitochondrial fission. *Mol Biol Cell* 24:659-667
157. Lukic Z, Goff SP, Campbell EM, Arriagada G (2013) Role of SUMO-1 and SUMO interacting motifs in rhesus TRIM5alpha-mediated restriction. *Retrovirology* 10:10

158. Mackenzie JM, Jones MK, Young PR (1996) Immunolocalization of the dengue virus nonstructural glycoprotein NS1 suggests a role in viral RNA replication. *Virology* 220:232-240
159. Magliano D, Marshall JA, Bowden DS, Vardaxis N, Meanger J, Lee J-Y (1998) Rubella virus replication complexes are virus-modified lysosomes. *Virology* 240:57-63
160. Manders EMM, Verbeek FJ, Aten JA (1993) Measurement of Colocalization of Objects in Dual-Color Confocal Images. *J Microsc-Oxford* 169:375-382
161. Maroui MA, Kheddache-Atmane S, El Asmi F, Dianoux L, Aubry M, Chelbi-Alix MK (2012) Requirement of PML SUMO interacting motif for RNF4- or arsenic trioxide-induced degradation of nuclear PML isoforms. *PloS one* 7:e44949
162. Marshall D, Schneemann A (2001) Specific packaging of nodaviral RNA2 requires the N-terminus of the capsid protein. *Virology* 285:165-175
163. Matunis MJ, Coutavas E, Blobel G (1996) A novel ubiquitin-like modification modulates the partitioning of the Ran-GTPase-activating protein RanGAP1 between the cytosol and the nuclear pore complex. *J Cell Biol* 135:1457-1470
164. McBride HM, Neuspiel M, Wasiak S (2006) Mitochondria: more than just a powerhouse. *Curr Biol* 16:R551-R560
165. McGuffin LJ, Bryson K, Jones DT (2000) The PSIPRED protein structure prediction server. *Bioinformatics* 16:404-405
166. Mezeth KB, Nylund S, Henriksen H, Patel S, Nerland AH, Szilvay AM (2007) RNA-dependent RNA polymerase from Atlantic halibut nodavirus contains two signals for localization to the mitochondria. *Virus Res* 130:43-52
167. Miller DJ, Schwartz MD, Ahlquist P (2001) *Flock House virus* RNA replicates on outer mitochondrial membranes in *Drosophila* cells. *J Virol* 75:11664-11676
168. Miller DJ, Ahlquist P (2002) *Flock House virus* RNA polymerase is a transmembrane protein with amino-terminal sequences sufficient for mitochondrial localization and membrane insertion. *J Virol* 76:9856-9867

169. Miller S, Krijnse-Locker J (2008) Modification of intracellular membrane structures for virus replication. *Nature reviews Microbiology* 6:363-374
170. Miteva M, Keusekotten K, Hofmann K, Praefcke GJ, Dohmen RJ (2010) Sumoylation as a signal for polyubiquitylation and proteasomal degradation. *Sub-cellular biochemistry* 54:195-214
171. Mori K-i, Nakai T, Nagahara M, Muroga K, Mekuchi T, Kanno T (1991) A viral disease in hatchery-reared larvae and juveniles of redspotted grouper. *Gyobyo Kenkyu (Fish Pathol)* 26:209-210
172. Mori K-I, Nakai T, Muroga K, Arimoto M, Mushiake K, Furusawa I (1992) Properties of a new virus belonging to nodaviridae found in larval striped jack (*Pseudocaranx dentex*) with nervous necrosis. *Virology* 187:368-371
173. Munday BL, Langdon JS, Hyatt A, Humphrey JD (1992) Mass mortality associated with a viral-induced vacuolating encephalopathy and retinopathy of larval and juvenile barramundi, *Lates calcarifer* Bloch. *Aquaculture* 103:197-211
174. Murphy FA, Scherer WF, Harrison AK, Dunne HW, Gary GW, Jr. (1970) Characterization of *Nodamura virus*, an arthropod transmissible picornavirus. *Virology* 40:1008-1021
175. Nagai K (1996) RNA-protein complexes. *Curr Opin Struct Biol* 6:53-61
176. Neuspiel M, Schauss AC, Braschi E, Zunino R, Rippstein P, Rachubinski RA, Andrade-Navarro MA, McBride HM (2008) Cargo-selected transport from the mitochondria to peroxisomes is mediated by vesicular carriers. *Current biology : CB* 18:102-108
177. Newman JFE, Brown F (1973) Evidence for a divided genome in *Nodamura virus*, an arthropod-borne picornavirus. *J Gen Virol* 21:371-384
178. Newman JFE, Brown F (1976) Absence of poly(A) from the infective RNA of *Nodamura virus*. *J Gen Virol* 30:137-140
179. Newman JFE, Brown F (1977) Further physicochemical characterization of *Nodamura virus*. Evidence that the divided genome occurs in a single component. *J Gen Virol* 38:83-95

180. Newman JFE, Matthews T, Omilianowski DR, Salerno T, Kaesberg P, Rueckert R (1978) *In vitro* translation of the two RNAs of *Nodamura virus*, a novel mammalian virus with a divided genome. J Virol 25:78-85
181. Newman TC, Ohme-Takagi M, Taylor CB, Green PJ (1993) DST sequences, highly conserved among plant SAUR genes, target reporter transcripts for rapid decay in tobacco. Plant Cell 5:701-714
182. Nishizawa T, Mori K-i, Furuhashi M, Nakai T, Furusawa I, Muroga K (1995) Comparison of the coat protein genes of five fish nodaviruses, the causative agents of viral nervous necrosis in marine fish. J Gen Virol 76:1563-1569
183. Nishizawa T, Furuhashi M, Nagai T, Nakai T, Muroga K (1997) Genomic classification of fish nodaviruses by molecular phylogenetic analysis of the coat protein gene. Appl Environ Microbiol 63:1633-1636
184. Novoa RR, Calderita G, Arranz R, Fontana J, Granzow H, Risco C (2005) Virus factories: associations of cell organelles for viral replication and morphogenesis. Biology of the cell / under the auspices of the European Cell Biology Organization 97:147-172
185. Nunnari J, Marshall WF, Straight A, Murray A, Sedat JW, Walter P (1997) Mitochondrial transmission during mating in *Saccharomyces cerevisiae* is determined by mitochondrial fusion and fission and the intramitochondrial segregation of mitochondrial DNA. Mol Biol Cell 8:1233-1242
186. Okamoto T, Schwab RB, Scherer PE, Lisanti MP (2001) Analysis of the association of proteins with membranes. Current protocols in cell biology / editorial board, Juan S Bonifacino [et al] Chapter 5:Unit 5 4
187. Olichon A, Guillou E, Delettre C, Landes T, Arnaune-Pelloquin L, Emorine LJ, Mils V, Daloyau M, Hamel C, Amati-Bonneau P, Bonneau D, Reynier P, Lenaers G, Belenguer P (2006) Mitochondrial dynamics and disease, OPA1. Biochimica et biophysica acta 1763:500-509
188. Pal S, Rosas JM, Rosas-Acosta G (2010) Identification of the non-structural influenza A viral protein NS1A as a bona fide target of the Small Ubiquitin-like Modifier by the use of dicistronic expression constructs. J Virol Methods 163:498-504

189. Pal S, Santos A, Rosas JM, Ortiz-Guzman J, Rosas-Acosta G (2011) Influenza A virus interacts extensively with the cellular SUMOylation system during infection. *Virus Res* 158:12-27
190. Palmer CS, Elgass KD, Parton RG, Osellame LD, Stojanovski D, Ryan MT (2013) Adaptor proteins MiD49 and MiD51 can act independently of Mff and Fis1 in Drp1 recruitment and are specific for mitochondrial fission. *J Biol Chem* 288:27584-27593
191. Parker JL, Ulrich HD (2012) A SUMO-interacting motif activates budding yeast ubiquitin ligase Rad18 towards SUMO-modified PCNA. *Nucleic Acids Res* 40:11380-11388
192. Patel S, Korsnes K, Bergh O, Vik-Mo F, Pedersen J, Nerland AH (2007) Nodavirus in farmed Atlantic cod *Gadus morhua* in Norway. *Dis Aquat Organ* 77:169-173
193. Pathak HB, Ghosh SK, Roberts AW, Sharma SD, Yoder JD, Arnold JJ, Gohara DW, Barton DJ, Paul AV, Cameron CE (2002) Structure-function relationships of the RNA-dependent RNA polymerase from poliovirus (3Dpol). A surface of the primary oligomerization domain functions in capsid precursor processing and VPg uridylylation. *J Biol Chem* 277:31551-31562
194. Pelletier J, Sonenberg N (1988) Internal initiation of translation of eukaryotic mRNA directed by a sequence derived from poliovirus RNA. *Nature* 334:320-325
195. Perrotta AT, Been MD (1991) A pseudoknot-like structure required for efficient self-cleavage of *hepatitis delta virus* RNA. *Nature (London)* 350:434-436
196. Petty HR (2001) Overview of the physical state of proteins within cells. *Current protocols in cell biology* / editorial board, Juan S Bonifacino [et al] Chapter 5:Unit 5 1
197. Pich S, Bach D, Briones P, Liesa M, Camps M, Testar X, Palacin M, Zorzano A (2005) The Charcot-Marie-Tooth type 2A gene product, Mfn2, up-regulates fuel oxidation through expression of OXPHOS system. *Human molecular genetics* 14:1405-1415
198. Price BD, Ball LA, Johnson KL Unpublished observation.

199. Price BD, Rueckert RR, Ahlquist P (1996) Complete replication of an animal virus and maintenance of expression vectors derived from it in *Saccharomyces cerevisiae*. *Proc Natl Acad Sci USA* 93:9465-9470
200. Price BD, Roeder M, Ahlquist P (2000) DNA-directed expression of functional *Flock House virus* RNA1 derivatives in *Saccharomyces cerevisiae*, heterologous gene expression, and selective effects on subgenomic mRNA synthesis. *J Virol* 74:11724-11733
201. Price BD, Ahlquist P, Ball LA (2002) DNA-directed expression of an animal virus RNA for replication-dependent colony formation in *Saccharomyces cerevisiae*. *J Virol* 76:1610-1616
202. Price BD, Eckerle LD, Ball LA, Johnson KL (2005) *Nodamura virus* RNA replication in *Saccharomyces cerevisiae*: heterologous gene expression allows replication-dependent colony formation. *J Virol* 79:495-502
203. Qiu Y, Cai D, Qi N, Wang Z, Zhou X, Zhang J, Hu Y (2011) Internal initiation is responsible for synthesis of Wuhan nodavirus subgenomic RNA. *J Virol* 85:4440-4451
204. Qiu Y, Wang Z, Liu Y, Qi N, Miao M, Si J, Xiang X, Cai D, Hu Y, Zhou X (2013) Membrane association of Wuhan nodavirus protein A is required for its ability to accumulate genomic RNA1 template. *Virology* 439:140-151
205. Racaniello VR, Baltimore D (1981) Cloned poliovirus complementary DNA is infectious in mammalian cells. *Science* 214:916-919
206. Ranjith-Kumar CT, Sarisky RT, Gutshall L, Thomson M, Kao CC (2004) De novo initiation pocket mutations have multiple effects on hepatitis C virus RNA-dependent RNA polymerase activities. *J Virol* 78:12207-12217
207. Ransangan J, Manin BO (2010) Mass mortality of hatchery-produced larvae of Asian seabass, *Lates calcarifer* (Bloch), associated with viral nervous necrosis in Sabah, Malaysia. *Vet Microbiol* 145:153-157
208. Ransangan J, Manin BO, Abdullah A, Roli Z, Sharudin EF (2011) Betanodavirus infection in golden pompano, *Trachinotus blochii*, fingerlings cultured in deep-sea cage culture facility in Langkawi, Malaysia. *Aquaculture* 315:327-334

209. Reinganum C, Bashiruddin JB, Cross GF (1985) *Boolarra virus*: a member of the *Nodaviridae* isolated from *Oncopera intricoides* (Lepidoptera: Hepialidae). Intervirology 24:10-17
210. Ren J, Gao X, Jin C, Zhu M, Wang X, Shaw A, Wen L, Yao X, Xue Y (2009) Systematic study of protein sumoylation: Development of a site-specific predictor of SUMOsp 2.0. Proteomics 9:3409-3412
211. Reshi ML, Su YC, Hong JR (2014) RNA Viruses: ROS-Mediated Cell Death. Int J Cell Biol 2014:467452
212. Roskopf JJ, Upton III JH, Rodarte L, Romero TA, Leung M-Y, Taufer M, Johnson KL (2010) A 3' terminal stem-loop structure in Nodamura virus RNA2 forms an essential cis-acting signal for RNA replication. Virus research 150:12-21
213. Rubino L, Russo M (1998) Membrane targeting sequences in tombusvirus infections. Virology 252:431-437
214. Russo M, Martelli GP (1972) Ultrastructural observations on tomato bushy stunt virus in plant cells. Virology 49:122-129
215. Russo M, Di Franco A, Martelli GP (1983) The fine structure of Cymbidium ringspot virus infections in host tissues. III. Role of peroxisomes in the genesis of multivesicular bodies. Journal of ultrastructure research 82:52-63
216. Saks VA, Veksler VI, Kuznetsov AV, Kay L, Sikk P, Tiivel T, Tranqui L, Olivares J, Winkler K, Wiedemann F, Kunz WS (1998) Permeabilized cell and skinned fiber techniques in studies of mitochondrial function in vivo. Mol Cell Biochem 184:81-100
217. Salonen A, Ahola T, Kaariainen L (2005) Viral RNA replication in association with cellular membranes. Current topics in microbiology and immunology 285:139-173
218. Sambrook J, Russell DW (2001) Molecular cloning: a laboratory manual, Third edn. Cold Spring Harbor Laboratory Press, Cold Spring Harbor, New York
219. Saunders K, Kaesberg P (1985) Template-directed RNA polymerase from black beetle virus-infected *Drosophila melanogaster* cells. Virology 147:373-381

220. Scherer WF, Hurlbut HS (1967) *Nodamura virus* from Japan: a new and unusual arbovirus resistant to diethyl ether and chloroform. *Am J Epidemiol* 86:271-285
221. Scherer WF (1968) Variable results of sodium deoxycholate tests of *Nodamura virus*, an ether and chloroform resistant arbovirus. *Proc Soc Exptl Biol Med* 129:194-199
222. Scherer WF, Verna JE, Richter GW (1968) *Nodamura virus*, an ether- and chloroform-resistant arbovirus from Japan. Physical and biological properties, with ecologic observations. *Am J Trop Med Hyg* 17:120-128
223. Schlegel A, Kirkegaard K (1995) Cell Biology of Enterovirus Infection. In: Rotbart HA (ed) *Human Enterovirus Infections*. ASM Press, Washington, D.C., pp 135-154
224. Schlegel A, Giddings TH, Jr., Ladinsky MS, Kirkegaard K (1996) Cellular origin and ultrastructure of membranes induced during poliovirus infection. *J Virol* 70:6576-6588
225. Schneemann A, Zhong W, Gallagher TM, Rueckert RR (1992) Maturation cleavage required for infectivity of a nodavirus. *J Virol* 66:6728-6734
226. Schneemann A, Dasgupta R, Johnson JE, Rueckert RR (1993) Use of recombinant baculoviruses in synthesis of morphologically distinct viruslike particles of *Flock House virus*, a nodavirus. *J Virol* 67:2756-2763
227. Schneemann A, Gallagher TM, Rueckert RR (1994) Reconstitution of *Flock House* provirions: a model system for studying structure and assembly. *J Virol* 68:4547-4556
228. Schneemann A, Marshall D (1998) Specific encapsidation of nodavirus RNAs is mediated through the C terminus of capsid precursor protein alpha. *J Virol* 72:8738-8746
229. Schneemann A (2006) The structural and functional role of RNA in icosahedral virus assembly. *Annu Rev Microbiol* 60:51-67

230. Schwartz M, Chen J, Janda M, Sullivan M, den Boon J, Ahlquist P (2002) A positive-strand RNA virus replication complex parallels form and function of retrovirus capsids. *Mol Cell* 9:505-514.
231. Scorrano L, Liu D (2009) The SUMO arena goes mitochondrial with MAPL. *EMBO Rep* 10:694-696
232. Scotti PD, Dearing S, Mossop DW (1983) *Flock House virus*: a nodavirus isolated from *Costelytra zealandica* (White) (Coleoptera: Scarabaeidae). *Arch Virol* 75:181-189
233. Scotti PD, Fredericksen S (1987) *Manawatu virus*: a nodavirus isolated from *Costelytra zealandica* (white) (Coleoptera: Scarabaeidae). *Arch Virol* 97:85-92
234. Settles EW, Friesen PD (2008) Flock house virus induces apoptosis by depletion of Drosophila inhibitor-of-apoptosis protein DIAP1. *J Virol* 82:1378-1388
235. Shaw JG, Plaskitt KA, Wilson TM (1986) Evidence that tobacco mosaic virus particles disassemble contrtranslationally in vivo. *Virology* 148:326-336
236. Shaw JM, Nunnari J (2002) Mitochondrial dynamics and division in budding yeast. *Trends in cell biology* 12:178-184
237. Sheridan C, Martin SJ (2010) Mitochondrial fission/fusion dynamics and apoptosis. *Mitochondrion* 10:640-648
238. Shetty M, Maiti B, Shivakumar Santhosh K, Venugopal MN, Karunasagar I (2012) Betanodavirus of marine and freshwater fish: distribution, genomic organization, diagnosis and control measures. *Indian J Virol* 23:114-123
239. Smirnova E, Shurland DL, Ryazantsev SN, van der Bliek AM (1998) A human dynamin-related protein controls the distribution of mitochondria. *J Cell Biol* 143:351-358
240. Smirnova E, Griparic L, Shurland DL, van der Bliek AM (2001) Dynamin-related protein Drp1 is required for mitochondrial division in mammalian cells. *Mol Biol Cell* 12:2245-2256

- 241. Song BH, Yun SI, Choi YJ, Kim JM, Lee CH, Lee YM (2008) A complex RNA motif defined by three discontinuous 5-nucleotide-long strands is essential for Flavivirus RNA replication. *RNA* 14:1791-1813
- 242. Spagnolo JF, Rossignol E, Bullitt E, Kirkegaard K (2010) Enzymatic and nonenzymatic functions of viral RNA-dependent RNA polymerases within oligomeric arrays. *RNA* 16:382-393
- 243. Spector DH, Baltimore D (1974) Requirement of 3'-terminal poly(adenylic acid) for the infectivity of poliovirus RNA. *Proc Natl Acad Sci U S A* 71:2983-2987
- 244. Stapleford KA, Rapaport D, Miller DJ (2009) Mitochondrion-enriched anionic phospholipids facilitate flock house virus RNA polymerase membrane association. *J Virol* 83:4498-4507
- 245. Starkey WG, Ireland JH, Muir KF, Shinn AP, Richards RH, Ferguson HW (2000) Isolation of nodavirus from Scottish farmed halibut, *Hippoglossus hippoglossus* (L). *J Fish Dis* 23:419-422
- 246. Starkey WG, Ireland JH, Muir KF, Jenkins ME, Roy WJ, Richards RH, Ferguson HW (2001) Nodavirus infection in Atlantic cod and Dover sole in the UK. *Vet Rec* 149:179-181
- 247. Su B, Wang X, Bonda D, Perry G, Smith M, Zhu X (2010) Abnormal mitochondrial dynamics--a novel therapeutic target for Alzheimer's disease? *Molecular neurobiology* 41:87-96
- 248. Su B, Wang X, Zheng L, Perry G, Smith MA, Zhu X (2010) Abnormal mitochondrial dynamics and neurodegenerative diseases. *Biochimica et biophysica acta* 1802:135-142
- 249. Su Y-C, Wu J-L, Hong J-R (2009) Betanodavirus non-structural protein B2: A novel necrotic death factor that induces mitochondria-mediated cell death in fish cells. *Virology* 385:143-154
- 250. Su YC, Hong JR (2010) Betanodavirus B2 causes ATP depletion-induced cell death via mitochondrial targeting and complex II inhibition in vitro and in vivo. *J Biol Chem* 285:39801-39810

251. Sullivan CS, Ganem D (2005) A virus-encoded inhibitor that blocks RNA interference in mammalian cells. *J Virol* 79:7371-7379
252. Sumper M, Luce R (1975) Evidence for *de novo* production of self-replicating and environmentally adapted RNA structures by *bacteriophage Qb* replicase. *Proc Natl Acad Sci USA* 72:162-166
253. Tan C, Huang B, Chang SF, Ngoh GH, Munday BL, Chen SC, Kwang J (2001) Determination of the complete nucleotide sequences of RNA1 and RNA2 from *greasy grouper (Epinephelus tauvina) nervous necrosis virus*, Singapore strain. *J Gen Virol* 82:647-653
254. Tanaka A, Youle RJ (2008) A chemical inhibitor of DRP1 uncouples mitochondrial fission and apoptosis. *Mol Cell* 29:409-410
255. Tang KF, Pantoja CR, Redman RM, Lightner DV (2007) Development of in situ hybridization and RT-PCR assay for the detection of a nodavirus (PvNV) that causes muscle necrosis in *Penaeus vannamei*. *Dis Aquat Organ* 75:183-190
256. Tang L, Johnson KN, Ball LA, Lin T, Yeager M, Johnson JE (2001) The structure of *Pariacoto virus* reveals a dodecahedral cage of duplex RNA. *Nat Struct Biol* 8:77-83
257. Tang L, Lin CS, Krishna NK, Yeager M, Schneemann A, Johnson JE (2002) Virus-like particles of a fish nodavirus display a capsid subunit domain organization different from that of insect nodaviruses. *J Virol* 76:6370-6375
258. Taylor MP, Burgon TB, Kirkegaard K, Jackson WT (2009) Role of microtubules in extracellular release of poliovirus. *J Virol* 83:6599-6609
259. Tesh RB (1980) Infectivity and pathogenicity of *Nodamura virus* for mosquitoes. *J Gen Virol* 48:177-182
260. Thompson JD, Higgins DG, Gibson TJ (1994) CLUSTAL W: improving the sensitivity of progressive multiple sequence alignment through sequence weighting, position-specific gap penalties and weight matrix choice. *Nucleic Acids Res* 22:4673-4680

261. Tihova M, Dryden KA, Le T-vL, Harvey SC, Johnson JE, Yeager M, Schneemann A (2004) Nodavirus coat protein imposes dodecahedral RNA structure independent of nucleotide sequence and length. *J Virol* 78:2897-2905
262. Tsubuki S, Saito Y, Tomioka M, Ito H, Kawashima S (1996) Differential inhibition of calpain and proteasome activities by peptidyl aldehydes of di-leucine and tri-leucine. *J Biochem* 119:572-576
263. Ucko M, Colorni A, Diamant A (2004) Nodavirus infections in Israeli mariculture. *J Fish Dis* 27:459-469
264. Ulmanen I, Soderlund H, Kaariainen L (1976) Semliki Forest virus capsid protein associates with the 60S ribosomal subunit in infected cells. *J Virol* 20:203-210
265. Uo T, Dworzak J, Kinoshita C, Inman DM, Kinoshita Y, Horner PJ, Morrison RS (2009) Drp1 levels constitutively regulate mitochondrial dynamics and cell survival in cortical neurons. *Experimental neurology* 218:274-285
266. van der Meer Y, van Tol H, Locker JK, Snijder EJ (1998) ORF1a-encoded replicase subunits are involved in the membrane association of the arterivirus replication complex. *J Virol* 72:6689-6698
267. van der Meer Y, Snijder EJ, Dobbe JC, Schleich S, Denison MR, Spaan WJM, Locker JK (1999) Localization of mouse hepatitis virus nonstructural proteins and RNA synthesis indicates a role for late endosomes in viral replication. *J Virol* 73:7641-7657
268. Vander Heyden AB, Naismith TV, Snapp EL, Hanson PI (2011) Static retention of the luminal monotopic membrane protein torsinA in the endoplasmic reticulum. *EMBO J* 30:3217-3231
269. Vanderlaan M, Thomas CB (1985) Characterization of monoclonal antibodies to bromodeoxyuridine. *Cytometry* 6:501-505
270. Vendramin N, Patarnello P, Toffan A, Panzarin V, Cappellozza E, Tedesco P, Terlizzi A, Terregino C, Cattoli G (2013) Viral Encephalopathy and Retinopathy in groupers (*Epinephelus* spp.) in southern Italy: a threat for wild endangered species? *BMC Vet Res* 9:20

271. Venter PA, Schneemann A (2007) Assembly of two independent populations of flock house virus particles with distinct RNA packaging characteristics in the same cell. *J Virol* 81:613-619
272. Venter PA, Marshall D, Schneemann A (2009) Dual roles for an arginine-rich motif in specific genome recognition and localization of viral coat protein to RNA replication sites in flock house virus-infected cells. *J Virol* 83:2872-2882
273. Venter PA, Marshall D, Schneemann A (2009) Dual roles for an arginine-rich motif in specific genome recognition and localizing viral coat protein to RNA replication sites in Flock House virus-infected cells. *J Virol*
274. Verhoeven K, Claeys KG, Zuchner S, Schroder JM, Weis J, Ceuterick C, Jordanova A, Nelis E, De Vriendt E, Van Hul M, Seeman P, Mazanec R, Saifi GM, Szigeti K, Mancias P, Butler IJ, Kochanski A, Ryniewicz B, De Bleecker J, Van den Bergh P, Verellen C, Van Coster R, Goemans N, Auer-Grumbach M, Robberecht W, Milic Rasic V, Nevo Y, Tournev I, Guergueltcheva V, Roelens F, Vieregge P, Vinci P, Moreno MT, Christen HJ, Shy ME, Lupski JR, Vance JM, De Jonghe P, Timmerman V (2006) MFN2 mutation distribution and genotype/phenotype correlation in Charcot-Marie-Tooth type 2. *Brain : a journal of neurology* 129:2093-2102
275. Victoria JG, Kapoor A, Li L, Blinkova O, Slikas B, Wang C, Naeem A, Zaidi S, Delwart E (2009) Metagenomic analyses of viruses in stool samples from children with acute flaccid paralysis. *J Virol* 83:4642-4651
276. Vogt B, Hofmann K (2012) Bioinformatical detection of recognition factors for ubiquitin and SUMO. *Methods Mol Biol* 832:249-261
277. von Heijne G (1992) Membrane protein structure prediction. Hydrophobicity analysis and the positive-inside rule. *J Mol Biol* 225:487-494
278. Wang C, Youle RJ (2009) The role of mitochondria in apoptosis*. *Annual review of genetics* 43:95-118
279. Wang QM, Hockman MA, Staschke K, Johnson RB, Case KA, Lu J, Parsons S, Zhang F, Rathnachalam R, Kirkegaard K, Colacino JM (2002) Oligomerization and cooperative RNA synthesis activity of hepatitis C virus RNA-dependent RNA polymerase. *J Virol* 76:3865-3872

280. Wang X (2001) The expanding role of mitochondria in apoptosis. *Genes & development* 15:2922-2933
281. Wasiak S, Zunino R, McBride HM (2007) Bax/Bak promote sumoylation of DRP1 and its stable association with mitochondria during apoptotic cell death. *J Cell Biol* 177:439-450
282. Wery J-P, Reddy VS, Hosur MV, Johnson JE (1994) The refined three-dimensional structure of an insect virus at 2.8 Å resolution. *J Mol Biol* 235:565-586
283. Wu Q, Luo Y, Lu R, Lau N, Lai EC, Li WX, Ding SW (2010) Virus discovery by deep sequencing and assembly of virus-derived small silencing RNAs. *Proc Natl Acad Sci U S A* 107:1606-1611
284. Wu S-X, Kaesberg P (1991) Synthesis of template-sense, single-stranded *Flock House virus* RNA in a cell-free replication system. *Virology* 183:392-396
285. Wu S-X, Ahlquist P, Kaesberg P (1992) Active complete *in vitro* replication of nodavirus RNA requires glycerophospholipid. *Proc Natl Acad Sci USA* 89:11136-11140
286. Wu W, Wang Z, Xia H, Liu Y, Qiu Y, Liu Y, Hu Y, Zhou X (2014) Flock house virus RNA polymerase initiates RNA synthesis de novo and possesses a terminal nucleotidyl transferase activity. *PloS one* 9:e86876
287. Xue Y, Zhou F, Fu C, Xu Y, Yao X (2006) SUMOsp: a web server for sumoylation site prediction. *Nucleic Acids Res* 34:W254-257
288. Yamaguchi T, Sharma P, Athanasiou M, Kumar A, Yamada S, Kuehn MR (2005) Mutation of SENP1/SuPr-2 reveals an essential role for desumoylation in mouse development. *Mol Cell Biol* 25:5171-5182
289. Yeh ET (2009) SUMOylation and De-SUMOylation: wrestling with life's processes. *J Biol Chem* 284:8223-8227
290. Yoshikoshi K, Inoue K (1990) Viral nervous necrosis in hatchery-reared larvae and juveniles of Japanese parrotfish, *Oplegnathus fasciatus* (Temminck & Schlegel). *J Fish Dis* 13:69-77

291. Youle RJ (2005) Morphology of mitochondria during apoptosis: worms-to-beetles in worms. *Developmental cell* 8:298-299
292. Youle RJ, Narendra DP (2011) Mechanisms of mitophagy. *Nat Rev Mol Cell Biol* 12:9-14
293. Zeddiam J-L, Rodriguez JL, Ravallec M, Lagnaoui A (1999) A noda-like virus isolated from the sweetpotato pest *spodoptera eridania* (Cramer) (Lep.; noctuidae). *J Invertebr Pathol* 74:267-274
294. Zhong W, Dasgupta R, Rueckert R (1992) Evidence that the packaging signal for nodaviral RNA2 is a bulged stem-loop. *Proc Natl Acad Sci USA* 89:11146-11150
295. Zhong W, Rueckert RR (1993) *Flock House virus*: down-regulation of subgenomic RNA3 synthesis does not involve coat protein and is targeted to synthesis of its positive strand. *J Virol* 67:2716-2722
296. Zlotnick A (1994) Structural and biophysical characterization of *Nodamura virus*. Purdue University
297. Zorzano A, Liesa M, Sebastian D, Segales J, Palacin M (2010) Mitochondrial fusion proteins: dual regulators of morphology and metabolism. *Seminars in cell & developmental biology* 21:566-574
298. Zunino R, Schauss A, Rippstein P, Andrade-Navarro M, McBride HM (2007) The SUMO protease SENP5 is required to maintain mitochondrial morphology and function. *J Cell Sci* 120:1178-1188
299. Zunino R, Braschi E, Xu L, McBride HM (2009) Translocation of SenP5 from the nucleoli to the mitochondria modulates DRP1-dependent fission during mitosis. *J Biol Chem* 284:17783-17795

Glossary

ACNV	<i>Atlantic cod nervous necrosis virus</i>
ActD	Actinomycin D
AHNV	<i>Atlantic halibut nodavirus</i>
alb	<i>Anopheles albimanus</i> mosquito cell line
Amp	Ampicillin
ANV	American nodavirus
AP	Alkaline phosphatase
AP-61	<i>Aedes pseudoscutellaris</i> mosquito larvae cell line
ARM	Arginine-rich motif
ATP	Adenosine triphosphate
BBV	<i>Black beetle virus</i>
BFNNV	<i>Barfin flounder nervous necrosis virus</i>
BGNV	Bat guano-associated nodavirus GF-4
BHK21	Baby hamster (<i>Mesocricetus auratus</i>) kidney cell line
BMV	<i>Brome mosaic virus</i>
BoV	<i>Boolarra virus</i>
BrUTP	5-Bromouridine 5'-triphosphate
BSC40	<i>Cercopithecus aethiops</i> (monkey) kidney epithelial cell line
BSR-T7/5	Baby hamster (<i>Mesocricetus auratus</i>) kidney cell line that constitutively expresses T7 RNA polymerase in the cytoplasm
CAT	Chloramphenicol acetyl transferase
cDNA	Complementary DNA
CFTR	Cystic fibrosis transmembrane regulator
CHO	Chinese hamster ovary cell line
CNS	Central nervous system
Co-IP	Co-immunoprecipitation
COX3	Cytochrome c oxidase subunit III
CP	Coat protein
CPE	Cytopathic effect

C127	Mouse fibroblast cells
DAPI	4', 6-diamidino-2-phenylindole
DGNNV	<i>Dragon grouper nervous necrosis virus</i>
DIAP1	<i>Drosophila</i> inhibitor-of-apoptosis protein
DIEV	<i>Dicentrarcus labrax nervous necrosis virus</i>
DL1	<i>Drosophila</i> line 1 cell line
DMEM	Dulbecco's modified Eagle's medium
DNA	Deoxyribonucleic acid
Drp1	Dynamin-related protein 1
DTT	Dithiolthreitol
Δ	Deletion
EMCV	<i>Encephalomyocarditis virus</i>
ER	Endoplasmic reticulum
EtBr	Ethidium bromide
FA	<i>Flock house virus</i> protein A
FBS	Fetal bovine serum
FB33	<i>Helicoverpa zea</i> (Corn earworm) cell line
FHV	<i>Flock house virus</i>
Fis1	Mitochondrial fission protein 1
FITC	Fluorescein isothiocyanate
GFP	Green fluorescent protein
GF-1	Grouper cell line
GGNNV	<i>Greasy grouper nervous necrosis virus</i>
GL-av	Grouper liver cell line subcloned from grouper liver cell line GL-a
GNNV	<i>Guppy nervous necrosis virus</i>
GPL	Glycerophospholipid
G-418	Geneticin®, related to gentamicin analog of neomycin sulfate
HA	Influenza virus Hemagglutinin tag
HBV	<i>Hepatitis B virus</i>
HBx	<i>Hepatitis B virus</i> X protein
HCV	<i>Hepatitis C virus</i>
HD	High-density

HDV	<i>Hepatitis delta virus</i>
HEK 293T	Human embryonic kidney epithelial cell line
HeLa	Human epithelial adenocarcinoma cell line
HEp-2	Human epithelial cell line, HeLa contaminant
hpt	Hours post-transfection
HRP	Horseradish peroxidase
HR2	Heptad repeat region
[³H]	Tritium, radioactive hydrogen isotope
IBNNV	<i>Iberian betanodavirus</i>
IgG	Immunoglobulin type G
IMM	Inner mitochondrial membrane
IRES	Internal ribosomal entry site
JFNNV	<i>Japanese flounder nervous necrosis virus</i>
kDA	Kilodalton
LD	Low-density
LEDGF/p75	Lens epithelium-derived growth factor/p75
LNV	<i>Lymantria ninayi virus</i>
MAO	Monoamine oxidase
MAPL	Mitochondrial-associated protein ligase
MAR	Membrane-associated region
MCS	Multiple cloning site
MGNNV	<i>Malabaricus grouper nervous necrosis virus</i>
MgNNV	<i>Mouse grouper nervous necrosis virus</i>
MEM	Minimal essential medium
Mff	Mitochondrial fission factor
Mfn1/2	Mitofusins 1 and 2
MG132	Proteasome inhibitor
MiD49/51	49 and 51 kDa mitochondrial dynamics proteins
MMP	Mitochondrial membrane potential
MOS-55	<i>Anopheles gambiae</i> mosquito cell

	line
MTR	MitoTracker® Red CM-H ₂ XRos
MTS	Mitochondrial targeting sequence
MrNv	<i>Macrobrachium rosenbergii</i> <i>nodavirus</i>
MW	Molecular weight
MwV	<i>Manawatu virus</i>
NA	<i>Nodamura virus</i> protein A
NCS	Newborn calf serum
NEM	N-Ethylmaleimide
NoV	<i>Nodamura virus</i>
nt	Nucleotides
N1	Nodamura virus RNA1
N2	Nodamura virus RNA2
N3	Nodamura virus RNA3
OC	Overlap coefficient
OMM	Outer mitochondrial membrane
OPA1	Optic atrophy protein 1
ORF	Open reading frame
PaV	<i>Pariacoto virus</i>
PBS	Phosphate-buffered saline
PBS-T	Phosphate-buffered saline with Triton X-100
Pen-Strep	Penicillin-Streptomycin
PFA	Paraformaldehyde
PK15	Porcine kidney cell line
PMSF	Phenylmethylsulfonyl fluoride
PNL	Post-nuclear lysate
PTM	Post-translational modification
PVDF	Polyvinylidene fluoride
PvNV	<i>Penaeus vannamei nodavirus</i>
P20	20,000 x g pellet
P100	100,000 x g supernatant
[³²P]	Radioactive phosphorus isotope
RC	Replication complex
RdRp	RNA-dependent RNA polymerase
RGNNV	<i>Redspotted grouper nervous</i> <i>necrosis virus</i>
RNA	Ribonucleic acid
RNAi	RNA interference

RNase	Ribonuclease
ROI	Region of interest
ROS	Reactive oxygen species
rRNA	Ribosomal RNA
SAE1/UBA2	Heterodimeric SUMO activating enzyme 1 (E1)
SB	Sea bass
SBNNV	<i>Asian sea bass nervous necrosis virus</i>
SDS	Sodium dodecyl sulfate
SDS-PAGE	Sodium dodecyl sulfate gel electrophoresis
SENP	Sentrin-specific (SUMO-specific) protease
SGNNV	<i>Seven-band grouper nervous necrosis virus</i>
SIM	SUMO interacting motif
SJNNV	<i>Striped jack nervous necrosis virus</i>
Smac/DIABLO	Second mitochondria-derived binding protein with low pI
SP6	Bacteriophage SP6 (usu. reference SP6 RNA polymerase or its promoter element)
sTobRV	<i>Satellite tobacco ringspot virus</i>
SUMO	Small ubiquitin-like modifier
S20	20,000 x g supernatant
S100	100,000 x g supernatant
[³⁵S]	Radioactive sulfur isotope
TBS	Tris-buffered saline
TBS-T	Tris-buffered saline with tween 20
TGNNV	<i>Tiger grouper nervous necrosis virus</i>
TLR3	Toll-like receptor 3
TMD	Transmembrane domain
TNV	<i>Turbot nodavirus</i>
TPNNV	<i>Tiger puffer nervous necrosis virus</i>
TR	Texas Red
TRA-171	<i>Toxorhynchites</i> Mosquito larvae cell line
TX100	Triton X-100
Ubc9	SUMO E2 conjugating enzyme
USA	United States of America

UTR	Untranslated region
U₄	Four uracil bases in the 5' untranslated region of RNA1 segments for some alphaviruses
VER	Viral encephalopathy and retinopathy
Vero	African green monkey kidney cell line
VLP	Virus-like particle
VNN	Viral nervous necrosis
VPg	<i>Polio virus</i> genome-linked viral protein
WhNV	<i>Wuhan nodavirus</i>
WSNNV	<i>White snapper nervous necrosis virus</i>
WT	Wild type
α	Protein alpha
β	Protein beta
β-ME	2-mercaptoethanol
γ	Protein gamma
143B	Human bone osteosarcoma cell line

Appendix I: Phylogenetic Analysis of Family *Nodaviridae*

A1.1 Phylogenetic analysis of genomic RNA segments

Analysis of the degree of heterogeneity of full-length genomic RNA segments from 31 reported nodaviruses was performed as a means of updating the alignments to include all members of this virus family, including those described after publication of the most recent report. Multiple sequence alignment and phylogenetic analysis of genomic RNAs were performed using Clustal Omega and MEGA6, respectively (128). The inferred dendrograms were drawn using the maximum-likelihood method with 1000 bootstrap repetitions (**Figure 37 and 38** for RNA1 and RNA2, respectively). As expected, there is a clear divergence between the alpha- and betanodaviruses as seen for both RNA1 and RNA2 (**Figure 37 and 38**). The betanodaviruses share a high degree of RNA sequence identity (**Figure 40**) that is not seen with the alphanodaviruses (**Figure 38**), which results in the alphanodavirus genomic RNA sequences being more heterogeneous and having markedly lower sequence identity (**Figure 39**) compared to the betanodaviruses.

The shrimp nodaviruses share modest sequence identity with members of the *Nodaviridae*, but both shrimp viruses diverge from betanodaviruses in RNA2 sequence and group with NoV based on their RNA1 sequence (**Figure 37 and 38**). Additionally, the unclassified fish nodaviruses group with the betanodaviruses, which could lead to further expansion of this genus. Interestingly, both genomic segments of WhNV were grouped with the betanodavirus clade even though it was isolated from insect larvae (**Figures 36 and 37**). The tendency of an individual nodaviral sequence to drift between genera is uncommon, however it has been observed previously that the RNA1

Figure 37: Phylogeny among the alpha- and betanodavirus RNA1 segments. Multiple sequence alignments were performed using Clustal Omega. Phylogenetic analysis was performed using the maximum-likelihood method and unrooted trees were drawn using MEGA6. The bootstrap values are represented as percentages of 1000 resamplings. Representative members of each genera are marked with symbols **filled diamond**) NoV, alphanodaviruses, **open diamond**) SJNNV, betanodaviruses.

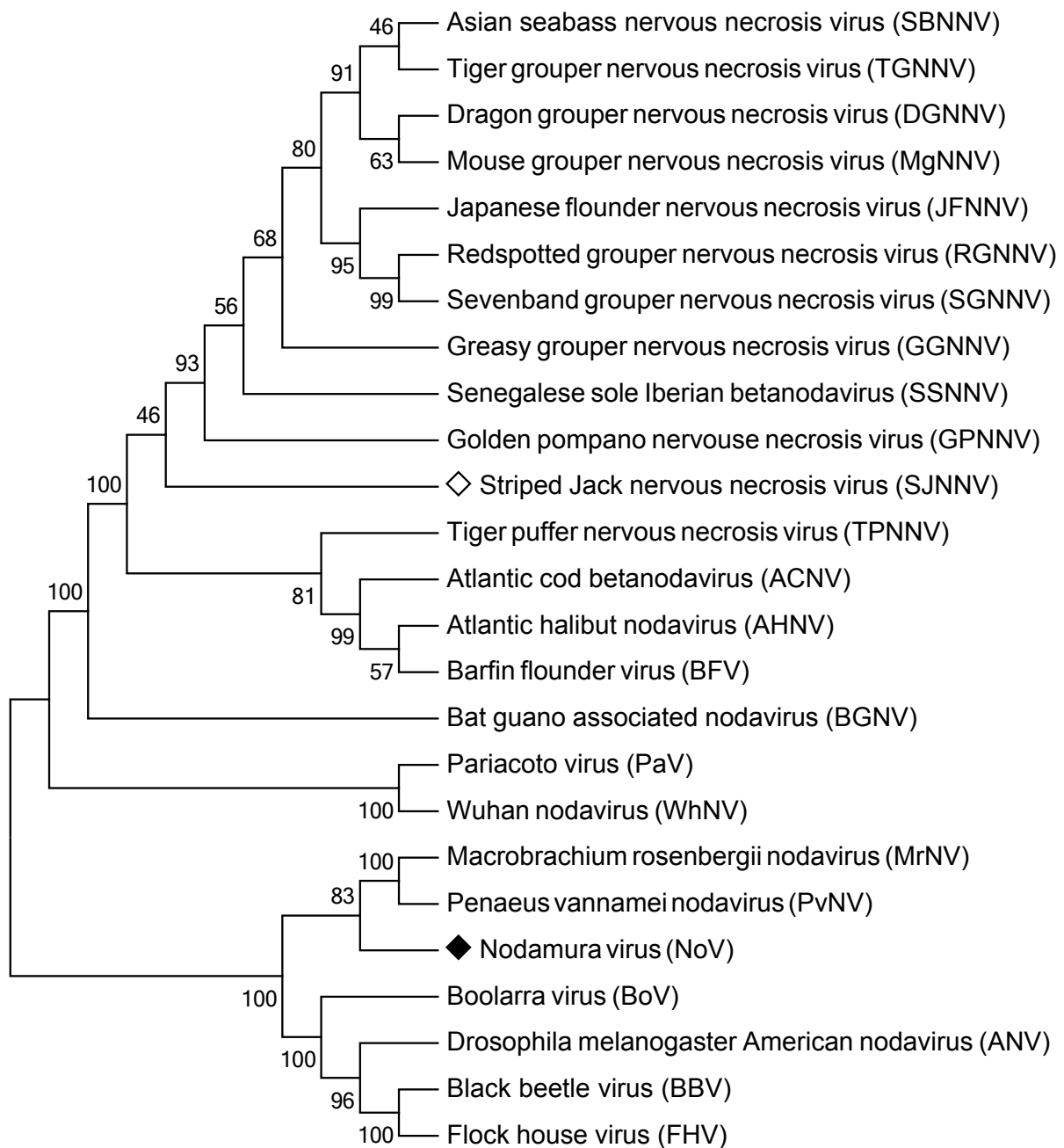
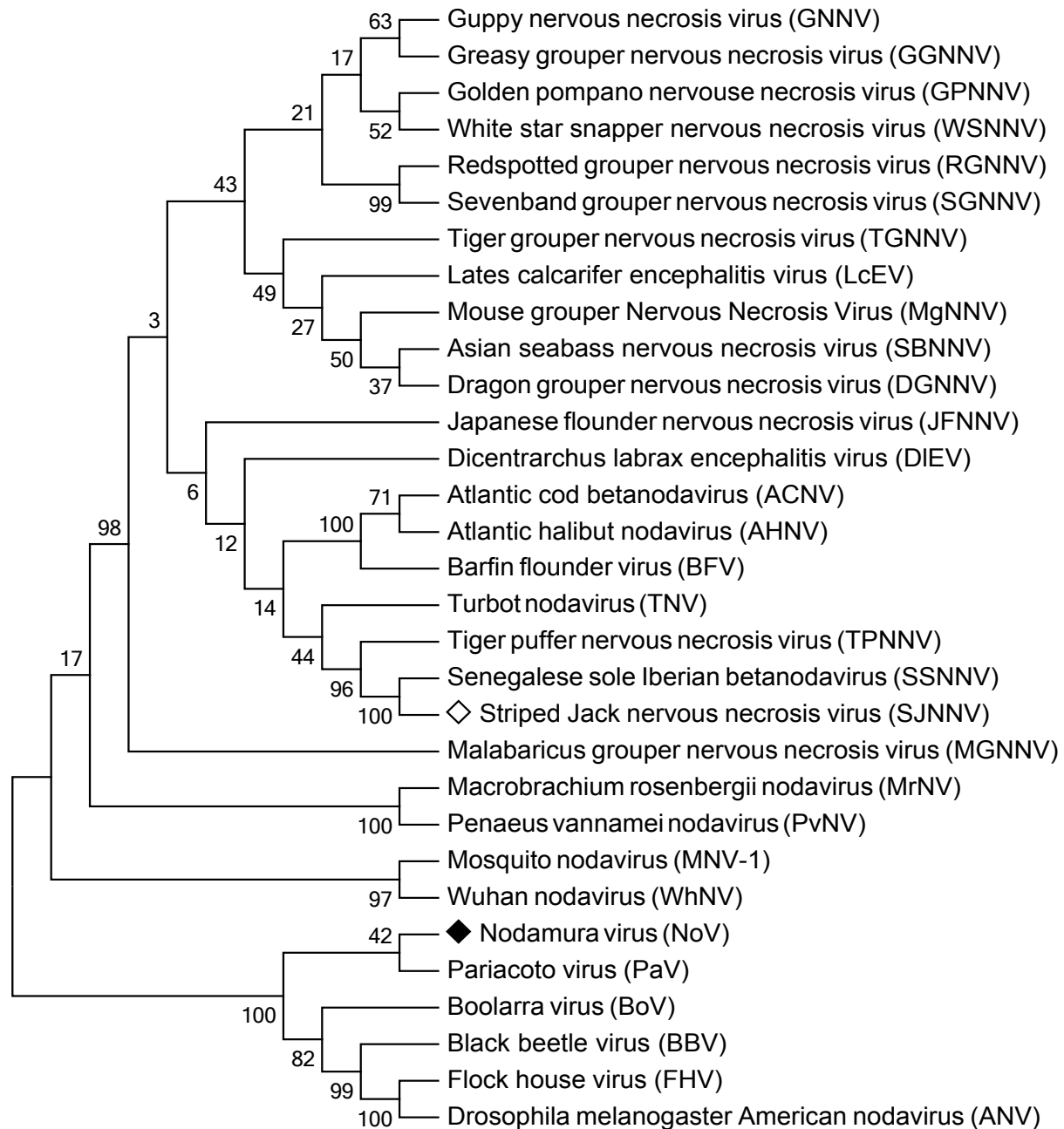


Figure 38: Phylogeny among the alpha- and betanodavirus RNA2 segments. Multiple sequence alignments were performed using Clustal Omega. Phylogenetic analysis was performed using the maximum-likelihood method and unrooted trees were drawn using MEGA6. The bootstrap values are represented as percentages of 1000 resamplings. Representative members of each genera are marked with symbols **filled diamond**) NoV, alphanodaviruses, **open diamond**) SJNNV, betanodaviruses.



sequence of PaV grouped with the betanodavirus RNA1 clade (**Figure 37**) (149). A similar genetic diversion was reported in nodaviral sequences found in bat guano in the United States. Although the bat guano tested was from insectivore bat species, the bat guano-associated nodavirus GF-4 (**BGNV**) RNA1 sequence isolated groups in the betanodavirus clade (**Figure 38**) (4, 169, 217).

A1.2 Mitochondrial association of protein A

Positive-strand RNA viruses utilize a wide variety of intracellular organelle membranes to build networks of RCs, often via interactions between membranes and one or more viral nonstructural proteins (84, 87, 142). The nodaviruses establish replication complexes within invaginations or spherules on the outer mitochondrial membrane, which are also in close association with RNA replication and viral particles (106, 168). So far, protein A has been shown to be a mitochondrial membrane associated protein and is the only protein required for nodavirus RC formation. Protein A for several nodaviruses has been reported to contain predicted secondary structures responsible for membrane anchoring and sequences for mitochondrial targeting. Not all nodavirus RdRps utilize the same tactics or sequences to anchor themselves to mitochondria. Protein A from FHV, GGNNV and WhNV are predicted to have N-terminal TMDs (166). Miller and Ahlquist (2002) predicted the presence of a single TMD from amino acids 15-36 on FHV protein A. They further showed that the N-terminal 46 amino acids of FHV protein A serves as a MTS and enables the replicase to interact with outer mitochondrial membranes as an integral membrane protein. Guo *et al.* (2004) showed similar results for the GGNNV protein A, except there are two predicted TMDs from

amino acids 153-173 and 229-249. AHNV protein A was predicted to have two independent TMDs at amino acids 1-40 and 225-246 with MTS activity and sequences similar to those found in FHV (1-40) and GGNNV (229-249) (204). There are also 2 predicted TMDs in the protein A sequence for WhNV from amino acids 33-64 and 212-254 (84). NoV protein A was predicted to have two N-terminal MARs that serve to anchor protein A to membranes as an integral membrane protein, but in a fashion different to that of FHV and GGNNV. Our hydrophobicity plots of the protein A sequences (**Figure 41**) show that the above mentioned nodaviruses have internal and N-terminal hydrophobic regions that could serve as membrane anchors with the exception of PaV. The hydrophobicity of PaV protein A does not reach the lower cutoff anywhere in the sequence and the most hydrophobic region is at the C-terminus around amino acid 800 (**Figure 41, D**).

A1.3 Concluding Remarks

The family *Nodaviridae* is a very diverse and economically important group of pathogens. Since the last comparative review of six nodavirus sequences, several nodavirus isolates have been found and their sequences have been made available. The primary focus of this appendix was the presentation of bioinformatical data that compares the genomic segments of 31 nodaviruses (where sequence was reported) and compared the hydrophobicity of the RdRps of select alphanodaviruses.

A

Alphanodavirus RNA1						
	Nov RNA1	BBV RNA1	FHV RNA1	BoV RNA1	PaV RNA1	WhNV RNA1
Nov RNA1	100	53.69	53.85	53.26	46.01	43.68
BBV RNA1	53.69	100	99	78.56	45.71	46.39
FHV RNA1	53.85	99	100	78.57	45.86	46.46
BoV RNA1	53.26	78.56	78.57	100	45.85	46.18
PaV RNA1	46.01	45.71	45.86	45.85	100	54.64
WhNV RNA1	43.68	46.39	46.46	46.18	54.64	100

B

Alphanodavirus RNA2						
	Wuhan RNA2	PaV RNA2	NoV RNA2	BoV RNA2	BBV RNA2	FHV RNA2
Wuhan RNA2	100	43.39	44.41	45.33	44.82	46.44
PaV RNA2	43.39	100	50.68	47.4	49.72	48.54
NoV RNA2	44.41	50.68	100	52.98	56.12	55.71
BoV RNA2	45.33	47.4	52.98	100	58.33	57.41
BBV RNA2	44.82	49.72	56.12	58.33	100	77.43
FHV RNA2	46.44	48.54	55.71	57.41	77.43	100

Figure 39: Sequence identity of alphanodavirus genomic RNAs. (A) RNA1 and **(B)** RNA2 based off the multiple sequence alignments used to draw the dendrograms in figures 36 and 37.

A

Betanodavirus RNA1										
	MrNV RNA1	GGNNV RNA1	DGNNV RNA1	JFNNV RNA1	RGNNV RNA1	SJNNV RNA1	TPNNV RNA1	AHNV RNA1	ACNV RNA1	BFNNV RNA1
MrNV RNA1	100	51.53	51.35	51.49	51.44	48.97	50.22	49.33	49.47	49.08
GGNNV RNA1	51.53	100	97.84	97.62	97.94	82.13	82.81	83.25	83.04	82.99
DGNNV RNA1	51.35	97.84	100	98.16	98.42	82.59	82.78	83.31	83.21	83.12
JFNNV RNA1	51.49	97.62	98.16	100	99.32	82.17	82.88	83.21	83.08	82.89
RGNNV RNA1	51.44	97.94	98.42	99.32	100	82.15	82.73	83.12	83.02	82.93
SJNNV RNA1	48.97	82.13	82.59	82.17	82.15	100	82.82	83.25	83.02	82.99
TPNNV RNA1	50.22	82.81	82.78	82.88	82.73	82.82	100	91.55	91.71	91.58
AHNV RNA1	49.33	83.25	83.31	83.21	83.12	83.25	91.55	100	99.1	98.97
ACNV RNA1	49.47	83.04	83.21	83.08	83.02	83.02	91.71	99.1	100	99.27
BFNNV RNA1	49.08	82.99	83.12	82.89	82.93	82.99	91.58	98.97	99.27	100

B

Betanodavirus RNA2										
	MrNV RNA2	AHNV RNA2	ACNV RNA2	BFNNV RNA2	JFNNV RNA2	DGNNV RNA2	GGNNV RNA2	RGNNV RNA2	SJNNV RNA2	TPNNV RNA2
MrNV RNA2	100	51.89	51.17	52.54	49.31	51.64	51.73	52.11	51.29	51
AHNV RNA2	51.89	100	98.23	98.61	82.17	81.98	81.59	81.83	79.34	79.97
ACNV RNA2	51.17	98.23	100	98.47	81.57	81.34	81.17	81.26	78.97	80.03
BFNNV RNA2	52.54	98.61	98.47	100	82.41	82.94	82.59	82.81	80.3	80.94
JFNNV RNA2	49.31	82.17	81.57	82.41	100	97.59	96.99	97.59	78.19	79.4
DGNNV RNA2	51.64	81.98	81.34	82.94	97.59	100	98.53	98.95	80.38	81.02
GGNNV RNA2	51.73	81.59	81.17	82.59	96.99	98.53	100	99.02	79.89	80.52
RGNNV RNA2	52.11	81.83	81.26	82.81	97.59	98.95	99.02	100	80.11	80.61
SJNNV RNA2	51.29	79.34	78.97	80.3	78.19	80.38	79.89	80.11	100	81.77
TPNNV RNA2	51	79.97	80.03	80.94	79.4	81.02	80.52	80.61	81.77	100

Figure 40: Sequence identity of betanodavirus genomic RNAs. (A) RNA1 and (B) RNA2 based off the multiple sequence alignments used to draw the dendrograms in figures 36 and 37.

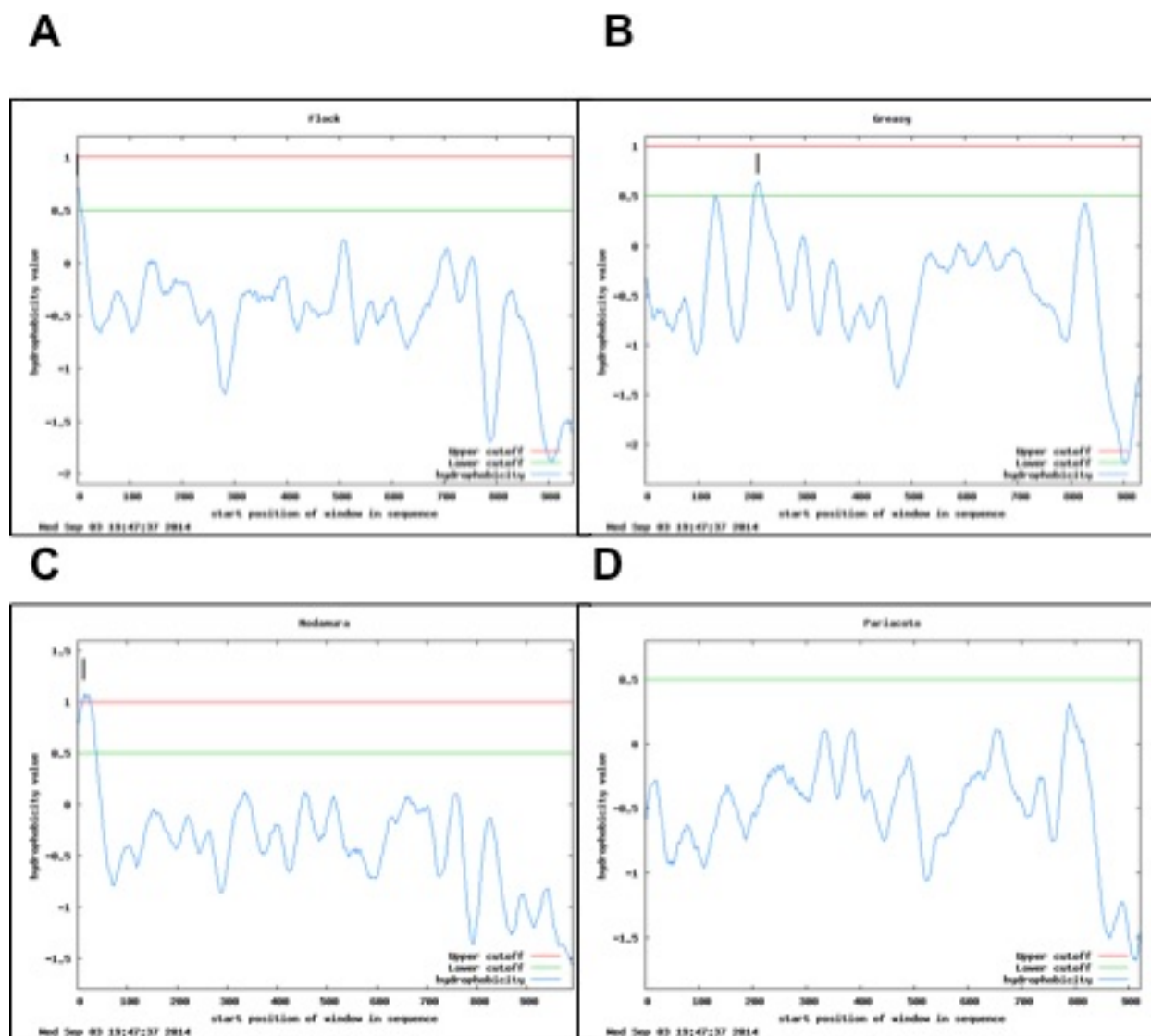


Figure 41: Topology predictions for protein A from FHV, GGNNV, NoV, and PaV. Hydrophobicity was calculated using the method of Kyte and Doolittle with a core window size of 11 and a full window of 21 aa. Red line, upper cutoff; green line lower cutoff.

Curriculum Vita

Vincent U. Gant Jr. earned his Bachelor of Science degree in Biomedical Sciences from the University of Texas at El Paso in 2008. Vincent was accepted into the Biological Sciences graduate program at The University of Texas at El Paso (**UTEP**) in Fall, 2008 and joined the Biological Sciences doctoral program the following Spring of 2009. Vincent has trained and taught well over 30 undergraduate students with many of them continuing their careers in industry, graduate school, or medical school. While in the doctoral program Vincent has earned numerous fellowships, honors and awards.

Honors and Awards

- Best Graduate Student Presentation Award. Annual Meeting of the Rio Grande Branch of the American Society for Microbiology. The University of Texas at El Paso, February 2014.
- Society for Advancement of Chicanos and Native Americans in Science (SACNAS) Travel Scholarship, October 2012.

Fellowships

- **American Society for Microbiology Robert D. Watkins Graduate Research Fellowship.** American Society for Microbiology, 2014-2015
- **Research Initiatives for Scientific Enhancement Graduate Scholars Program Fellowship.** National Institute of General Sciences from the Division of Minority Opportunities in Research (MORE), 2009 and 2011-2014.
- **Louis Stokes Alliance for Minority Participation (LSAMP) Bridge to the Doctorate (BD) Fellowship.** National Science Foundation, 2009-2011.

National Conference Presentations

- Two Membrane-Associated Regions within the *Nodamura virus* RNA-Dependent RNA Polymerase are Critical for Both Mitochondrial Localization and RNA Replication. Annual Meeting of the Rio Grande Branch of the American Society for Microbiology, University of Texas at El Paso, El Paso, TX. 2014.
- Nodamura Virus RdRp Is a Membrane-Associated Protein That Localizes to the Outer Mitochondrial Membrane in Transfected Mammalian Cells, Resulting in Clustering of Mitochondria. American Society for Virology 32nd Annual Meeting, State College, PA. 2013.

Publications

- Gant Jr., V.U., Moreno, S., Varela-Ramirez, A., and Johnson, K.L. Two membrane-associated regions within the Nodamura virus RNA-dependent RNA polymerase are critical for both mitochondrial localization and RNA replication. *Journal of Virology*. 88:5912-5926 June, 2014.
- Moreno–Olivas, F., Gant Jr., V.U., Johnson, K.L., Peralta-Videa, J.R., and Gardea-Torresdey, J. Random amplified polymorphic DNA reveals that TiO₂ nanoparticles are genotoxic to *Cucurbita pepo*. *JZUS. (Applied physics and engineering)*. 15(8): 618-623 July, 2014.

Permanent address: 10625 Onyxstone Street
 El Paso, TX 79924

This dissertation was typed by Vincent U. Gant, Jr.